Understanding catalytic processes and their selectivity from first principles: The oxidation of ammonia

von
Dipl. chem.
Claudia Mangold

im Fachbereich Physik der Freien Universität Berlin eingereichte
Dissertation zur Erlangung des Akademischen Grades
DOCTOR RERUM NATURALIUM

Berlin, 2011

MAX-PLANCK-GESELLSCHAFT

Diese Arbeit wurde in der Zeit von November 2008 bis Dezember 2011 unter der Aufsicht von Prof. Dr. Karsten Reuter in der Abteilung Theorie von Prof. Matthias Scheffler am Fritz-Haber-Institut der Max-Planck-Gesellschaft durchgeführt.

Erster Gutachter (Betreuer): Prof. Dr. Karsten Reuter
Zweiter Gutachter: Prof. Dr. Martin Weinelt
Disputationstermin: 13. Februar 2012

Contents

List of Figures

List of Tables

Chapter 1

Introduction

Catalytic selectivity: Impact and obstacles

For a rational improvement of industrial catalytic processes the detailed understanding of the corresponding reaction network is crucial: The knowledge about reaction intermediates and involved reaction steps can offer precious insights into the events within the catalytic cycle and therewith increase the knowledge about the parameters that are to be changed to advance the overall process. In heterogeneous catalysis, when it comes to a reaction between a solid catalyst and a gaseous environment[1], a wide variety of methodologies are available to investigate the status on the surface of a catalyst as well as the reactions that are occurring on it. Among these are the thermal desorption spectroscopy (TDS) and high resolution electron energy-loss spectroscopy (HREELS) which help to reveal what desorbs *off* the surface and what is attached *on* the surface of the catalyst, respectively. Besides the fortunes each experimental method has its deficiencies: In HREELS spectra for example, only adsorbates that are stable for a *sufficiently* long time can be observed – a rather unstable intermediate can be overseen. And TDS experiments can not detect an adsorbate that decomposes in the gas phase before the detector is reached. A *theoretical* approach to the analysis of catalytic reaction networks can help to fill such missing parts and therewith gain even deeper insights into the overall picture of a process.

A seminal and by now well investigated model reaction where theory and experiment combined forces to expand the knowledge of both is the CO oxidation reaction to CO_2 [4–10]. For theoreticians who aim at an atomic scale understanding a major challenge was the so-called pressure gap: Standard electronic structure theory based descriptions of surface systems have the disadvantage that the distribution of the

---

[1] which represents the setup of most of the industrially performed catalytic processes [3].

electrons and with that the energy of the system is evaluated at a pressure of zero. This is far off a realistic description of any industrial process and therefore a multiscale modeling approach to bridge this gap between theory and experiment has to be performed: Within this framework the kinetic parameters for the elementary processes are derived on the basis of first-principles electronic structure calculations. These parameters serve as an input for a kinetic Monte Carlo (kMC) simulation (on a mesoscopic time and length scale) to analyze the concerted interplay of processes in the catalytic cycle.

The focus of CO oxidation research was on the improvement of the *activity* of a catalyst[2]. The *selectivity* of any catalytic reaction is the second main aspect to assess the performance of a catalyst: If a process has more than one possible stable product[3] the knowledge about the parameters that determine whether one or the other (or even a third) of these products is formed is crucial. The main obstacle that complicates investigations of the selectivity of those reactions is the complexity even of the most basic reaction schemes.

A rather simple reaction that exhibits selectivity is the catalytic oxidation of ammonia to nitrogen monoxide. Despite its simplicity this oxidation reaction illustrates already nicely how desirable but also challenging a detailed understanding and concomitant control of the reaction selectivity is: In the industrially important Ostwald

---

[2] The activity of a catalyst is measured in terms of the turnover frequency, i.e. the number of converted product molecules per site and second: TOF $[site^{-1}s^{-1}]$

[3] This immediately shows why the selectivity does not play a role within the CO oxidation: This process has only one product.

process[4] [11–13] nitrogen monoxide (NO) is the favored product 1.1 (as an intermediate for the production of nitric acid (HNO_3)):

$$4\ NH_3 + 5\,O_2 \quad \xrightarrow[\text{Pt/Rh−gauze}]{700\,\text{K}} \quad 4\,NO + 6\,H_2O \tag{1.1}$$

But this reaction can also lead to molecular nitrogen (N_2) 1.2:

$$4\ NH_3 + 3\,O_2 \quad \rightarrow \quad 2\,N_2 + 6\,H_2O \tag{1.2}$$

What is the undesired side product in the Ostwald process, turns into the preferred one when it comes to air pollution and NO in its role as a greenhouse gas. Eqns. 1.1 and 1.2 show the stoichiometric reaction equations for the first step of the Ostwald process: The highest crop of the main product NO is achieved under the reaction conditions displayed in 1.1. However, the *detailed* intermediate steps of this reaction are not known – and the possibilities are manifold: To start with an analysis of what could happen during the oxidation of ammonia to NO and N_2 at a catalyst surface (like the Pt-catalyst as it is applied in the Ostwald process) the most obvious reactions are the stepwise dehydrogenation reaction of ammonia and its descendants via oxygen and OH, as well as the spontaneous decomposition of NH_x species accompanied by the appearance of atomic hydrogen. The product formation of NO and N_2 then takes place between the participating atoms. For an overview these basis reactions are summarized in figure 1.1. Attempts to explain the oxidation of ammonia on several model catalyst surfaces comprising these reactions (partially or completely)

---

[4] The Ostwald process is the main source for nitric acid in chemical industries which is on the other hand a precursor for the production of fertilizers (ammonium- and potassium-salts of the acid). After the ammonia oxidation reaction to NO the Ostwald process continues as follows:
After oxidation and dimerisation in the gas phase (g), disproportionation is initiated with liquid (l) water:

$$\begin{aligned} NO\,(g) + O_2 \quad &\xrightarrow{\text{Oxidation}} \quad NO_2(g) \\ 2\ NO_2(g) \quad &\xrightarrow{\text{Dimerisation}} \quad N_2O_4\,(g) \\ 2\ N_2O_4 + H_2O\,(l) \quad &\xrightarrow{\text{Disproportionation}} \quad HNO_3\,(l) + HNO_2\,(l) \end{aligned}$$

Besides the desired product, nitric acid, also nitrous acid is formed. This acid can then further disproportionate into HNO_3 and NO:

$$3HNO_2\,(l) \quad \xrightarrow{\text{Disproportionation}} \quad HNO_3\,(g) + 2NO\,(g) + H_2O\,(l)$$

The therewith formed NO molecules can take again part in the reaction cycle.

were made experimentally [1, 14–22] and theoretically [14, 15, 23–25]. The proposed reaction network, regarding the associated diffusion adsorption and desorption processes, already consists of 41 reactions. For comparison: The CO oxidation reaction network comprises in total 22 reactions. Due to the flexibility of nitrogen in terms of

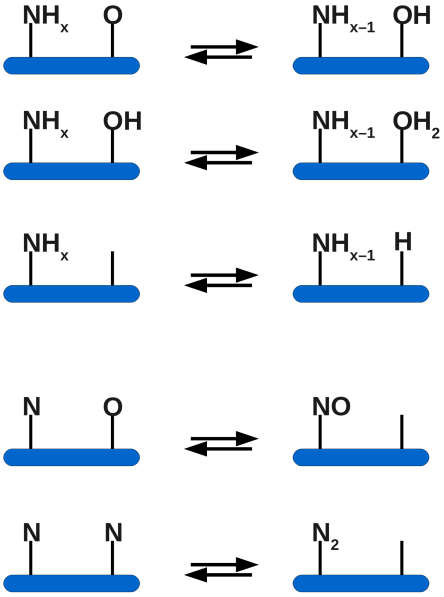

Figure 1.1: Basis reactions for the oxidation of ammonia to nitrogen monoxide and molecular nitrogen.

its oxidation state, further conceivable steps within the reaction network of the oxidation of ammonia involve the low-index species of the homologous series of azanes (N_nH_{n+2}), azenes (N_nH_n) and azadiens ($N_nH_{n\text{-}2}$), of which several were discussed in [16, 17, 26, 27], as well as nitrogen oxides (N_xO_y), which also already found reference related to the oxidation of ammonia [2, 14, 21, 25, 28–33]. Nitrogen hydroxides like hydroxylamin (H_2NOH) or nitroxyl (HNO) are also possible intermediates. The appearance of the latter is discussed in [34].

Furthermore, the diffusion of hydrogen atoms between oxygen- or nitrogen species respectively can play a decisive role within the reaction ensemble. The situation gets even more complex with potentially significant lateral interactions between adsorbates at the catalyst surface. This elevates the number of potential inequivalent processes easily far beyond 200 cross-linked steps – although so far only one type of active site at a catalyst surface is considered (for a list of these processes see appendix C). If there are two different site types, the number of processes on the list has to be multiplied by four: Reactions between adsorbates on two same sites as well as on two different sites can occur, while for the latter it has to be differentiated, which species is adsorbed on which of the two sites. Concerted reactions between three or more reactants on the surface are thereby not even considered.

This clearly reveals that even an apparently simple and innocent looking reaction like the oxidation of ammonia with solely two main products (plus water as a side product) can hide a complex reaction network. To account for this extended reaction scheme on a theoretical basis it is not straightforward to simply apply the ansatz used for the CO reaction network: Within this investigation the barriers for all possible 22 reactions were evaluated with electronic structure calculations. For the multiplicity of possible reactions as mentioned above this strategy is in fact (almost) not feasible, but definitely also not worthwhile: Many reactions that are *possible*, will in the end not play a role within the reaction context – an expensive first-principles calculation of the corresponding reaction barrier would therefore be just a waste of resources. Therefore a *sensitivity-guided* multiscale modeling approach will be developed and explored in this work: To account for the challenge to handle a far greater set of reactions and intermediates, not all energy parameters for all possible elementary reactions are evaluated as it was done instead within the multiscale modeling approach for the CO oxidation reaction. A selection among all possible reactions is performed: The most encouraging reactions are chosen initially as a basis setup. Further reactions are then to be added stepwise to complete the reaction network of the ammonia oxidation until the reaction pathway with all its side and sub-reactions is revealed. The decision which reactions are promising is initially based on chemical intuition as well as information from literature (if available) and the aim is to start with a moderate but sufficient setup. For following iterations further reactions are added to the process list and the sensitivity of these changes on the reaction network is evaluated. Due to their performance the additional reactions are utilized in further simulations.

Recent detailed experiments [1] inspired by the first step of the Ostwald process investigated how the catalytic oxidation of ammonia performs when a model oxide catalyst, namely RuO_2 on its (110) facet is used. Even though these experiments were executed under pressures much lower than those used in the industrial process, the results are promising: The selective conversion to NO could be achieved with significantly lower reaction temperature: $500\,K$ for $\approx 90\,\%$ selectivity to NO and $530\,K$ for $\approx 100\,\%$ selectivity vs. $\approx 700\,K$ in the commonly used process in industries. Due to this highly interesting upgrade in terms of the reaction conditions the catalytic oxidation of ammonia on $\mathrm{RuO_2}(110)$ was chosen as the test case to develop the above described methodology. Furthermore, the specific surface is particularly appealing for the exploratory study as extensive studies in the past have led to a well-established surface structure model [6, 35] (see figure 3.1).

Ensuring experiments of Perez-Ramirez *et al.* [14] could not confirm the outstanding high selectivity to NO as it was observed in the afore mentioned experiments. Notwithstanding, the same *ratios* of the two involved partial pressures of ammonia and of oxygen were taken for the various measurements within both experiments, the *absolute* values of the partial pressures differ: While the experiments in [1] were performed under ultrahigh vacuum (UHV) conditions, ambient pressure dominates in the experiments of [14]. Perez-Ramirez already speculated that this could be the reason for the different selectivities.

Both experimental findings thus present themselves as a good target for the theoretical evaluation of the reaction network: They provide a rich source of information especially concerning the various pressure regimes. Furthermore they can serve as a benchmark for the quality of the ansatz. Therewith the oxidation of ammonia on $\mathrm{RuO_2}(110)$ constitutes a prosperous example to apply the ansatz of a *sensitivity-guided* multiscale modeling approach for a thorough understanding of this reaction network, with an emphasis on its selectivity.

Chapter 2

Methodology

2.1 Multiscale modeling approach

For a directive optimisation of an industrial process a thorough knowledge about the underlying elementary reaction steps is desirable. With this it would be possible to identify and vary the crucial parameters by which this process is governed. Computational modeling has already become a key contributor to gain insights into those elementary reaction steps playing on the microscopic time and length scales: The detailed making and breaking of chemical bonds, determining the energetics of the elementary processes, occurs within picoseconds and obviously on the atomic scale. Such scenarios can be described on an *ab initio* level using first-principles electronic structure theory. However an industrial process plays in the macroscopic regime, which means minutes or even hours on the time scale and meters on the length scale. To span these disparate regions in time and space hierarchical approaches that integrate various levels of theory into one multi-scale simulation are needed. Such an approach is what is usually referred to as multiscale modeling [36, 37] (for an illustration of the different realms in time and length see diagram 2.1). In this approach first-principles electronic structure theory, that plays in the microscopic regime, is connected with the mesoscopic realm where the statistical interplay among the manifold of different elementary processes is appropriately evaluated to determine the overall surface catalytic function. For the former requirement, density functional theory (DFT) is applied, which nowadays represents the best compromise between accuracy and computational cost for studies at extended metal or metal-oxide surfaces, as investigated here in this work. For the latter task, particularly kinetic Monte Carlo (kMC) simulations offer the prospect to improve over the prevalent mean-field description of standard rate equation based approaches and explicitly account for the spatial distributions of the adsorbates at the surface [36]. The link between these two methods is established by transition state theory [38, 39].

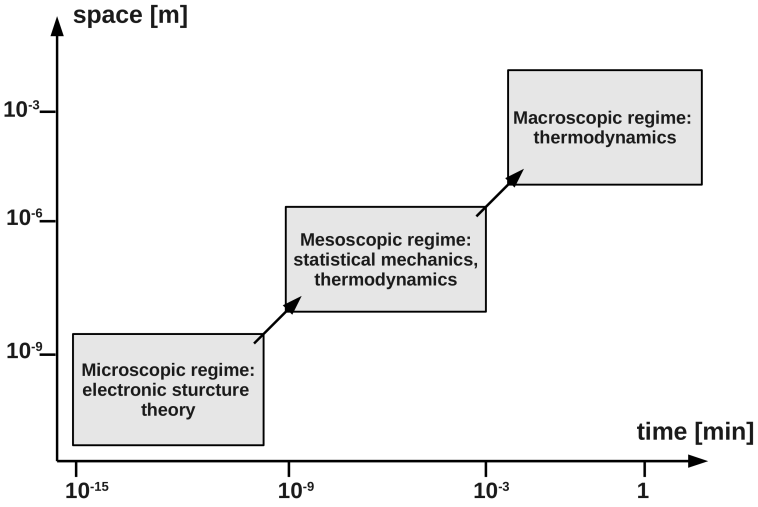

Figure 2.1: Overview over the range of realms of time and space of relevance for the present work: Electronic structure calculations give insight into the elementary processes on an atomistic – microscopic – level; statistical mechanics can describe the mesoscopic realm. *Ab initio* thermodynamics provides information on the macroscopic scale.

For simple model reactions like the CO oxidation such first-principles microkinetic simulations have already provided highly valuable insight into the factors that govern the overall catalytic activity [8–10, 40]. Unfortunately, the extension of this methodology to more complex reaction networks is severely challenged by the exploding number of inequivalent elementary processes and the thereby prohibitive computational costs to determine their first-principles kinetic parameters. To date this has prevented this multiscale modeling approach from being employed to provide similarly detailed insight as for the overall activity of simple reactions. This holds in particular for the factors that govern the selectivity in reactions where more than one product is thermodynamically feasible. Acknowledging this, a novel approach based on a *sensitivity-analysis* guided refinement will be explored in this work to keep the number of elementary processes that have to be investigated as low as possible. Support for this sensitivity guided refinement approach will come from *ab initio* thermodynamics [41–44]. With the latter method, playing in the macroscopic regime of time and space, valuable information about the constitution of the catalyst surface under varying reaction conditions is accessible. In the following the above mentioned methods will be introduced in as much as of relevance for the present work.

2.2 Density functional theory

For describing the electronic structure of matter – let it be an isolated molecule or extended crystals and their surfaces – density functional theory (DFT) is presently among the most popular and most widely used methods in theoretical solid state pyhsics and quantum chemistry[5]. In contrast to the initiations of quantum mechanics, DFT no longer focuses on the wavefunction as the key quantity to get the energetics of a system (like in Hartree-Fock (HF) theory), but rather deals with another quantity, the electron density $n(r)$.With that the many-body problem to solve an exact equation, the Schrödinger equation, that has too many variables[6] to be solved explicitly, is shifted to the problem of solving an equation that depends solely on the three different spatial coordinates of the electron density, but whose explicit form is not known.

2.2.1 Basics of DFT

The idea of using the electron density $n(r)$ as the key quantity to get the energetics of a system is about as old as the ansatz of the wavefunction approach [49] and goes back to L.H. Thomas and E. Fermi [50, 51] in the late twenties of the former century. Thomas and Fermi used the concept of the uniform electron gas[7] to describe the interaction of electrons to express the total energy of a system as a functional of the electron density. Naturally there are four different energy contributions to the total energy of a system: the kinetic energy of the system, the attractive forces between electrons and nuclei, the repulsive forces between electrons and the repulsive forces between nuclei. The latter are considered constant within the Born Oppenheimer (BO) approximation [52][8]. With this in mind one arrives at a universal expression

---

[5] For an all-embracing description of DFT, the reader can choose from a manifold of textbook and reviews. The author found the following the most helpful ones: [45–48]

[6] $3N$, with N being the number of electrons of the system of interest.

[7] This concept, also known as 'jellium model' is especially suitable for the observation of electron-electron interactions as the nuclei (with their positive charge) are assumed to be distributed uniformly.

[8] The BO approximation is applied for all concepts exemplified in this work

for the energy in terms of the density:

$$E[n(r)] = \underbrace{T[n(r)]}_{\text{kinetic energy}} + \underbrace{E_{\text{ne}}[n(r)]}_{\text{nuclear}-\text{electron interaction}} + \underbrace{E_{\text{ee}}[n(r)]}_{\text{electron}-\text{electron interaction}} \tag{2.1}$$

where it is conventional to separate the electron-electron interaction into its exchange/ correlation and Coulomb fraction:

$$E_{\text{ee}}[n(r)] = \underbrace{E_{\text{XC}}[n(r)]}_{\text{Exchange interaction}} + \underbrace{E_{\text{Coulomb}}[n(r)]}_{\text{Coulomb repulsion}} \tag{2.2}$$

While the electron-nucleus interaction as well as the Coulomb part of the electron-electron interaction are described classically within the Thomas-Fermi (TF) approach, for the kinetic energy the afore mentioned concepts of the uniform electron gas are applied to form the Thomas-Fermi energy functional:

$$E_{\text{TF}} = \frac{3}{10}(3\pi^2)\frac{2}{3}\int n\frac{5}{3}(r)dr - \int \frac{Zn(r)}{r}dr + \frac{1}{2}\int\int \frac{n(r_1)n(r_2)}{r_{1,2}}dr_1 dr_2 \tag{2.3}$$

This is a rather crude approximation – not only because of the disregard of the exchange energy, but also because the uniform electron gas represents a rather poor description for the kinetic energy. Even worse the TF model cannot cope with a chemical bond and therefore fails for the description of molecules. Although some improvements were tried – consideration of the exchange energy also in the spirit of the uniform electron gas within the slightly better Thomas-Fermi-Dirac model [53], or the inclusion of not only the density but also its gradient to the kinetic as well as the exchange energy – the methods still produced unacceptable errors.

Hohenberg-Kohn theorems

In defiance to all these drawbacks the TF model was the corner stone for modern DFT: Hohenberg and Kohn justified the employed concept of the electron density being a basic variable to entirely determine the properties of a system, or more precisely, they could show that for a system in the groundstate with a given potential $V(r)$ there is only one electron density $n(r)$[9].

Hohenberg and Kohn furthermore defined an energy functional $E[n(r)]$ and proved that the electron density of a system indeed minimizes this energy functional (as was

---

[9] The Hohenberg-Kohn theorems do not include the description of excited states though they can be extended to describe time dependent processes. This comes under the name TD-DFT.

assumed by Thomas and Fermi already who used the variational principle to solve eqn. 2.3) (For a derivation of the two theorems see the original literature [54] or standard textbooks).
The energy functional introduced by Hohenberg and Kohn has the following form:

$$E_{\mathrm{HK}}[n(r)] = \int n(r) V_{\mathrm{ext}} dr + F_{\mathrm{HK}}[n(r)] \tag{2.4}$$

The Hohenberg-Kohn functional $F_{\mathrm{HK}}[n(r)]$ includes both the kinetic energy and the electron-electron interaction with the latter split into its classical Coulomb- (also called Hartree-) and non-classical exchange-correlation (non-classical (ncl)) part (the former analogous to the TF model):

$$F_{\mathrm{HK}}[n(r)] = T[n] + \underbrace{\frac{1}{2}\int\int E_{\mathrm{Hartree}} + E_{\mathrm{ncl}}[n(r)]}_{E_{\mathrm{ee}}[n]} \tag{2.5}$$

The most important fact about the Hohenberg-Kohn functional $F_{\mathrm{HK}}[n(r)]$ is that it is unknown. The best approach so far to overcome this obstacle within the framework of DFT is with the help of the Kohn-Sham equations.

The Kohn-Sham ansatz

The main idea of Kohn and Sham to access the Hohenberg-Kohn functional $F_{\mathrm{HK}}[n(r)]$ was to separate the kinetic energy T into two parts: One being the kinetic energy of the system T_{S} with no interaction between the particles and one being the correction term T_{c} that accounts for the former approximation as the electrons in the real system of course do interact. With that concept, the kinetic energy T_{S} of all electrons can be expressed as the sum over their independent one-electron wavefunctions ϕ_i [55]:

$$T_{\mathrm{S}} = \sum_{i=1}^{N} \langle \phi_i(r)| - \frac{1}{2}\nabla^2 |\phi_i(r)\rangle \tag{2.6}$$

The index in T_{S} points out that actually a Slater determinant is calculated. The Hohenberg-Kohn functional can then be written as

$$F_{\mathrm{HK}}[n(r)] = T_{\mathrm{S}}[n] + \frac{1}{2} E_{\mathrm{Hartree}}[n(r)] + E_{\mathrm{XC}}[n(r)] \tag{2.7}$$

with $E_{\mathrm{XC}}[n(r)]$, the exchange-correlation (XC-) functional, that includes the electrons' non-classical behavior as well as kinetic energy-correction term T_{c}. With that, the problem of the unknown Hohenberg-Kohn functional $F_{\mathrm{HK}}[n(r)]$ is shifted to the

problem of the unknown XC-functional $E_{\mathrm{XC}}[n(r)]$. How such functionals can be constructed is the subject of the following section.
To obtain now the ground state energy of the system, the energy should be minimized by executing the variational principle on eqn. 2.4, i.e. variation of the wavefunction ϕ. Since only T_{S} is a function of ϕ, minimization with respect to this variable leads to the following variational equation:

$$\frac{\delta E_{\mathrm{HK}}}{\delta \phi_i(r)} = \frac{\delta T_{\mathrm{S}}}{\delta \phi_i(r)} + \left[\frac{\delta V_{\mathrm{ext}}}{\delta n(r)} + \frac{\delta E_{\mathrm{Hartree}}}{\delta n(r)} + \frac{\delta E_{\mathrm{XC}}}{\delta n(r)}\right] \times \frac{\delta n(r)}{\phi_i(r)} = 0 \tag{2.8}$$

With eqn. 2.6 and

$$n(r) = \sum_{i=1}^{N} |\phi_i(r)|^2 \tag{2.9}$$

eqn. 2.8 can be simplified to

$$(H_{\mathrm{KS}} - \epsilon_i)\phi_i(r) = 0 \tag{2.10}$$

with H_{KS}, the Kohn-Sham Hamiltionian

$$H_{\mathrm{KS}} = -\frac{1}{2}\nabla^2 + V_{\mathrm{eff}}(r) \tag{2.11}$$

with $V_{\mathrm{eff}}(r)$ being the effective potential, gathering the energy contributions of the external potential, the Hartree term and the XC-energy. Eqn. 2.10 are the famous Kohn-Sham (KS) equations that are to be solved in a standard DFT calculation. Within the KS equations the many-body problem of *interacting* particles is transformed to a single-particle problem of *non-interacting* particles being in an effective potential caused by all other electrons.
The total energy of a system as described above is thus a functional of the electron density and so are the various contributions to this energy. Therefore the Kohn-Sham equations have to be solved iteratively. In practice this is done as follows: After an initial guess for the electron density, the effective potential V_{eff} of this electron density is calculated. With this effective potential, the KS equations are solved. With the therewith evaluated wavefunctions, the new electron density of the system is evaluated. If the new electron density is not consistent with the initial one, a new cycle of calculation starts, using the generated electron density as a new input for evaluating the effective potential. A flowchart of the succession of this self-consistency cycle is shown in figure 2.2.

Choice of the exchange correlation functional

As alluded to the preceding section, it is the main goal and obstacle in DFT to find a good expression for the XC-functional $E_{\mathrm{XC}}[n(r)]$. A first attempt was the local

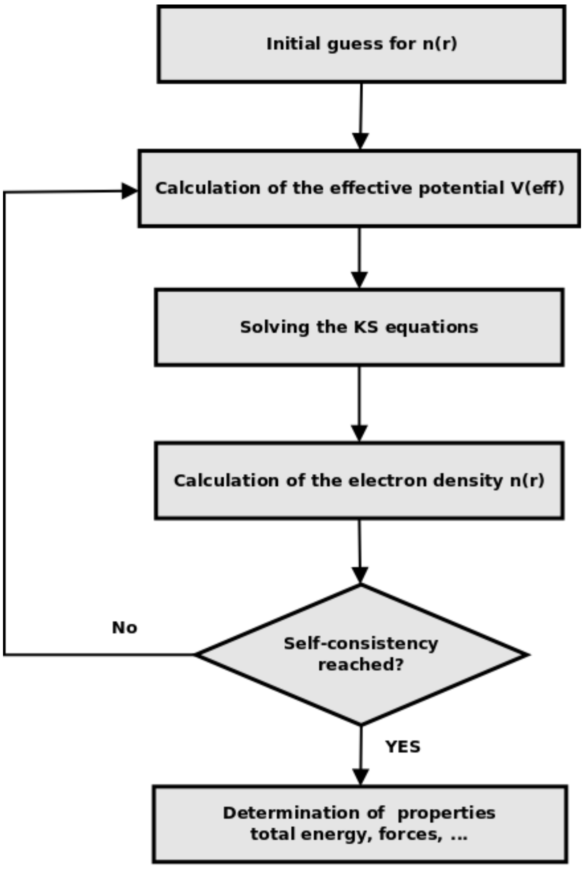

Figure 2.2: Schematic representation of the self consistency cycle for solving the KS equations.

density approximation (LDA). This class of XC-functionals treats the electrons as a uniform electron gas (as assumed to be a good approximation for simple metals).

$$E_{\mathrm{XC}}^{\mathrm{LDA}}[n(r)] = \int n(r)\epsilon_{\mathrm{XC}}[n(r)]dr \tag{2.12}$$

Separating E_{XC} in its exchange and correlation part, one can find a rather simple expression for E_{X} [46]:

$$-\epsilon_{\mathrm{X}} = \frac{3}{4}\sqrt[3]{\frac{9n(r)}{\pi}} \tag{2.13}$$

However, the correlation term has to be numerically evaluated with Quantum Monte Carlo (QMC) methods as was done in [56]. These QMC results have to be interpolated adequately to be used in DFT calculations. The resulting LDA functional is known to significantly overestimate binding energies and cohesive energies [57, 58].

An improvement over LDA is represented by the generalized gradient approximation (GGA). The XC-functionals based on the GGA account not only for the local electron density, but also for its gradient $|\nabla n(r)|$ and are therefore often referred to as semi-local functionals:

$$E_{\mathrm{XC}}^{\mathrm{GGA}}[n(r)] = \int n(r)\epsilon_{\mathrm{XC}}[n(r), \nabla n(r)]dr \tag{2.14}$$

or rather

$$E_{\mathrm{XC}}^{\mathrm{GGA}}[n(r)] = \int n(r)\epsilon_{\mathrm{XC}}^{\mathrm{LDA}}(n)F_{\mathrm{XC}}[n(r), \nabla n(r)]dr \tag{2.15}$$

where F_{XC} accounts for the gradient dependency and is dimensionless and $\epsilon_{\mathrm{XC}}^{\mathrm{LDA}}(n)$ is the XC-energy density from eqn. 2.12. For a gradient of $\nabla n = 0$, F_{XC} becomes one and one gets again the LDA XC-energy from eqn. 2.12.

To evaluate F_{XC}, it is first split into its exchange part F_{X} and its correlation part F_{C}. For the former, the reduced density gradients s are needed:

$$s_m = \frac{|\nabla^m n(r)|}{2^m(3\pi^2)^{\frac{m}{3}}} n(r)^{(\frac{1+m}{3})} \tag{2.16}$$

m being the order of the gradient. With this the exchange part F_{X} can be expressed as follows:

$$F_{\mathrm{X}}(s) = 1 + \kappa - \frac{\kappa}{1 + \mu s^2/\kappa} \tag{2.17}$$

with κ and μ being constants. In atoms and molecules the reduced density gradients s are higher than in solids. Therefore the derived values for F_{X} are higher (as less is subtracted in the third term of eqn. 2.17). Higher values for F_{X} mean also higher values for the total energies. This is the reason why binding energies of molecules adsorbed on surfaces are lower compared to LDA results.

The correlation part $\mathrm{F_C}$ is more complex and typically also smaller than $\mathrm{F_X}$. The expression

$$F_{\mathrm{C}} = \frac{E_{\mathrm{C}}^{\mathrm{LDA}}(n)}{E_{\mathrm{X}}^{\mathrm{LDA}}(n)}(1 - 0.219.51s_1^2 + ...) \tag{2.18}$$

for the correlation part following Ma and Brueckner [59] is the lowest order gradient expansion at high density.

Popular functionals using this formalism are the ones constructed by Perdew and Wang (PW91) [60] or by Perdew, Burke and Enzerhof (PBE) [61] to mention just two of a manifold of GGA-XC-functionals. Within the PBE functional the overestimation of binding energies is often significantly reduced compared to LDA (for the above described reasons), but still the binding energies often differ by about half an eV from experimental results [58].

Therefore several efforts were undertaken to improve this functional. One attempt was conducted by Zhang *et al* [62]: They suggested the variation of the constant κ from $\kappa = 0.804$ as in the original paper [61] to $\kappa = 1.245$. With that they were able to get binding energies closer to experimental values. However, in the original paper by Perdew *et al* the value for κ was chosen for good reasons: By using $\kappa = 0.804$, $F_{\mathrm{X}}(s)$ is bound to the upper limit of 1.804. This gives rise to the following inequality:

$$n(r)\epsilon_{\mathrm{X}}(r) \geq -1.679 n(r)^{\frac{4}{3}} \tag{2.19}$$

which automatically leads to the fullfillment of the Lieb-Oxford bound [63]:

$$E_{\mathrm{XC}}[n] \geq -1.679 \int n(r)^{\frac{4}{3}} dr \tag{2.20}$$

This criterion marks the lower limit of $E_{\mathrm{XC}}[n(r)]$. The Lieb-Oxford bound is a universal property of XC-functionals. The necessity for such a lower bound arises from the question, *how much* the electrons with same spin can avoid each other because of their exchange interaction [64].

Zhang *et al* justified their so-called *rev*PBE with the argument that for a *given* electron density eqn. 2.19, the *local* Lieb-Oxford bound, is only a sufficient but not necessary requirement for the *integrated* Lieb-Oxford bound (eqn. 2.20). They could show that *in practice* this upper bound for F_{X} is always fullfilled.

To work around this deficiency, Hammer *et al* suggested another revised PBE functional, the so-called RPBE functional [58] which has the advantages of the *rev*PBE but does not violate the global Lieb-Oxford criterion. By defining

$$F_{\mathrm{X}}(s) = 1 + \kappa(1 - e^{(-\mu s^2/\kappa)}) \tag{2.21}$$

with $\kappa = 0.804$ this mission was accomplished.

Within the class of GGA functionals the RPBE functional often marks a lower limit in terms of binding energies of molecules (internal bonding within a gas phase molecule as well as molecules bound to a surface), while PBE yields more an upper limit.

It has to be pointed out that there is no systematic improvement scheme for XC-functionals like it exists in HF theory and its descendants. The improvement over

PBE achieved by the RPBE functional deals only with the binding energy of the molecules. It does not mean, that this functional is in general superior to PBE or any other functionals. Therefore the choice of the functional is intrinsically connected with the questions one wants to address. Since the focus of the present work is on surface reaction processes as well as desorption- and adsorption processes it is natural to choose PBE and RPBE as a useful indicator of the span of surface energetics provided by GGA-functionals.

2.2.2 Plane waves and pseudopotentials

With the Kohn-Sham ansatz the many-body problem was mapped to a single-particle problem resulting in the Kohn-Sham equations 2.10. However, no recipe to solve these equations was provided so far. In this work, reactions of adsorbates on an *extended* but periodic surface are studied. With that the system contains in principle an infinite number of electrons. This results in two obstacles: First of all it is not possible to include an infinite number of wavefunctions, and furthermore the wavefunction of each of these electrons is extended over the whole system and therefore the basis set for each wavefunction has in principle an infinite number of contributions. To cope with this problem Bloch's theorem is applied to find an expression for the wavefunctions [65]:

$$\phi_i(r) = \exp\left(i\mathbf{kr}\right) f_i(r) \tag{2.22}$$

The Bloch theorem tells that an electronic wavefunction of a periodic system can be split into a wavelike part $\exp(i\mathbf{k}r)$ (with $\mathbf{k}$ being the wavevector of the wavefunction) and a cell-periodic part $f_i(r)$. For the wavevectors $\mathbf{k}$ we can restrict ourselves to values of $\mathbf{k}$ lying in the first Brillouin zone (BZ) (it could be any unit cell of the reciprocal lattice, but the first BZ is chosen by convention) because of the periodicity of the system. Also because of the periodicity the latter function can be expanded in a basis set of plane waves:

$$f_i(r) = \sum_{\mathbf{G}} c_{i,\mathbf{G}} \exp\left(i\mathbf{G}r\right) \tag{2.23}$$

where $\mathbf{G}$, the reciprocal lattice vectors, are defined as

$$\mathbf{G}\, l = 2\pi m \tag{2.24}$$

with l being the lattice vector of the system, and m any integer. Combining with the afore mentioned expression for the wavefunction results in

$$\phi_i(r) = \exp\left(i\mathbf{k}r\right) \sum_{\mathbf{G}} c_{i,\mathbf{G}} \exp\left(i\mathbf{G}r\right) = \sum_{\mathbf{G}} c_{i,(\mathbf{k}+\mathbf{G})} \exp\left(i(\mathbf{k}+\mathbf{G})r\right) \tag{2.25}$$

In principle one could use these electronic wavefunctions to solve the KS equations. Admittedly there is still in principle an infinite number of wavevectors $\mathbf{k}$ to account for. However it generally produces reasonable results, if one considers only a finite set of wavevectors each representing a small region of $\mathbf{k}$ space. This is applicable since wavefunctions with very close wavevectors can be assumed to be nearly identical. Integration over the first BZ is therefore simplified to a summation over several $\mathbf{k}$-points:

$$\int_{BZ} \frac{1}{\Omega_{BZ}} d\mathbf{k} \rightarrow \sum_{\mathbf{k}} \omega_{\mathbf{k}} \tag{2.26}$$

with Ω_{BZ} being the unit cell of the first BZ and ω being the weight of a $\mathbf{k}$-point. The crucial question is the choice of the $\mathbf{k}$-points. There are several schemes to sample the first BZ [66–69]. In this work the $\mathbf{k}$-point sampling according to Monkhorst and Pack (MP) [66] was applied which combines symmetry related $\mathbf{k}$-points. The weight ω is then related to the number of symmetry-equivalent $\mathbf{k}$-points.

For metals or metallic oxides like RuO_2 the MP $\mathbf{k}$-point sampling saves a problem: Metals have the property of a continuous density of states (DOS) $n(\epsilon)$ at the Fermi level ϵ_F. To sample this region correctly one either needs a high density of $\mathbf{k}$-points (which is directly linked to a higher computational cost) or one introduces a smearing scheme: Earlier attemps are the ones of Ho and Fu [70, 71] who introduced Gaussian like broadened functions to describe the delicate area around the Fermi level. The exact DOS

$$n(\epsilon) = \sum_{i\mathbf{k}} \delta(\epsilon - \epsilon_{i\mathbf{k}}) \tag{2.27}$$

is therewith broadened to a smoother DOS $n'(\epsilon)$

$$n'(\epsilon) = \sum_{i\mathbf{k}} \frac{1}{\sigma} \delta' \left(\frac{\epsilon - \epsilon_{i\mathbf{k}}}{\sigma} \right) \tag{2.28}$$

The smearing actually introduces an artificial temperature to the system, for which the final energy has to be corrected after its evaluation (half of the entropic energy is subtracted) [72].

After solving the problem of an infinite number of wavefunctions, the problem of the infinite basis set of plane waves has to be conquered. This can be done by introducing a cutoff energy E_{cutoff}. Since the coefficients $c_{i,\mathbf{k}+\mathbf{G}}$ of plane waves from eqn. 2.25 with small kinetic energy are more important than the ones with a high kinetic energy, one can only take the plane waves that correspond to a kinetic energy up to a certain value:

$$E_{\text{cutoff}} \geq \frac{\hbar^2}{2m} ||k + G||^2 \tag{2.29}$$

By variation of E_{cutoff} one can include more or less plane waves and thus improve or corrupt a calculation. The number of included plane waves is therefore, besides the choice of the density of the $\mathbf{k}$-point mesh, one of the two crucial factors that immanently determine the computational cost and accuracy of a simulation and therefore have to be determined very carefully. Indeed within the computational setup these two parameters have to be varied until convergence is reached (for the computational details and convergence tests see appendix A and B).

Plane waves describe extended systems with periodicity perfectly well and therefore one of the best applications is within the uniform electron gas. When it comes to the description of the core orbitals of atoms however, plane waves are no good choice: One would need an extensive set of plane waves to describe these tightly bound orbitals at the core, where the true potential has a cusp and the wavefunction has many nodes. Yet, in contrast to the valence orbitals, the core orbitals do not participate in the chemical bond – they stay in principle where they are (so-called frozen-core approximation). Hence they can be approximated by pseudopotentials [73–75], which can be described by far smaller basis sets, i.e. far less plane waves. Within the pseudopotential approximation the wavefunction is replaced by a nodeless pseudo-wavefunction inside the core region. Outside this defined core region the pseudo-wavefunction mimics the true wavefunction exactly. How the (pseudo-) potential and (pseudo-) wavefunction are associated is shown in figure 2.3.

An important fact about pseudopotentials is that the total energies evaluated are no longer physically meaningful since the contribution of the core orbitals is only approximated – and by no means in the sense to describe it as good as possible, but merely to reduce the computational cost. Therefore only *differences* in total energies are meaningful. As core orbital total energies are by a factor of ≈ 1000 higher than the valence band orbital energies, the residual total energies due to the valence orbitals sum up to a comparably small value. And that is half the battle of the pseudopotential approach: As stated before, only differences in energies are useful to learn about the properties of a system – and the use of comparably small numbers to produce these differences leads to smaller numerical errors than doing so with higher number.

There are different classes of pseudopotentials [77]: Among the first approaches are norm-conserving pseudopotentials [78, 79]: As the name already implies, they are constructed so that the generated pseudopotential has the same norm as the corresponding all-electron wavefunction, i.e. the pseudocharge (and with that the pseudo electron density) within the core region has to match the true charge (and with that the true electron density) exactly. The norm-conserving condition was introduced to ensure transferability, but is known to cause problems especially for the $2p$ and $3d$ elements: For their highly localized orbitals it was shown that it is not possi-

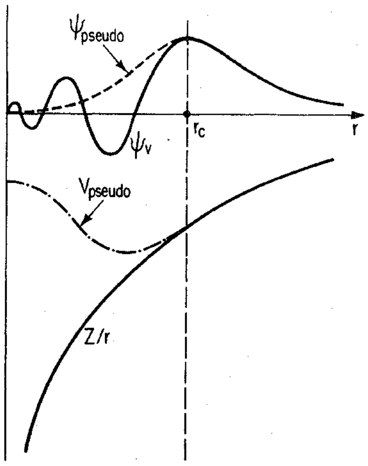

Figure 2.3: Schematic representation of all-electron (solid) and pseudoelectron potential (dashed line) and the corresponding wavefunctions. r_c denotes the radius where the pseudo- and the all-electron values match. Figure from Ref. [76]

ble to construct a considerably smoother pseudo-wavefunction than the all-electron wavefunction (without introducing huge errors an extensive basis set of planewaves is then still necessary to mimic the pseudo-wavefunction in these hard pseudopotentials). Ultrasoft pseudopotentials [80] can cure this deficiency: They no longer obey the norm-conservation criterion and produce much smoother pseudopotentials.

2.2.3 The supercell approach

The Bloch theorem calls for a periodic structure of the system of interest. As mentioned before the system investigated in this work is a surface structure (on which adsorbates interact). Such a surface shows periodicity just in two dimensions. Periodicity in the third dimension has to be introduced artificially by the so-called supercell approach. Here the simulation cell features a bulk part truncated in the positive as well as the negative z-direction. Above the two surfaces a vacuum region is introduced, dividing the two “slabs“ (for details see figure 2.4). The slab as well as the vacuum region have to be thick enough to prevent interaction of adsorbates either through the slab or the vacuum.

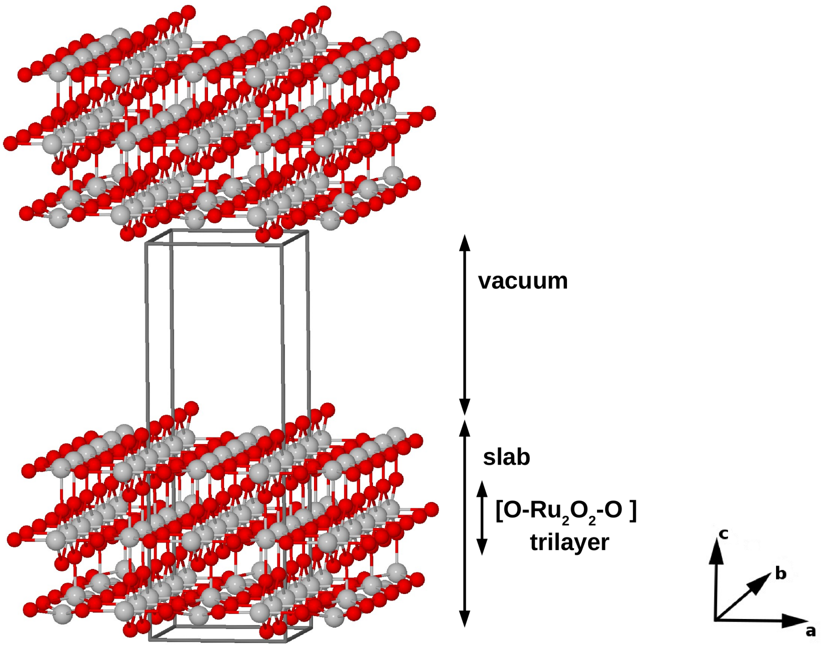

Figure 2.4: Schematic representation of the supercell approach: The unit cell (represented by the box) contains the slab as well as the vacuum region. To illustrate the periodicity of the system in all three dimensions the unit cell is extended in the a-, b- and c-direction.

2.2.4 Applications: binding energies and transition states

The concepts, as described in the preceding chapters, were applied within DFT calculations using the CASTEP (Cambridge Serial Total Energy Package) [81] code to calculate the total energy of a state of the system. To find the groundstate of a system, geometry optimization calculations were performed to identify the minimum energy configuration of a structure. In this configuration the forces acting on the nuclei[10] should vanish. These forces are evaluated following the Hellmann-Feynman theorem [82, 83]. The theorem establishes the connection between the force $F(x_i)$,

---

[10] arising from other nuclei and the electrons

the first derivative of the energy of the system, with the expectation value of its Hamiltonian H:

$$F(x_i) = \frac{\delta E}{\delta x_i} = \int \psi * (x_i) \frac{\delta H}{\delta x_i} \psi(x_i) \tag{2.30}$$

The forces are optimized using the scheme of Broyden, Fletcher, Goldfarb and Shanno (BFGS) [84–87] This geometry optimization technique is a so-called *quasi*-Newton method: The direction in which the nuclei are moved in order to optimize the structure with the Newton minimization technique is evaluated according to

$$x_{i+1} = x_i - \alpha_i [J_i]^{-1} \nabla F(x_i) \tag{2.31}$$

where α is the factor that minimizes the Hessian matrix $[J_i] = [\delta^2 F / \delta x_j \delta x_k]$ of the force F at x_i. In the *quasi*-Newton BFGS scheme the Hessian matrix J_i is not evaluated explicitly. Instead the BFGS method includes information about the previous optimization steps for an estimate of J_i. The *quasi*-Newton method is – at least within the region of the harmonic PES – superior to the also common conjugate gradient method [88] and the method of steepest descent [89]. The latter simply follows the PES downhill. The former indeed accounts for the gradient of the force but does not evaluate the second derivative of the force according to x_i.

The resulting groundstate and its assigned total energy can then be used to further evaluate the binding energy of an adsorbate as the difference between the total energy of the surface with the adsorbate and the total energy of the plain surface plus the total energy of the isolated adsorbate in the gas phase:

$$E_{\text{bind}} = -\frac{1}{N_{\text{Ads}}} [E_{\text{surf+Ads}} - (E_{\text{plain surf}} + N_{\text{Ads}} E_{\text{Ads,gas}})] \tag{2.32}$$

with N_{Ads} being the number of adsorbates. The algebraic sign was chosen so, that the positive binding energies indicates for exothermicity: The higher the value of E_{bind} the stronger the adsorbate binds to the surface.

Finding transition states and reaction pathways on the potential energy surface (PES)[11] are more demanding tasks since their search requires in general more than just three geometry optimization calculations, that are needed for the evaluation of a single binding energy. The nudged elastic band (NEB) method to find the minimum energy pathway (MEP) [90–92] as implemented in the Atomic Simulation Environment (ASE) package [93] was used to evaluate the transition states of the reactions. Within this method, first a band of $N-1$ images connecting an initial (IS) and final

---

[11] as mentioned before the BO approximation holds for all calculations done in this work. The PES is therefore an energy function $E(R_i)$ depending on the atomic coordinates R_i.

state (FS) along the reaction pathway of a system is constructed. Then the energy and the forces acting on each of the $N-1$ images of the band is evaluated. The band of images is then optimized to minimize the forces acting on each of the images in the band. Besides the true force $\nabla V(R_i)$ acting on any image, an artificial spring force F_i^S between neighboring images is introduced to ensure continuity of the band (see figure 2.5). The total force acting on an image i is then evaluated as

$$F_i = F_i^{\mathrm{S}} - \nabla V(R_i) \tag{2.33}$$

with the spring force F_i^{S}

$$F_i^{\mathrm{S}} = k_{i+1}^{\mathrm{S}}(R_{i+1} - R_i) - k_i^{\mathrm{S}}(R_i - R_{i-1}) \tag{2.34}$$

with the spring constant k^{S} and R_i the spatial vector of the image i. Two problems arise from this ansatz: If the spring forces between neighboring images are assumed to be very rigid, the band is not elastic enough to mimic pathways that are longer than the initial one, as the images can simply not move away from each other (keyword: 'cutting edge' problem). If the spring force is too weak so that the elongation of the band is possible, the images could drift away from each other pulled by the force $\nabla V(R_i)$ and the distances between the images would become very uneven. This would especially affect the most interesting region, the region where the transition state lies (keyword: 'sliding down' problem), and therefore this region would not be sampled adequately.

To overcome this shortcomings, certain contributions of both forces are projected out: This affects the orthogonal component of the spring force as well as the parallel component of the force $\nabla V(R_i)$ (see figure 2.5 for details). Eqn. 2.33 then becomes

$$F_i = F_i^{\mathrm{S}}|_{\parallel} - \nabla V(R_i)|_{\perp} \tag{2.35}$$

with

$$F_i^{\mathrm{S}}|_{\parallel} = F_i^{\mathrm{S}} \tau_{\parallel} \tau_{\parallel} \tag{2.36}$$

and

$$\nabla V(R_i)|_{\perp} = \nabla V(R_i) - \nabla V(R_i) \tau_{\parallel} \tau_{\parallel} \tag{2.37}$$

with $\tau_{\perp}$ and $\tau_{\parallel}$ being the unit tangent orthogonal and parallel to the path, respectively. By projecting out the orthogonal part of the spring force, this force only has an effect on the distance between the images, but not on the relaxation of the images orthogonal to the path. After locating the TS of a reaction, the activation energy of a forward- or backward reaction are then simply the differences between the energy of the TS minus the energy of the IS and FS, respectively:

$$\Delta E_{\mathrm{forward/\,back}} = E_{\mathrm{TS}} - E_{\mathrm{IS/\,FS}} \tag{2.38}$$

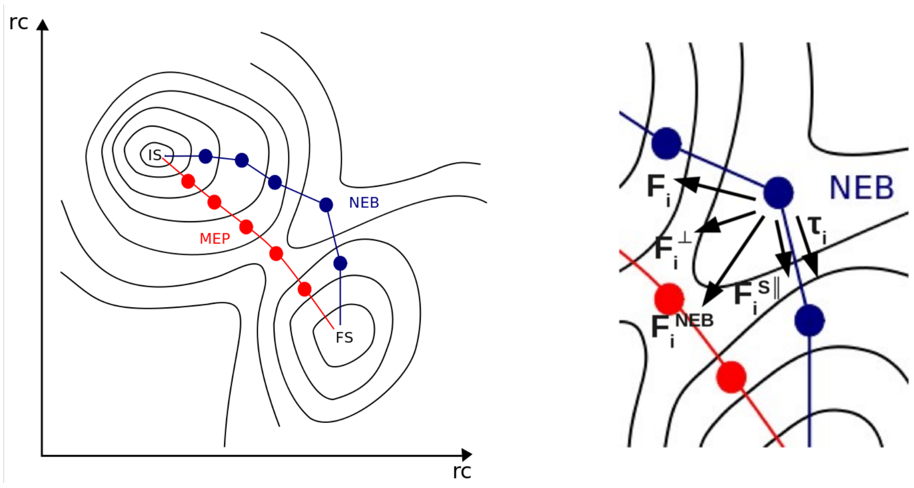

Figure 2.5: The minimum energy pathway (MEP) of a reaction can be found using the nudged elastic band (NEB) method: A band of images is created (left). After evaluation of their forces, the band is optimized so that the forces acting on an image are minimized. The forces acting on the images are decomposed (right): The total NEB force F_i^{NEB} consists of the parallel part of the spring force $F_i^{\mathrm{S}\|}$ following the tangent τ_i, and the orthogonal component $F_i^{\perp}$. F_i is the total force acting on each image (adapted from [94]).

The NEB method constitutes a rather demanding way for the evaluation of a MEP and its transition state. For really simple processes like the diffusion of a single atom from one site to another this method might be a bit over the top. A reasonable alternative for such simple cases is the so-called drag method [95]. Like in NEB a band of images between an IS and a FS is created within this method. For all images however, one coordinate is chosen to be fixed, while the other coordinates are free to change within a geometry optimization calculation. For the diffusion process of an oxygen atom between two identical sites the easiest approach would be a simple linear interpolation between IS and FS. The drag coordinate would then obviously be the direction back or towards the IS and FS respectively (with, in the present example, the TS located exactly midpoint between IS and FS for symmetry reasons). The MEPs as evaluated with the NEB method as well as the energy diagrams resulting from the drag-method are shown in appendix D. The binding energies E_{bind} and activation energies ΔE evaluated by a DFT calculation can then serve as input data for *ab initio* thermodynamics and harmonic transition state theory/ kinetic Monte Carlo, which will be described in the following chapters 2.3 and 2.4.

2.3 *Ab initio* thermodynamics

To access information about the composition on and of a surface, *ab initio* thermodynamics is a potent tool: This method allows to calculate the phase diagram of a certain system showing its various surface occupancies, and for that solely the binding energies of the adsorbates obtained with comparably cheap DFT calculations are needed. With that a connection between the microscopic and the mesoscopic regime on the time and length scale is established. The problem that has to be resolved thereby is the following: DFT is often referred to as a zero-temperature-, zero-pressure-method, i.e. all results derived by this method strictly only hold at $T = 0$ K, $p = 0$ atm. Yet these latter variables are the natural ingredients of a phase diagram. Therefore *ab initio* thermodynamics has to bridge concepts from DFT and classical thermodynamics [41–44]. How this is done within the framework of a 'constrained' equilibrium is shown in the following.

Studying a surface it is appreciated to find out, which occupancy of adsorbates on this surface is most stable in a certain T and p range. For this the key quantity is the Gibbs free energy of adsorption that can be expressed as a function of the surface free energy:

$$\Delta G^{\text{ads}}(p,T) = \gamma_{\text{slab}}(p,T,N) - \gamma_{\text{slab+ads}}(p,T,N,n) \tag{2.39}$$

where γ_{slab} is the surface free energy of the plain surface and $\gamma_{\text{slab+ads}}$ is the surface free energy of the surface slab with an adsorbate. The former depends on pressure p, temperature T and the number of particles N, the latter additionally on n, the number of particles that are adsorbed per unit area. This surface free energies γ represent the increase in internal energy, if a solid is cleaved so that two surfaces appear, i.e. the energetic cost of this endothermic process [96].

The Gibbs free energy G^{tot} of a solid exhibiting a surface with a surrounding gas phase consists of the following contributions:

$$G^{\text{tot}} = G^{\text{bulk}} + \gamma A + N\mu \tag{2.40}$$

with the Gibbs free energy contribution of the solid, G^{bulk}, the surface free energy γ of the size A and the chemical potential μ of the N gas phase molecules. In *ab initio* thermodynamics the major issue is that the system is assumed to be in thermodynamic equilibrium. Within this framework this system in equilibrium can be divided in several smaller subsystems, which are again in equilibrium, but do not necessarily have to be in equilibrium with each other. Introducing this concept of a 'constrained' equilibrium to the surface being in equilibrium with a gas phase reservoir above this surface (see figure 2.6), the surface free energy is

$$\gamma = \frac{1}{A}\left(G^{\text{tot}} + G^{\text{bulk}} - \sum_i N_i\mu_i\right) \tag{2.41}$$

for a system containing i components. Here the surface is assumed to be in equilibrium with each of the gas phase components separately to mimic the situation in heterogeneous catalysis [97–101]. The Gibbs free energy of adsorption of a two-component gas phase system, containing a species A and B, is then:

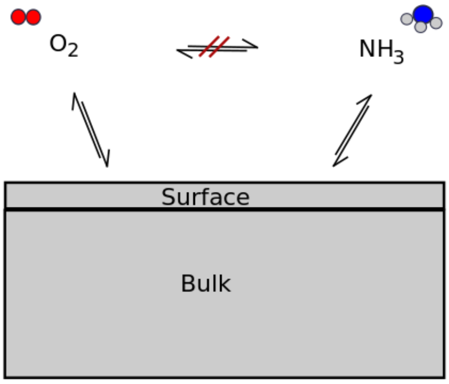

Figure 2.6: In a 'constrained' equilibrium the two subsystems are in equilibrium with each other, while the subsystems do not necessarily have to be in equilibrium: Here the two subsystems are the two gas phase components oxygen and ammonia, that are in equilibrium with the surface, but they are *not* in equilibrium with each other.

$$\Delta G^{\text{ads}} = \frac{1}{A}\left[(G^{\text{plain surf}} - G^{\text{bulk}}) - (G^{\text{surf+ads}} - N_A\mu_A - N_B\mu_B - G'^{\text{bulk}})\right] \tag{2.42}$$

If the number of atoms N in the bulk remains the same during the adsorption process, i.e. $G = G'$. With the expression for the chemical potential

$$\mu = E_{\text{tot}} - \Delta\mu \tag{2.43}$$

one arrives at the expression for the Gibbs free energy of adsorption as

$$\Delta G^{\text{ads}} = \frac{1}{A}\left[(G^{\text{plain surf}} - G^{\text{surf + ads}} + N_A(E_{A,\text{gas}} + \Delta\mu_A) + N_B(E_{B,\text{gas}} + \Delta\mu_B))\right] \tag{2.44}$$

For the evaluation of the difference between the Gibbs free energy of the plain surface and the surface including the adsorbate, the following expression is needed [102]:

$$G(p,T) = U + F_{\text{vib}} - TS^{\text{conf}} + pV \tag{2.45}$$

The first, and major term, the internal energy U (without ZPE) is what is derived from DFT calculations directly (via equation 2.32: $U = E_{\text{tot}}$). TS^{conf}, that stands for the configurational entropy, as well as pV have rather sparse contribution to the Gibbs free energy – therefore they are neglected in 2.44. Similarly, F_{vib}, that accounts for the vibrational free energy and provides indeed a non-negligible contribution to the Gibbs free energy of adsorption: In the *difference* between vibrational free energies in eqn. 2.44 its contribution might be small. This was shown for small adsorbates [5, 103]. In the present context, in particular for hydrogen containing adsorbates, this might no longer be fulfilled. Still, as a first approximation F_{vib} will be neglected in the following. Therewith one arrives at the following approximation for ΔG

$$(G^{\text{plain surf}} - G^{\text{surf + ads}}) \approx (E_{\text{tot}}^{\text{plain surf}} + E_{\text{tot}}^{\text{surf + ads}}) \tag{2.46}$$

Combined with the following expression for the binding energy of an adsorbate:

$$E_{\text{tot}}^{\text{plain surf}} + E_{\text{tot}}^{\text{surf + ads}} + E_{\text{tot},A} + E_{\text{tot},B} = -E_{\text{bind}} \tag{2.47}$$

one finally gets the working equation for the Gibbs free energy of adsorption:

$$\Delta G^{\text{ads}} = -\frac{1}{A} E_{\text{bind}} + N_A \Delta\mu_A + N_B \Delta\mu_B \tag{2.48}$$

This function for ΔG^{ads} depends on two chemical potentials and therefore one gets a three dimensional plot for the Gibbs free energy of adsorption of a two-component system on a surface. The most stable surface occupancy under certain (p, T) conditions is then the one that minimizes the surface free energy γ most. This means the surface occupancy that causes the *highest* Gibbs free energy of adsorption is the most stable one.

2.4 Transition state theory

Harmonic transition state theory (hTST) [38] establishes the connection between energetics calculated from first-principles (see previous chapter 2.2) and the process rate constants as the basis for kinetic Monte Carlo simulations (see following chapter 2.5). With DFT-NEB-calculations one can follow the minimum energy pathway of a reaction, and with this find its transition state (TS), which represents the maximum barrier within this trajectory. Having this picture of the resulting potential energy surface (PES) with an initial state (IS) and a final state (FS) as well as the TS in mind, hTST assumes that the process rate of a reaction can be approximated assuming the transition from an IS to a FS as an equilibrium flux from this IS through a plane (perpendicular to the reaction pathway) at the TS to the FS or the other way around from the FS through the plane at the TS of the PES back to the IS. This assumption neglects a recrossing of the plane (which marks the discrepancy to the Eyring theory from 1935 [104] which handles the recrossing with a prefactor $\kappa \leq 1$) – that means every trajectory that starts to cross the TS will end up in the IS or FS, respectively. However, as the plane, through which the flux is assumed to flow, is perpendicular to the minimum energy pathway (MEP) between IS and FS one can assume that the main flux will indeed take this direction and cross the saddle point of this trajectory (for illustration see figure 2.7). The process rate for a transition from one state i to another state j can then be expressed as follows [39]:

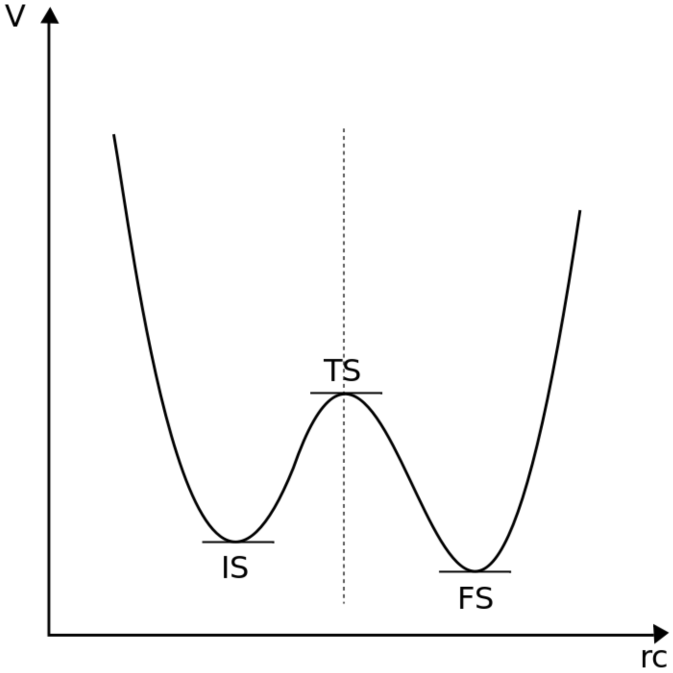

Figure 2.7: Schematic one-dimensional PES along a reaction coordinate (rc): The MEP from an initial state (IS) to a final state (FS) via a transition state (TS). After passing through the plane at the TS perpendicular to the MEP (indicated by the dotted line), recrossing is not possible within the framework of hTST.

$$k_{ij}(T) = f_{ij}(T)\frac{k_B T}{h}\exp\left(-\frac{\Delta E_{ij}}{k_B T}\right) \tag{2.49}$$

ΔE_{ij} is the energy barrier between the two states i and j, which comes from the first-principles DFT-NEB calculations. f_{ij} contributes to the harmonic modes of IS and TS:

$$f_{ij}(T) = \frac{q_{TS}^{\text{vib}}}{q_{IS}^{\text{vib}}} = \frac{\prod\limits_{i=0}^{N} \nu_i^{IS}}{\prod\limits_{i=0}^{N-1} \nu_i^{TS}} \tag{2.50}$$

where q^{vib} are the partition functions of the IS and TS, respectively, with N degrees of freedom. This simple expression for the process rate constants k_{ij} owes to the assumption that the vibrational modes of the IS and TS are harmonic, which means the degrees of freedom at the TS are only of vibrational nature. This holds only in case $h\nu \ll k_B T$. In the following chapters the preceding assumptions are used to evaluate the process rate constants for the four main process types considered in this work: adsorption, desorption, diffusion and reaction.

2.4.1 Reaction and diffusion

Along the lines of the assumptions made in the preceding chapter 2.4, the process rate constants for the diffusion and reaction processes can be calculated as follows:

$$k_{ij}^{\text{Diff}}(T) = f_{ij}(T)\frac{k_B T}{h} \exp\left(-\frac{\Delta E_{ij}^{\text{Diff}}}{k_B T}\right) \tag{2.51}$$

$$k_{ij}^{\text{Reac}}(T) = f_{ij}(T)\frac{k_B T}{h} \exp\left(-\frac{\Delta E_{ij}^{\text{Reac}}}{k_B T}\right) \tag{2.52}$$

Thereby the prefactor $f_{ij}(T)$ is assumed to be ≈ 1 within the whole work presented here. It was shown before [4] that this simplification is not the crucial factor when it comes to the treatment of atomic adsorbates or small molecules, as this only means that the vibrational modes of the TS and IS are assumed to be rather similar. A common simplification is to set the prefactor to $k_B T/h = 10^{-13}\text{s}^{-1}$. This represents an even more severe insection. However, the prefactor is not the crucial part in eqn. 2.51 and 2.52, as it only enters linearly. The systematic DFT error in ΔE in contrast can cause much more variance in the process rate constants: Though it lies in fact in the order of $\approx 200 - 400\,\text{meV}$, one has to consider, that these energy barriers enter in the exponent which means that also the error will also enter exponentially. If one remembers the differences in energy barriers that arise from different XC-functionals (see chapter 2.2) it becomes obvious that the ratio of the partition functions as a prefactor does not have a comparably high impact.

2.4.2 Adsorption

The adsorption process is more complicated than reaction and diffusion processes:

$$k_i^{\mathrm{Ads}}(T) = \underbrace{\frac{p_i A}{\sqrt{2\pi m_i k_B T}}}_{\text{Impingement}} \underbrace{f_i(T)\frac{A_{i,s}}{A}\exp\left(-\frac{\Delta E_i^{\mathrm{Ads}}}{k_B T}\right)}_{\text{Sticking}} \tag{2.53}$$

The first part comes from kinetic gas theory and describes the impingement rate of an adsorbate i [4,40]. Obviously this factor depends on the partial pressure p_i of this species in the gas phase and the area A of the surface unit cell. The second part of eqn. 2.53 defines how many of the impinging particles actually stick on the surface. This allows for the different possibilities the gas phase molecules have for orientation with respect to the surface, velocity and in their internal degrees of freedom. If the surface provides more than one active site, the term $\frac{A_{i,s}}{A}$ becomes crucial. It describes the active region within the surface unit cell that is activated for an adsorption process. For an one-site unit cell this fraction equals 1. The surface that is observed in this work has two adsorption sites, though just one plays a role in the surface chemical reactions (there is proof from theory as well as experiment that this second site plays no or only a minor role within the catalytic reaction network under the reaction conditions interesting for this work – for details see chapter 3). Furthermore it is assumed that during adsorption there is no barrier for the adsorbate to cross over, i.e. there is no TS. Together with the fraction $f_{ij}(T)$ approximated to be ≈ 1 the sticking coefficient is then simply 1 and the adsorption depends therefore solely on the impingement rate. This is indeed a rough approximation. Notwithstanding, similar to the discussion of the prefactors, one has to recognize that approximations to the sticking coefficient enter only linearly – and will be predominantly lead to shifts in the global pressure dependencies.

2.4.3 Desorption

The desorption process is the antagonist to the adsorption process and therefore the evaluation of these two process rate constants are connected by the detailed balance criterion that ensures the microscopic reversibility of the system (see [105] and equation 2.70 in chapter 2.5): In thermal equilibrium there are naturally as many adsorption as desorption processes. Therefore the two process rate constants are connected via the Boltzmann distribution:

$$\frac{k^{\mathrm{Ads}}(p,T)}{k^{\mathrm{Des}}(T)} = \exp\left(\frac{\Delta G(T,p)}{k_B T}\right) \tag{2.54}$$

where $\Delta G(T,p)$ is the Gibbs free energy difference between gas phase state and adsorbed state. This equation 2.54 can be approximated by

$$\frac{k^{\mathrm{Ads}}(p,T)}{k^{\mathrm{Des}}(T)} \approx \exp\left(\frac{\mu_{\mathrm{gas}}(p,T) - F(T)}{k_B T}\right) \tag{2.55}$$

by neglecting the pV term in the expression for the Gibbs free Energy of the adsorbed state ($G \approx F$) [101]. The gas phase chemical potential $\mu_{\mathrm{gas}}(p,T)$ can be separated into two parts

$$\mu_{\mathrm{gas}}(p,T) = E_{\mathrm{tot,gas}} + \Delta\mu_{\mathrm{gas}} \tag{2.56}$$

and so can the free energy $F(T)$:

$$F(T) = E_{\mathrm{tot,Ads}} + F_{\mathrm{vib}} = E_{\mathrm{tot,Ads}} - k_B T \ln z_{\mathrm{vib}} \tag{2.57}$$

Both are thus separated into their total energy and vibrational contribution, with z_{vib} being the partition function of the vibrational degrees of freedom of the latter. Putting this all together one arrives at the following expression for $\frac{k^{\mathrm{Ads}}(p,T)}{k^{\mathrm{Des}}(T)}$:

$$\frac{k^{\mathrm{Ads}}(p,T)}{k^{\mathrm{Des}}(T)} = \exp\left(\frac{E_{\mathrm{tot,gas}} + \Delta\mu_{\mathrm{gas}} - (E_{\mathrm{tot,ads}} - k_B T \ln z_{\mathrm{vib}})}{k_B T}\right) \tag{2.58}$$

In the low temperature regime, $T \to 0$, the entropic vibrational contribution to the free energy $F(T)$, the term $k_B T \ln z_{\mathrm{vib}}$, represents the zero-point energy (ZPE) of an adsorbate. At this level of theory these vibrations are neglected as consistent with the treatment in *ab initio* thermodynamics. Later, on the level of Monte Carlo simulations with sensitivity guided analysis, it will be tested, if this disregard is justified by explicit evaluation of the ZPE for selected molecules and analysis of its effect on the binding energy of the single adsorbate and the interplay of events within the reaction network. This approximation yields the following simplified expression for the desorption energy:

$$\frac{k^{\mathrm{Ads}}(p,T)}{k^{\mathrm{Des}}(T)} \approx \exp\left(\frac{-E_{\mathrm{bind}} + \Delta\mu_{\mathrm{gas}}}{k_B T}\right) \tag{2.59}$$

with $E_{\mathrm{bind}} = -E_{\mathrm{tot,gas}} + E_{\mathrm{tot,Ads}}$. This then leads to the following 'working' equation for the process rate constants of desorption:

$$k^{\mathrm{Des}} = k^{\mathrm{Ads}} \exp\left(\frac{-E_{\mathrm{bind}} - \Delta\mu_{\mathrm{gas}}}{k_B T}\right) \tag{2.60}$$

2.4.4 The chemical potential for simple molecules

A detailed expression for $\Delta\mu$ [103] is

$$\Delta\mu_{\mathrm{gas}} = -\frac{1}{2} k_B T \left[z_{\mathrm{trans}} + z_{\mathrm{rot}} + z_{\mathrm{vib}} + z_{\mathrm{elec}}\right] \tag{2.61}$$

with several partition functions z_{xx} for the translational, rotational, vibrational and electronic degrees of freedom:

$$z_{\text{trans}} = \left[\left(\ln \frac{2\pi m k_B T}{h^2} \right)^{\frac{3}{2}} \frac{k_B T}{p} \right] \tag{2.62}$$

$$z_{\text{rot}} = \left[\ln \left(\frac{k_B T}{\sigma B_0} \right) \right] \tag{2.63}$$

This equation for the rotational degrees of freedom comes from the rigid rotator approximation and holds only for the case of diatomic molecules: $\sigma = 1$ for the number of indistinguishable orientations of the hetero-atomic molecule and $\sigma = 2$ of the homo-atomic molecule respectively (with $B_0 = \frac{\hbar^2}{2I}$ and $I = mr^2$). For bigger molecules (containing more atoms) the expression for z_{rot} is not straightforward and different approaches have to be applied (see 2.4.5).
The expression for z_{vib} is derived within the harmonic oscillator approximation:

$$z_{\text{vib}} = \left[-\ln \left(1 - \exp \left(\frac{\hbar \omega_0}{k_B T} \right) \right) \right] \tag{2.64}$$

with $\omega_0 = 2\pi\nu_0$ and $\nu_0 = \sqrt{\frac{k}{\mu_m}} \frac{1}{2\pi}$, with k being a force constant and μ the reduced mass $\mu_m = \frac{m_1 m_2}{m_1 + m_2}$. Finally the last contribution to the partition function is

$$z_{\text{elec}} = [\ln (I_{\text{spin}})] \tag{2.65}$$

with $I = 2s + 1$ being the electronic spin degeneracy.

2.4.5 The chemical potential for complex molecules

An approximation via the ideal gas law as was done in section 2.4.4 is only straightforward for small molecules like homo- and hetero-atomic dimers as they provide simple expressions for σ and B_0 (from eqn. 2.63). For more complex molecules however the evaluation of these terms are complicated. An easier way to evaluate $\Delta\mu$ is shown in [101] where the chemical potential is calculated using well defined and established thermodynamical parameters to solve the following equation:

$$\mu(p, T) = \mu(p^0, T) + kTln \left(\frac{p}{p^0} \right) \tag{2.66}$$

with

$$\mu(p^0, T) = \mu(p^0, T) + \Delta G(p^0, \Delta T) \tag{2.67}$$

Using the relation $G = H - TS$ between the Gibbs free energy and the enthalpy and entropy one arrives at

$$\mu(p^0, T) = \left[\Delta H(p^0, \Delta T)\right] - \left[\Delta S(p^0, \Delta T)\right] \qquad (2.68)$$

and the differences ΔH and ΔS with respect to the $T = 0$K limit can be calculated using the values listed in the thermodynamic tables [106]. For the simple case of the O_2 molecule, the two methods in section 2.4.4 and 2.4.5 were compared and the results were indistinguishable [103].

2.5 Kinetic Monte Carlo simulations

As mentioned above kinetic Monte Carlo (kMC) simulations act in the mesoscopic interval of time and length scales and represent the technique used in this work to simulate the statistical interplay of all events of a (catalytically driven) reaction network on a (metal catalyst) surface [107–109]. More precisely, with this method one can follow the trajectory of a system from state to state over a certain time span. The virtues of kMC can most suitably be explained by comparison with other techniques: Molecular dynamics (MD) is as well as kMC a commonly used method to investigate the movement of an ensemble of atoms or molecules. Within the MD framework the vibrational modes of an adsorbate are explicitly resolved. These thermal movements are omitted in a kMC simulation: Concentrating only on the rare events – namely the reactions, diffusions, adsorptions and desorptions – kMC is coarse-graining the simulation events. The advantage of doing so is the gain on the time scale: While MD is able to cope with simulation times in the picosecond regime[12], kMC can run simulations for up to seconds or even minutes. This is essential when it comes to the investigation of the interplay of the rare events on a surface, as these events take place on a picosecond timescale and therefore can merely happen very seldom during an MD simulation which itself runs only for a few picoseconds – by all means not often enough to get statistically meaningful answers. (For an illustration of the PES of the rare events and the vibrational motion see figure 2.8)

Aiming at comparably long simulation times, a mean field approximation via rate equations would be a strong candidate to do the simulation job. Within this framework the process rate constants are determined by the same set of differential equations like the ones solved in kMC, but they are simplified so that this approximation does not account for the actual spatial configuration of the adsorbates on the surface, but treats the occupancy of the adsorbed species on a surface only as an average –

---

[12] with nowadays available computer power

therefore a mean field model gives incorrect answers the more the surface distribution deviates from a random mixture. A kMC simulation in contrast *does* account for the exact spatial distribution of the absorbates at any time of the simulation. Especially for the case of a low-dimensional model as used in this work (see chapter 3) this is a crucial point.

Though kMC has its disadvantages – it is no longer deterministic and processes have to be chosen explicitly (see section 2.5.2 for more details) – kMC is the method of choice as it provides long enough simulation times to account for the rare events and is high enough in configurational accuracy.

The kMC algorithm used in this work follows the work of Bortz, Kalos and Lebowitz (BKL) [110] and Gillespie [111]. It is a rejection-free code and therewith among the most efficient kMC algorithms.

In this work the target quantity of a kMC simulation is the turnover-frequency (TOF) of a system under defined (p-, T-) conditions in steady state. This TOF defines how many product molecules of a given species are formed and desorb per site and second (TOF [$\mathrm{s}^{-1}\,\mathrm{site}^{-1}$]).

2.5.1 The machinery of a kMC algorithm

The basis of a kMC algorithm is a Markov state-to-state dynamics, described by the master equation 2.69:

$$\frac{dP_i}{dt} = \sum_{j \neq i} k_{ji} P_j(t) - \sum_{j \neq i} k_{ij} P_i(t) \tag{2.69}$$

This equation, 2.69, describes the evolution of the time-dependent probability density function $P_i(t)$ to find the system in a state i. This approach is particularly suitable as the general idea of kMC is the coarse graining of the motion of atoms and molecules to rare events: By focusing only on these long-time scale events, one can assume that the system performs its vibrational motion for long enough time, that it has forgotten, where it came from. It is completely independent from its former state(s), and therefore the probability density $P_i(t)$ of a state i is solely the sum over the probabilities of reaching this state minus the sum over the probabilities for leaving this state, while the sum runs over all possible system states j. The probabilities for the states P_i are weighted by the process rate constants k_{ij} which are evaluated by transition state theory (for details how these process rate constants are evaluated for the several events see chapter 2.4).

The kMC algorithm now provides a numerical solution of the differential equations

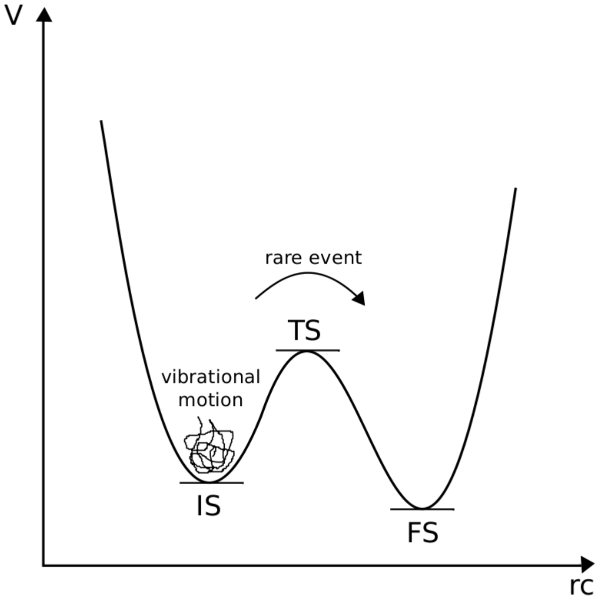

Figure 2.8: Schematic one-dimensional PES along a reaction coordinate (rc): A so-called 'rare event' – adsorption, desorption, reaction or diffusion – is performed, while the thermal motion lets the molecule just oscillate within the same potential energy minimum for a comparably long time.

2.69 to generate a chain of successive states of a system[13]. The detailed-balance criterion [105] has to be fulfilled to bring the therewith described canonical ensemble to thermal equilibrium:

$$k_{ji} P_j^{\mathrm{eq}} = k_{ij} P_i^{\mathrm{eq}} \tag{2.70}$$

For P_i being the equilibrium probability density for a transition from state i to state j, thermal equilibrium is reached when there are as many crossings to state j as recrossings to state i. For everyday kMC simulations this means reversibility of the processes has to be provided, i.e. it is a must that forward and backward reactions both are considered.

The first step to start a kMC process is the definition of an appropriate lattice and

---

[13] An analytical solution of the differential equations is not amenable, as the number of accessible sites grows exponentially. For a standard kMC simulation it is common practice to use 20 to 100 sites.

a process list: Both depend strongly on the system, and in particular the latter has to be chosen with caution (for details see 2.5.2).

In the beginning of a kMC simulation, a list of all processes that are possible for the current configurational condition of the system is compiled. Then the corresponding process rate constants are summed up to a total process rate K_{tot}:

$$K_{\text{tot}} = \sum_p k_p \tag{2.71}$$

where p is the number of processes. From this bunch of processes, one is selected via picking its process rate with the help of a random number $\rho_1 \in]0,1]$:

$$0 > \rho_1 K \geq K_{\text{tot}} \tag{2.72}$$

Thereby the process that has a higher process rate is more likely to be picked than a process with a smaller process rate. This can be illustrated as playing roulette in an 'unfair' way, namely with a roulette wheel that has disparate sections, representing the process rate constants for the different events that can take place on the surface. After the chosen process is performed, the configuration on the surface is updated.

The next step is the time update $t \rightarrow t + \Delta t$. This is again done with the help of a random number $\rho_2 \in]0,1]$:

$$\Delta t = -\frac{\ln \rho_2}{K_{\text{tot}}} \tag{2.73}$$

The time interval Δt depends on the process rate constants: The higher the process rate is, the shorter is the interval Δt, i.e. the time to leave a state. This perfectly makes sense as the higher the process rate constants are, the lower the stability of a state should be and therefore it should be able to escape more easily. This holds for a single process rate k_{ij} as well as for the total process rate K_{tot}. In the latter case one has to keep in mind that the time that has expired during one kMC step does *not* depend on that single process rate of the process that was accomplished, but on the whole ensemble of processes and their rate constants respectively. It was shown that the trajectory simulated with kMC follows a Poisson process and therefore the time that is expiring in kMC is connected to the real time [112].

Finishing the time update, the kMC simulation can start a new cycle with a new surface (lattice) configuration. The kMC simulation is done, when an initially defined system time t_{max} is reached. For an overview over the several steps of the kMC cycle see flowchart 2.9.

2.5.2 Limitations of kMC

For a reliable kMC algorithm, the choice of input reactions is essential to get the right interplay of reactions. The exact result would obviously come with a full set of

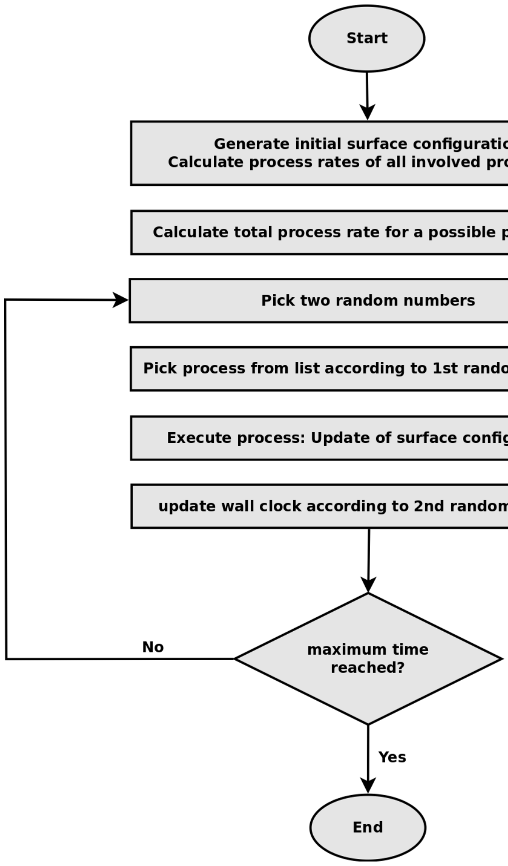

Figure 2.9: Flowchart for the cycle of a kMC simulation.

all reactions that actually happen on the surface or – if this set of reactions is not known – a set of all possible reactions that *can* occur. For simple reactions this will work. For more sophisticated reactions however, it is difficult to identify all possible reaction pathways just from chemical intuition. This becomes obvious if one thinks of complex reaction steps – for example concerted reactions between three or even more reactants. Furthermore the mere number of imaginable reactions can get extremely high so that the kMC approach can become simply not feasible with an *ab initio* kMC simulation.

Another obstacle in kMC can be huge differences in the process rate constants. If there is a process with a rather small process rate, it can happen that this process will be performed on and on. This does not increase the wall clock of the simulation too much, but simply leads to the technical problem that one has to run a very long kMC simulation in terms of computational time until one of the processes with lower probability occurs. This is more likely to be the case the more processes a kMC algorithm contains. Several workarounds have already been tested, for example coarse grained kMC [113].The mere number of processes[14] can also become a bottleneck of the simulation: As mentioned above, the progress of time within a kMC simulation depends always on *all* process rate constants. If there are many, the single process rate constants do not even have to be too big, but by summing all up one can still end up with a large total process rate K_{tot} – and this means small time increments which come with a longer simulation time until a certain wall clock time within the simulation is reached.

2.6 Sensitivity guided analysis

As already mentioned in chapter 2.5.2, the choice which reactions are taken into account in a kMC simulation is crucial: The more reactions are involved, the more complicated the situation gets. And considering *all* reactions can easily lead to an unmanageable number of events if one asks for a reliable set of process rate constants based on first-principles calculations. Yet to leave reactions out could mean to miss *the one* essential reaction – and the question which reaction is important and which is not (so) important can, if it comes to a complex reaction network, only be answered by statistical methods like kMC. Addressing such networks within the conventional approach pursued in first-principles kinetic Monte Carlo simulations would incur a prohibitive computational cost: First-principles calculations of the kinetic parameters (prefactors and energetic barriers) would be performed for every potentially possible elementary process, only to find out that many (most) of these processes are not rate-controlling: Some are completely irrelevant, others are required to close the catalytic cycle but whether they happen much faster or slower would not affect the overall turnovers and selectivities. These processes are not the bottlenecks or so-called rate-limiting steps.

Acknowledging this a novel approach will be explored in this work based on a sensitivity-analysis guided refinement. The statistical simulations are initiated with a core set of elementary processes that are described at the first-principles level. Additional processes, likewise on a first-principles level or at a low-level description, will then be added stepwise. The selection of these further processes will be based on

---

[14] either caused by a huge system size or a long process list

the knowledge adopted from the preceding simulations. Using the correspondingly refined kinetic parameters for the latter steps the simulations will be re-initiated and potentially refined until a consistent description has been reached. It is expected that this procedure, which concentrates the first-principles calculations on a subset of all feasible elementary processes, will reduce the computational burden to an extent to make also more complex reaction networks and their sensitivity features amenable to the detailed investigation by first-principles microkinetic modeling.

2.7 Summary

The here described methods, DFT, hTST, kMC as well as *ab initio* thermodynamics, are well established within their inherent time- and length scales. Connecting them within a computational multiscale modeling approach to cover the different regimes of time and space introduces interesting prospects and opportunities for reaction modeling and prediction. However, as described above, each method has its limitations and therefore introduces errors – therefore each step has to be handled carefully, especially having regard to the system that is treated. Executing the multiscale modeling approach to a complex network introduces a new dimension of instability to the methodology (especially within kMC) and therefore the strategy is to use the most standardized and best established *versions* of the afore mentioned methods to put the whole framework of the multiscale modeling approach on a basis with as few and small errors as possible[15]. With that it is believed that the sensitivity guided multiscale modeling approach can provide insights into even complex reaction processes that are not accessible via experiment. An overview over all methods, how they are following up and depend on each other, is shown in diagram 2.10.

---

[15] For DFT this means to stick to the well established XC-functionals, for kMC not to apply various kMC schemes like the above mentioned coarse-grained kMC

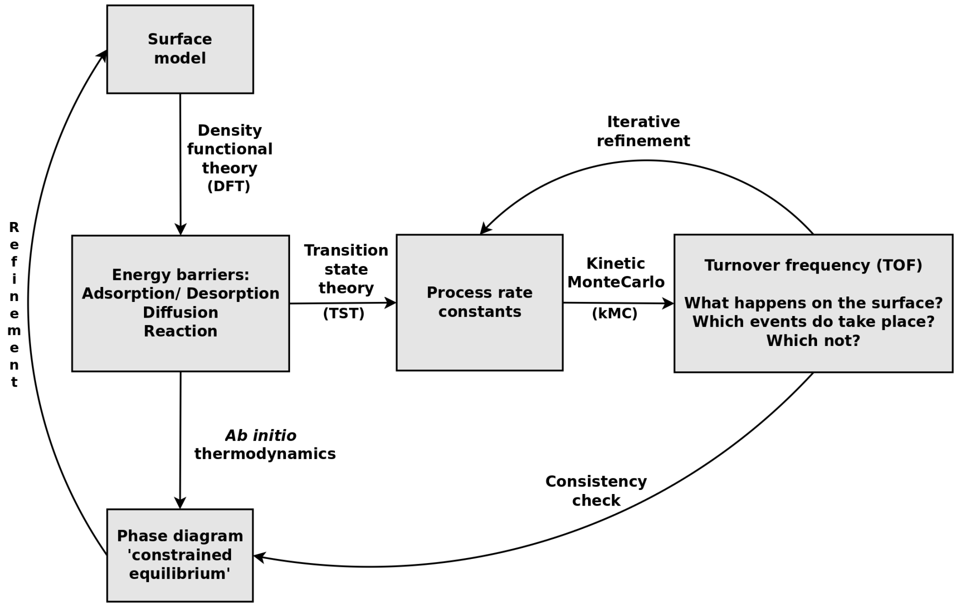

Figure 2.10: Overview over the methods used in this work: The energy barriers and binding energies calculated with density functional theory are the basis for the process rate constants, evaluated within harmonic transition state theory. The process rate constants are in turn the basis for the kinetic Monte Carlo simulations that provide the statistical interplay of the reaction network. Which process rate constants are important can already be curtailed by the *ab initio* thermodynamics phase diagram as it provides information about a sensible surface model. Extension and refinement of the list of process rate constants are developed by a sensitivity guided analysis.

Chapter 3

Results

3.1 Introductory remarks

In the following chapter the approach for a detailed description of the oxidation of ammonia to nitrogen monoxide and molecular nitrogen on $RuO_2(110)$ will be presented: Results from DFT calculations as well as kMC simulations will give insights into the individual steps of this complex reaction network – also in view of the special surface configuration. Furthermore already performed research on this issue, mainly experimental work, will be discussed to understand, to underline, but also to verify the findings obtained in the work presented here. These are mainly the experiments of Wang *et al.* [1] who investigated the oxidation of ammonia on the $RuO_2(110)$ surface with $\underline{t}$hermal $\underline{d}$esorption $\underline{s}$pectroscopy (TDS) and $\underline{h}$igh $\underline{r}$esolution $\underline{e}$lectron $\underline{e}$nergy-$\underline{l}$oss $\underline{s}$pectroscopy (HREELS), as well as steady-state reaction kinetics experiments. These experiments were performed under UHV conditions. Further support will come from the experiments of Perez-Ramirez *et al.* [14] who investigated the system under *ambient* pressure.

3.2 The structure of the surface

Before starting with the compilation of conceivable reaction steps, the surface structure and accordingly the dominant adsorption sites on the catalyst surface have to be determined. There is clear evidence for the active sites on the $RuO_2(110)$ facet from experiment [1] as well as from theory [4]: These active sites are the $\underline{c}$oordinatively $\underline{u}\underline{n}\underline{s}$aturated sites (*cus* sites) above five-fold coordinated surface Ru-atoms and the $\underline{b}\underline{r}$idge (*br*) sites occupied by the oxygen atoms in the stoichiometric termination. Both site types are arranged in rows (see figure 3.1 for details).

Two different adsorption sites imply four different possible combinations how two one-fold surface coordinated adsorbates can interact and react with each other: both

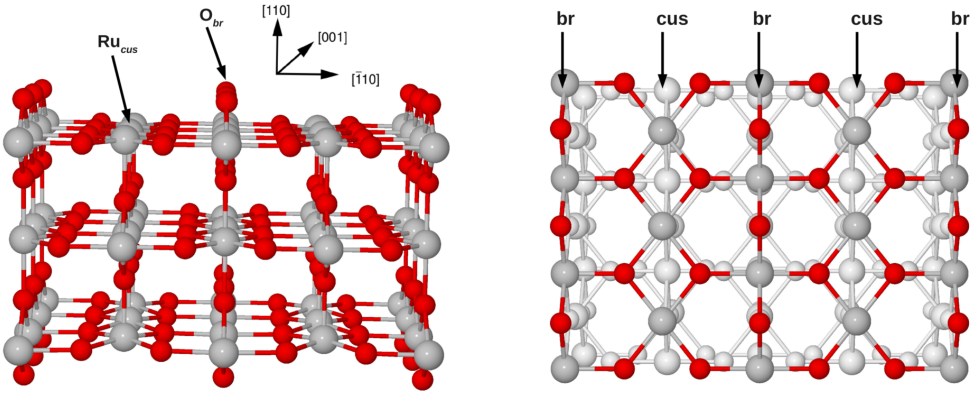

Figure 3.1: Stoichiometric $RuO_2(110)$ surface: Side (left) and on-top view (right) (Oxygen: red, ruthenium: grey, for the on-top view: atoms in deeper layers: white)

on *cus* sites, both on *br* sites, the first adsorbate on a *cus* and the second on a *br* site, or the second on a *cus* and the first on a *br* site. For this reason the list of processes to describe the reaction network within a kMC simulation, no matter how long it will be in the end, would have to be multiplied by four as all four possible combinations have to be considered. Notwithstanding experiment and theory agree in the fact that the oxygen atoms bind strongly to the *br* sites: It was shown experimentally that in the temperature and oxygen partial pressure range important for this work (temperatures around 500 K and pressures of 10^{-10} atm and higher), the *br* sites are fully occupied with oxygen. This is also reflected in the *ab initio* phase diagram for $RuO_2(110)$ (see figure 3.2 and 3.3) based on the calculated binding energies (see table 3.1) for ammonia and oxygen.

The binding energies of the adsorbates are coverage-dependent: If the whole surface is covered ($\hat{=}$ one mono layer(1 ML)) with ammonia, the molecules will not bind as strongly to the surface as if only every second site is occupied with NH_3 (0.5 ML). This destabilizing lateral interaction is due to the steric hindrance of this bulky molecule. The same effect, but much less distinct due to its slender shape can be found for the oxygen adsorbate. It has to be pointed out though that the low binding energy for the latter applies only for the case of the molecular reference, namely the oxygen *molecule* in the gas phase, as the oxygen desorption is known to be an associative process [4, 6].

The phase diagram shows that even at partial pressures as low as 10^{-15} atm for am-

Adsorbate	Coverage [ML]	E_{Bind} [eV]
NH_3	0.5	1.51
NH_3	1	1.15
O (molecular ref.)	0.5	0.98
O (molecular ref.)	1	0.94
NH_3 (+ O)	1	1.80
O (+ NH_3)	1	1.27

Table 3.1: Binding energies of the main adsorbates ammonia and oxygen (with respect to the coverage: 1 ML ≙ one mono layer).

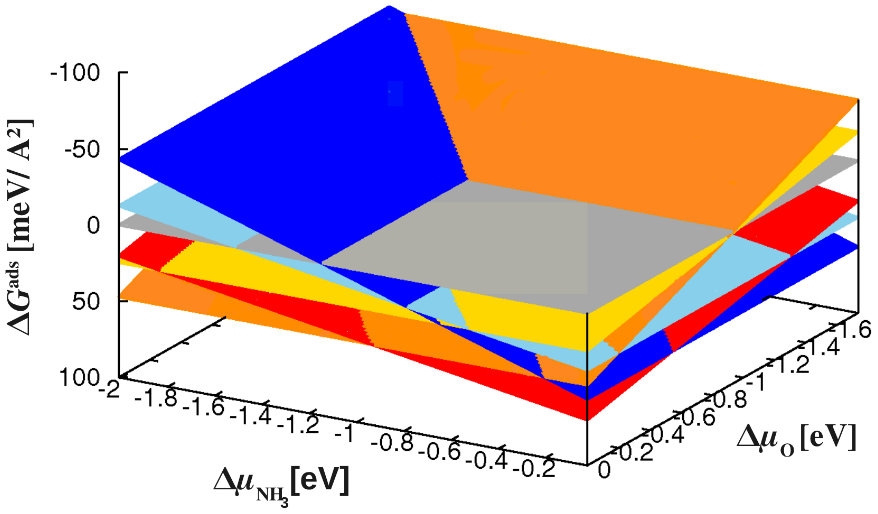

Figure 3.2: 3D *ab initio* phase diagram based on the binding energies listed in table 3.1: The surface free energy of adsorption ΔG^{ads} vs. the chemical potentials of oxygen, μ_{O}, and ammonia, $\mu_{\mathrm{NH_3}}$. The occupancy that minimizes the surface free energy (and with that maximizes ΔG^{ads}) is the most stable one. The most stable occupancies can be seen by looking on the *bottom* of this plot (see diagram 3.3).

monia and 10^{-25} atm for oxygen the *br* sites are occupied with oxygen. This sound agreement between theory and experiment allows for a preliminary simplification for the definition of a set of processes: Reactions will only take place between adsorbates on *cus* sites, viz. along one *cus* row. For the time being the *br* sites will thus be

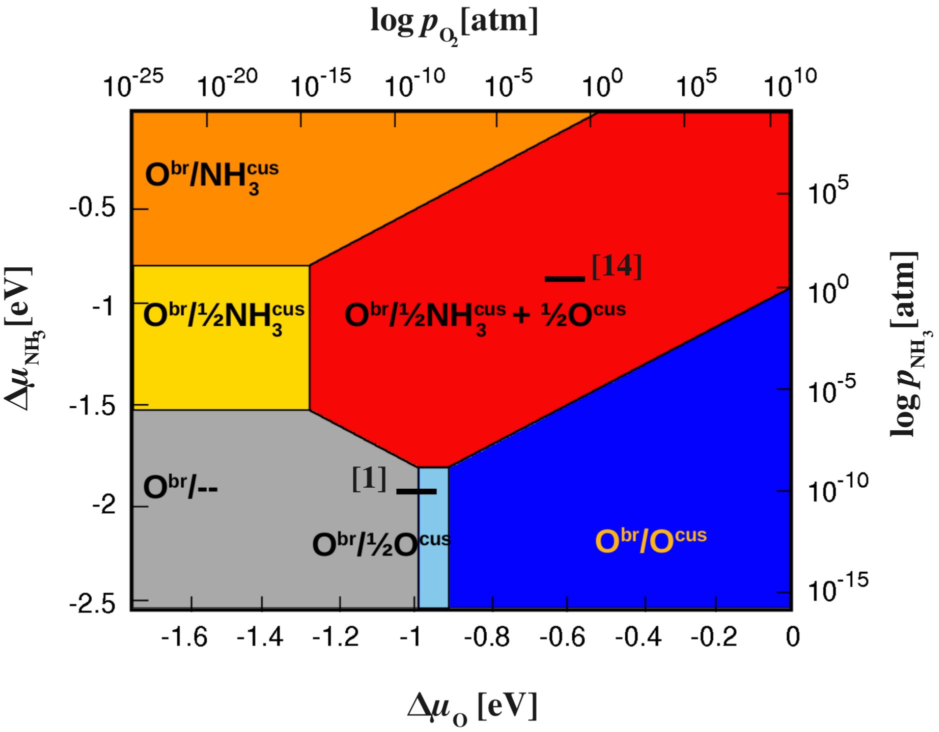

Figure 3.3: 2D phase diagram of the $RuO_2(110)$ surface at $T = 500\,K$ accounting for ammonia and oxygen: The black lines indicate the pressure range in which experiments of Wang *et al.* [1] and Perez-Ramirez *et al.* [14] were performed. Within the whole pressure range displayed the *br* sites of the surface are fully occupied with oxygen.

considered as oxygen-poisoned and not reacting with the neighboring adsorbates on the *cus* sites. Also adsorption and desorption processes from or to these sites are excluded. However, interaction, for example hydrogen bonding, between adsorbates on *cus* sites and the oxygen atoms on the *br* sites will naturally be considered. This way, the occupied *br* sites will serve as a natural border so that no interaction or reaction between *cus* sites of different *cus* rows can take place. Therefore the number of reactions that have to be considered will stay manageable within this approach.

The configurational degrees of freedom for the adsorbates are shrunk, since they can only react and diffuse along a one-dimensional chain of sites.

The phase diagram furthermore reveals that the population of the *cus* sites with ammonia starts at a NH_3-pressure of around 10^{-5} atm while oxygen coverage starts at an O-pressure of $\approx 10^{-8}$ atm. The phase in which both ammonia and oxygen are adsorbed on the surface covers already lower pressure ranges of ammonia and oxygen due to the cooperative lateral interaction of the adsorbates on each others binding energies ($\approx 10^{-15}$ atm for oxygen and $\approx 10^{-9}$ atm for ammonia): The molecules establish a hydrogen bond that tightens the whole ensemble. The pressure range in which the UHV experiments of Wang *et al.* [1] were performed correspond to a region of the phase diagram were only few *cus* sites should be occupied with oxygen and no NH_3 is expected. This region is certainly very close to the region where ammonia and oxygen coexist. As the straight lines in the phase diagram can not be taken as strict borders but rather represent the center of smooth transition regions, it is expected that the surface exhibits both ammonia and oxygen adsorbates, though in a rather low amount, leaving many *cus* sites empty. Initial kinetic Monte Carlo (kMC) simulations that account only for the adsorption, diffusion and desorption of the two main species (and with that thereby account for the configurational entropy at $T = 500\,\mathrm{K}$) reveal that at a pressure of 1.0×10^{-10} atm for both species the surface is indeed occupied with NH_3 and O: Ammonia covers around 25 % of the sites, while oxygen occurs at an average of 40 %. 35 % of the sites are empty. By lowering the oxygen pressure the amount of oxygen drops naturally, while the amount of ammonia initially increases because of the gained free sites on the surface. It then starts to drop according to the drop of oxygen atoms on the surface as the cooperative effect between these two adsorbates is lost. For a higher oxygen pressure ($\approx 10^{-9}$ atm) the O atoms displace the NH_3 molecules as well as the empty sites until the surface is completely covered with oxygen. This corresponds to a movement along a horizontal line within the phase diagram, which finally leads to the oxygen-rich phase, where indeed no ammonia molecules are expected on the surface.

Lowering the ammonia pressure instead corresponds to a vertical movement within the phase diagram and leads to depletion of ammonia until at $p_{\mathrm{NH}_3} \approx 10^{-15}$ atm no more NH_3 molecules can be detected on the surface. Certainly the amount of oxygen atoms increases with a decrease of the ammonia pressure, although the same effect can be expected as for lowering the oxygen pressure at fixed ammonia pressure: As discussed above the oxygen adsorbates also profits from the cooperative effect and bind therewith stronger if an ammonia molecule is adjacent. Therefore the oxygen atoms should also desorb more easily if the density of ammonia molecules decreases. However, in contrast the amount of oxygen on the surface increases! The reason for this odd behavior is that the process rate constants of these processes play in different regimes: The process rate constant for the *desorption* rate of ammonia is very high compared to its *adsorption* rate, and the neighboring effect of oxygen brings down the desorption rate in the vicinity of its corresponding adsorption rate. In contrast, the desorption rate of oxygen is *already* within the same range as its adsorption rate. An ammonia neighbor only lowers the process rate constant of desorption for oxygen even more, but this does not have any further effect on the desorption rate. This is reflected in the *ab initio* phase diagram where a vertical movement towards higher ammonia pressure (with fixed $p(O_2) = 10^{-10}$ atm) leads to the phase in which oxygen and ammonia are both present on the surface. The results of the kMC simulations displaying the evolution of the coverage with varying oxygen and ammonia pressures respectively are summarized in the diagrams 3.4 and 3.5.

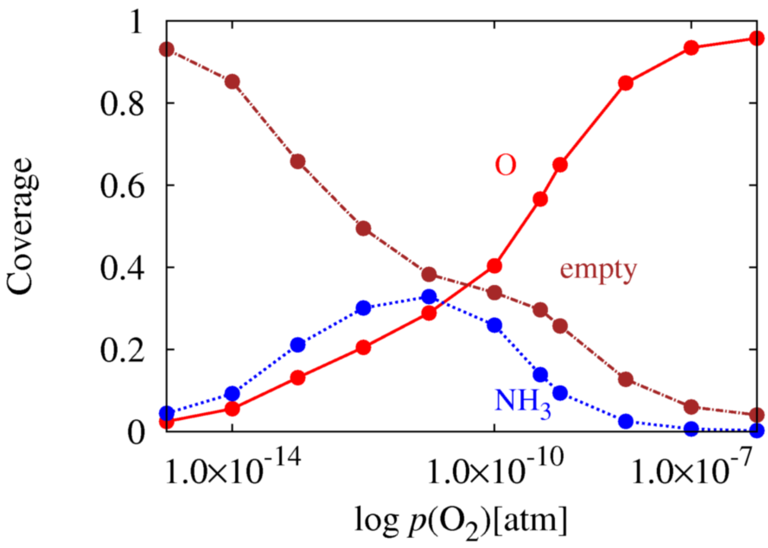

Figure 3.4: Evolution of the coverage of the surface with ammonia and oxygen for varying oxygen pressure; $p(NH_3) = \text{const} = 1.0 \times 10^{-10}$ atm (according to restricted kMC simulations (see text)). Red straight line: oxygen, blue dashed line: NH_3, brown dashed-dotted line: empty sites.

The experiments under ambient conditions [14] correspond clearly to the mixed oxygen/ ammonia phase – the borders to other phases are several orders of magnitude away in both directions. This could already be an explanation, why the progress

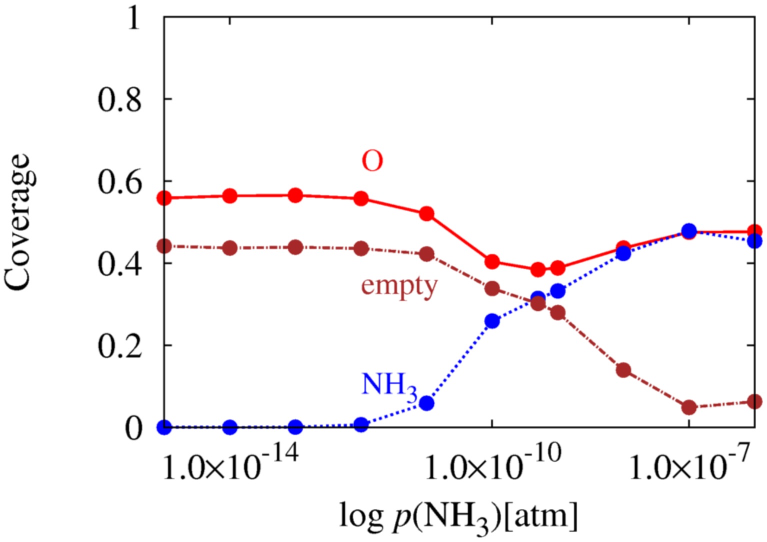

Figure 3.5: Evolution of the coverage of the surface with ammonia and oxygen for varying ammonia pressure; $p(O_2) = \text{const} = 1.0 \times 10^{-10}$ atm (according to restricted kMC simulations (see text)). Red straight line: oxygen, blue dashed line: NH_3, brown dashed-dotted line: empty site.

of the turnover frequency (TOF) escalates with increasing pressure within the UHV experiments [1], while it changes rather smoothly for the experiments under almost ambient pressure [14]: For the latter, no transition between different phases has to be accomplished. Furthermore the coverage on the surface is different – though the ratio of oxygen to ammonia pressure corresponds to the UHV experiments: At ambient pressure the *ab initio* phase diagram predicts a high population. KMC simulations with an ammonia pressure between 2.0×10^{-2} and 5.0×10^{-2} atm and an oxygen pressure between 1.0×10^{-1} and 2.0×10^{-1} atm indeed show that virtually all sites on the surface are covered with ammonia and oxygen almost half and half (with a slight tendency towards more oxygen), leaving only very few sites empty ($\approx 1 - 2\,\%$).

3.3 The reaction network – the basis reactions

Although the oxidation of ammonia has only two initial reactants – ammonia and oxygen – the involved elementary steps leading to one of the two main products (NO

and N_2), comprising adsorption, desorption, diffusion and reaction events, are manifold (for a list of possible reactions see appendix C). From chemical intuition the most important reactions among these are the following:
The stepwise dehydrogenation of NH_x species occur via oxygen or hydroxyl groups:

$$\mathrm{NH_x + O \rightleftarrows NH_{(x-1)} + OH} \tag{3.1}$$

$$\mathrm{NH_x + OH \rightleftarrows NH_{(x-1)} + H_2O} \tag{3.2}$$

or spontaneous dehydrogenation of the NH_x species:

$$\mathrm{NH_x \rightleftarrows NH_{(x-1)} + H} \tag{3.3}$$

(with $x = 1, 2, 3$).
After that, the products can be formed via a combination of the atomic species:

$$\mathrm{N + O \rightleftarrows NO} \tag{3.4}$$

and

$$\mathrm{N + N \rightleftarrows N_2} \tag{3.5}$$

To make the list of processes complete, the adsorption and desorption, as well as the diffusion of the various initial, intermediate species and products have to be considered:

$$\mathrm{Adsorbate} \rightleftarrows (*) + \mathrm{Adsorbate}\ \mathit{(g)} \tag{3.6}$$

$$\mathrm{Adsorbate} + (*) \rightleftarrows (*) + \mathrm{Adsorbate} \tag{3.7}$$

where $(*)$ means an empty site on the surface.
With this still very limited setup one can already start to evaluate the process rate constants for a kMC simulation to develop the TOF of the main products NO and N_2. Corresponding DFT calculations gave the following binding energies and energy barriers respectively, summarized in tables 3.2 and 3.3[16] (the energy diagrams for all energy barrier calculations concerning the reactions listed above as well as all the following (evaluated with the NEB as well as the drag method) are summarized in appendix D, for convergence tests and criteria see appendix A and B).
H_2O as well as N_2 have comparably low binding energies allowing for the efficient desorption within the temperature range of interest. In contrast NO, N, NH OH

---

[16] if not already displayed in 3.1

Adsorbate	E_{Bind} [eV]
O (atomic ref.)	3.90
NH_2	2.48
NH	2.60
N (molecular/ atomic ref.)	-0.94/ 3.72
OH	2.86
H_2O	1.14
NO	2.27
N_2	0.83

Table 3.2: Binding energies of the main surface species.

and NH_2 bind very strongly to the surface: The latter four ones are not stable in the gas phase and therefore their desorption from the surface will not be considered within the kMC simulations[17]. In contrast, NO is one of the main products within this reaction network – its desorption is highly desired. A comparably high binding energy for NO was reported in [14, 24]. In contrast, Hong *et al.* reported a smaller binding energy of this molecule. Furthermore the experiments in [1] imply an even lower binding energy. These discrepancies will be discussed in the following section.

The first dehydrogenation step of ammonia via oxygen (reaction 3.1 with $x = 3$) has a fairly low barrier, while the dehydrogenation via a hydroxyl group (reaction 3.2 with $x = 3$) does not exist: A stable minimum for the end-configuration of this process could not be found (this corresponds to the theoretical findings of Wang *et al.* [24]). The second dehydrogenation steps (reactions 3.1 and 3.2 with $x = 2$) show even lower activation barriers. And the third and last steps (reactions 3.1 and 3.2) even proceed without any barrier, while the corresponding back reactions do have barriers. Therefore it is assumed that the reaction network has the ability to quickly arrive at single nitrogen atoms on the surface that can provide the basis for the product formation processes (reactions 3.4 and 3.5). Their corresponding back reactions are very unlikely due to the high barriers.

---

[17] The binding energy of the nitrogen adsorbate is very high compared to the gas phase *atom* but very low compared to the gas phase *molecule* as it is also the case for oxygen. Therefore these two species do not desorb as atoms but as molecules. The binding energy of N_2 on the surface is higher than the one of O_2: 0.83 compared to 0.25 eV. Therefore the desorption of nitrogen is treated as a molecular desorption, following a combination reaction of two nitrogen atoms rather than an associative desorption process like it is the case for oxygen.

	E_{forward} [eV]	E_{back} [eV]
$NH_3 + O \rightleftarrows NH_2 + OH$	0.79	0.09
$NH_3 + OH \rightleftarrows NH_2 + H_2O$	FS not stable	0.00
$NH_2 + O \rightleftarrows NH + OH$	0.72	0.31
$NH_2 + OH \rightleftarrows NH + H_2O$	0.60	0.42
$NH + O \rightleftarrows NH + OH$	0.00	0.65
$NH + OH \rightleftarrows N + H_2O$	0.00	0.84
$N + O \rightleftarrows NO$	0.70	2.25
$N + N \rightleftarrows N_2$	0.82	3.50

Table 3.3: Energy barriers for the forward and back reactions 3.1, 3.2, 3.4, 3.5.

The decomposition of NH_3 into NH_2 and H as well as the further decomposition of NH_2 to NH and H (reactions 3.3 with $x = 2, 3$) are rather unlikely. This can already be concluded from the differences between the energies of the IS and FS (see table 3.4), as the corresponding reaction barriers have to be at least as high as this differences. The last dehydrogenation decomposition, NH to N + H (reaction 3.3 with $x = 1$), appears with a rather small energy difference. And indeed, the calculation of the MEP via NEB could show that there is no barrier, but the process just needs an activation energy as high as the energy difference between IS and FS to be performed. Therefore the latter process has to be included in the kMC simulations, while the first two decomposition processes can be ruled out.

	$\Delta E_{\text{(FS-IS)}}$ [eV]
$NH_3 \rightleftarrows NH_2 + H$	2.19
$NH_2 \rightleftarrows NH + H$	4.15
$NH \rightleftarrows N + H$	0.84

Table 3.4: Energy differences between IS and FS for the decomposition of various NH_x species. The energy differences between the IS and FS of the first two reactions are too high (with the barriers even higher), so that these reactions can be excluded.

Immanently important for the reaction network are the diffusion processes of the various adsorbates. The calculated diffusion barriers for diffusion processes from one *cus* site to another are listed in table 3.5[18].

---

[18] The diffusion barriers of NH_3 and O next to O and NH_3 and vice versa are simple estimates based on the calculations concerning the binding energy of these species with the corresponding

It turns out that several diffusion barriers are comparably high – especially the one

Adsorbate	E_{Diff} [eV]
NH_3	1.19
NH_3 (NH_3-rich)[18]	1.00
NH_3 (O-rich)[18]	1.50
N	1.65
O	1.55
O (O-rich)	1.19
O (NH_3-rich)	1.80
NO	1.87
NH	1.29
NH_2	2.52
OH	1.02
H_2O	0.75

Table 3.5: Diffusion barriers for the various surface adsorbates.

of NH_2 is remarkable. Yet also N and O exhibit high energy barriers for the diffusion process leading to very low process rate constants. Besides the constraints set by the row-type arrangement of the sites, as discussed above, these diffusion barriers are therefore a second crucial factor that could be a bottleneck for a proper mixture of the adsorbates.

KMC simulations which consider the reaction scheme presented above comprising 41 processes (3.1, 3.2, 3.3, 3.4 and 3.5, as well as diffusion, 3.7, desorption and adsorption processes, 3.6) lead to the TOFs displayed in diagram 3.6. The afore mentioned experiments [1] investigated the oxidation of ammonia on the $RuO_2(110)$ surface with TDS and HREELS experiments as well as steady state reaction kinetics experiments. The latter experiments were performed at temperatures of 500 and 530 K using UHV conditions. The resulting TOFs for 500 K will serve as the reference to control the validity of the theoretical ansatz evaluated in this work.

The kMC simulations were performed at a temperature of 500 K and at a constant NH_3 pressure of 1.0×10^{-10} atm as in experiment [1]. The oxygen pressure was varied analogous to the range in the UHV experiment [1] from 5.0×10^{-11} atm to 1.5×10^{-9} atm[19]. Within the kMC simulations the reactions that are mainly happening are the dehydrogenation reaction steps of NH_x via O and OH. The dehydro-

---

neighbors.

[19] if not stated otherwise.

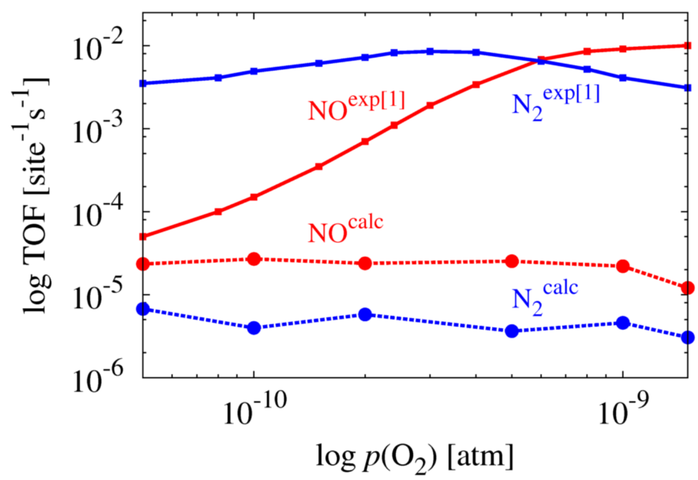

Figure 3.6: TOF vs. oxygen pressure from kMC simulations with a setup of 41 reactions at $T = 500\,\mathrm{K}$, $p(NH_3) = \mathrm{const} = 10^{-10}$ atm, compared to experiment: Straight lines represent the experimental [1], dashed lines the calculated results. Red lines are for NO, blue lines are for N_2

genation via decomposition (reaction 3.3) does occur also quite frequently, but is due to the low barrier always followed by immediate back reaction. Therefore neither hydrogen atoms nor their diffusion or combination to H_2 are detected within the simulation, despite the low barrier for the latter processes[20]. Also very frequent is the diffusion of the hydroxyl groups.

The TOF of nitrogen monoxide varies just slightly within the considered pressure range: It fluctuates around $2.5 \times 10^{-5}\,\mathrm{site}^{-1}\,\mathrm{s}^{-1}$. Only at a pressure of $p(O_2) = 1.5 \times 10^{-9}$ atm the TOF of NO starts to drop as the amount of oxygen species, namely O and OH, starts to displace the nitrogen species. With that the TOF of NO stays consequently below the experimental result. The same holds for the desorption rate of molecular nitrogen with even smaller values for its TOF: It fluctuates around $4 \times 10^{-6}\,\mathrm{site}^{-1}\,\mathrm{s}^{-1}$ and it drops to $1.2 \times 10^{-6}\,\mathrm{site}^{-1}\,\mathrm{s}^{-1}$ at $p(O_2) = 1.5 \times 10^{-9}$ atm.

---

[20] 0.1 eV for the diffusion process and 0.2 eV for the formation process.

The smooth decline is due to the increase of the oxygen pressure, which not only leads to more oxygen species on the surface but also leads to an overall higher surface occupancy (OH coverage). This in turn restricts the diffusion of N atoms. Water is with a TOF of $5-6\times10^{-5}\,\mathrm{site}^{-1}\,\mathrm{s}^{-1}$ the main desorption product throughout the whole pressure range.

NO dominates the surface occupancy over this whole pressure range: It represents with $\approx$ 40 % the main species. The accumulation of NO molecules on the surface was detected in the HREELS experiments of Wang *et al.*: At temperatures higher than 250 K weak peaks for the vibrational modes of nitrogen monoxide were observed, while the afore detected modes for NH_2 vanished. As the desorption of NO occurs only at a temperature as high as 500 K, the experimentalists assumed that the energy barrier for reaction 3.4 must be lower than the desorption barrier for NO, and therefore the NO release into the gas phase is expected to be desorption- rather than reaction-limited. This argumentation is in agreement with the formation energy and binding energy calculated for NO (see tables 3.2 and 3.3). However, no oxygen pressure dependency can be detected within the kMC simulations and the overall TOF is also remarkably lower than the measured one. This suggests that the binding energy of NO applied in the kMC simulations could be too high.

The high amount of rather immobile NO atoms on the surface has an influence on the N_2 desorption rate: The surface is passivated due to these molecules, and therefore the N atoms simply do not meet each other too often and thus can not overcome the comparably small barriers for N_2 formation and desorption. Though N atoms ($18-20\,\%$ coverage) were detected within the kMC simulations, the experimentalists could not find any hint for the existence of this species on the surface. For the TD spectra this is not surprising as the N atoms should bind so strongly to the surface that remarkably high temperatures would be needed to remove them from the surface (the maximum temperature in the TDS experiments was 700 K). And indeed the calculated binding energy for the single atom is remarkably high (see table 3.3). But also the HREELS did not show any signal for N. The experimentalists speculated in this case that the signal for N could be hidden due to overlap with other spectral features, but the absence of any signal could also be a hint that this species is indeed not present on the surface and that the kMC simulations miss an important process that would consume the N atoms to form another intermediate species or product.

Hydroxyl molecules as well as oxygen are both present on the surface in the kMC simulations. Yet while the average amount of the former is constant over the whole pressure range, the amount of the latter increases with increasing oxygen pressure, accompanied by a decrease of empty sites on the surface. Vibrational modes of oxygen atoms were clearly identified in the HREEL spectra. Their disappearance in the presence of ammonia molecules was detected at a temperature of 90 K. Only weak but existent a signal for the OH stretching mode also appeared around this temperature in the HREELS experiments. Both findings back up the reaction network simulated with kMC.

NH was also detected on the surface within the kMC simulations, covering around 10 % of the *cus* sites. Still neither the HREEL- nor the TD-spectra could proof its existence. The adsorbates, NH_3 and NH_2 share altogether only $1 - 2\,\%$ of the sites on the surface, implying that these species, once they are adsorbed/ formed, react immediately with their direct neighbors. The experimentalists indeed measured that ammonia either desorbs molecularly at a temperature of $\approx 460\,\mathrm{K}$ (as seen in the TD spectra) or reacts in the presence of oxygen as mentioned above. NH_2 could be clearly identified in the experiments via its rocking- and scissoring modes (in HREELS) though it could not be found on the surface (only in an almost negligible amount).

Desorption of the side product H_2O was detected at around 400 K in the TD spectra. And indeed the kMC simulations also show a vivid water formation and desorption: Once the molecule is formed it desorbs immediately, resulting in a TOF of $\approx 6.0 \times 10^{-5}\,\mathrm{site}^{-1}\,\mathrm{s}^{-1}$ being constantly higher than the production of NO and N_2. No other oxidation products like NO_2 or N_2O were observed in the experiments of Wang *et al.* [1]. In contrast, Perez-Ramirez *et al.* [14] reported N_2O as a desorption product within their experiments at ambient pressure. The average coverages of the species adsorbed on the surface for one representative oxygen pressure is summarized in tables 3.6 and 3.7 respectively.

$p(O_2)$ [atm]	TOF(NO) [site^{-1} s^{-1}]	TOF(N_2) [site^{-1} s^{-1}]	TOF(H_2O) [site^{-1} s^{-1}]
1.0×10^{-10}	2.7×10^{-6}	4.0×10^{-6}	1.0×10^{-5}

Table 3.6: KMC determined TOFs of the desorbing species NO, N_2 and H_2O at one representative oxygen pressure ($T = 500\,\mathrm{K}$, $p(NH_3) = 1.0 \times 10^{-10}$ atm).

Preliminary Summary

The TOF diagram for the kMC simulations comprising the 41 core reactions reveals that this basic setup can neither reproduce the high TOFs achieved in the experiment [1] nor grasp the main trend – an oxygen pressure dependency of the TOFs, featuring a crossover of the two TOF curves of NO and N_2 as also presented in [1]. The main problems at this stage seems to be the high binding energy of NO, that

Species	Coverage [%] at $p(O_2) = 1.0 \times 10^{-10}$ atm
NO	40
N	20
empty	20
OH	14
O	6
NH	6
others	2

Table 3.7: Average coverages for the main surface species at one representative pressure of oxygen as evaluated within kMC simulations comprising the basis reactions.

leads to a poisoning of the catalyst surface and the immobility of the N atoms, which therewith do not reach the vicinity of each other.
An earlier computational study [25] also determined a high diffusion barrier of the N atom, as well as a high binding energy for NO, drawing the same conclusion concerning the rate limiting steps for this reaction network. Their approach to improve the kMC simulations was to artificially modify these two barriers. The experimental results in [1] were reproduced quite nicely with this attempt. The legitimation for such an approach is nevertheless highly questionable as the calculated results no longer have a clear microscopic meaning but are instead only of an effective empirical nature.
The ansatz instead employed here is to refine the reaction network with a sensitivity guided analysis: To cure the identified problems, new concepts and reactions have to be applied to the kMC simulations. To investigate their very effect this will be done separately for each new idea. The successful ones that improve the results for the reaction network should then be combined. In the following chapters the ideas to overcome the – so far – two main obstacles, NO binding energy and immobile N, are presented and discussed.

3.4 Improvement steps

3.4.1 The high binding energy of NO

Nitrogen monoxide has by far the highest binding energies among those adsorbates in the system that are also stable in the gas phase. Therefore, desorption from the *cus* sites is rather sparse, though NO molecules *formation* via the atomic combination process 3.4 is very efficient. These two findings promote this species to be the main adsorbate on the surface under the considered gas phase conditions. A significantly lower binding energy of NO on $RuO_2(110)$ was reported by using the RPBE XC-functional: Perez-Ramirez *et al.* evaluated the binding energy of NO to be 1.78 eV (with the DFT code VASP [14]). With these two diverging results it is arguable if the PBE functional describes the binding of the NO molecule to the surface correctly. As discussed earlier (see chapter 2) the PBE XC functional is known to systematically the adsorbates' binding to the surface. The results from experiments [1] support this consideration: Estimating the binding energy of NO as inferred by its desorption temperature in the TDS experiments gave a value as low as 1.35 eV. This evaluation was done via the Redhead formula [114]. Binding energies of other adsorbates were evaluated in the same way (see [2]). The results of this crude approximation are listed in table 3.8 (the results not published in [2] were calculated using the desorption temperatures from [1] and the conditions/ prefactors according to [2]).

Adsorbate	T [K]	E_{Bind} [eV]
NO	500	1.35
NH_3 (O-rich conditions)	430	1.16
NH_3	420	1.13
N_2	420	1.13
H_2O	400	1.08

Table 3.8: Activation energies for the desorption for various species estimated with the Redhead formula as performed in [1, 2].

The calculated binding energies for NO as well as for NH_3 (which are not adjacent to an oxygen atom) are both higher than the values estimated via the Redhead formula. The binding energies for H_2O and NH_3 under oxygen-rich conditions are in contrast in rather good agreement. A special case is N_2: The calculated binding energy is lower than the one estimated with the Redhead formula (1.13 eV). In this case, the process that provides the basics for the formation of this molecule, namely the combination of two N atoms, is connected with a lower process rate constant than the desorption process and thus proceeds at a higher temperature. Only after these processes happen a N_2 molecule, that is able to desorb, is formed on the surface.

The different results for the binding energy imply that the binding energy of NO could actually be smaller than the one calculated in this work. It is therefore proceeded with a discussion of possible reasons for this discrepancy.

Lateral interactions

Destabilizing lateral interactions, like they occur between two adjacent ammonia molecules could also be found for NO molecules sitting next to an NH_2 molecule or an N atom: These two neighbors are able to lower the binding energy of NO significantly by 0.25 eV[21]. The kMC simulations comprising the basis reactions (see section before) reveal that the configuration of NO sitting next to an N atom occurs quite frequently, while NH_2 is almost not present on the surface – the former constellation could therefore have an impact on the TOFs, while the latter does most likely not change the results. KMC simulations were run with the two additional process rate constants and the reaction network comprises with that 43 processes. The corresponding TOF diagram is shown in 3.7.

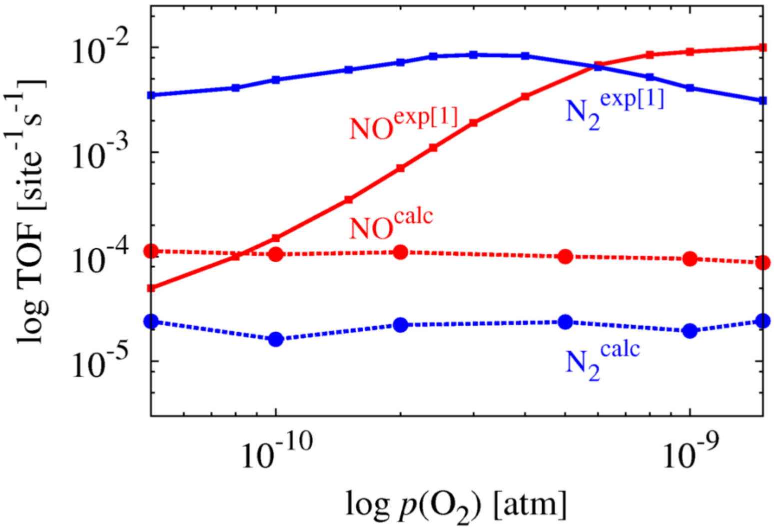

Figure 3.7: TOF vs. oxygen pressure for the 41 basis reactions including lateral interactions of NO with N and NH_2 respectively at $T = 500\,\mathrm{K}$, $p(NH_3) = \mathrm{const} = 10^{-10}$ atm (Straight lines represent the experimental [1], dashed lines the calculated results. Red lines are for NO, blue lines are for N_2).

---

[21] Lateral interaction calculations were also performed with the following neighbors next to the NO molecule: NH_3, NH, O, OH and H_2O. None of them could significantly lower the binding energy of NO.

Including the lateral interaction indeed increase the TOF of NO, and therewith also the TOF of N_2, as the NO molecules desorb more frequently. This allows for more movement and freedom for all adsorbates and therefore processes like the diffusion of N or NH can be executed more often. The surface exhibits with $\approx 39\,\%$ still a constantly high and rigid surface occupancy of NO. In contrast to the former simulations there are much more empty sites available than within the initial kMC simulations: About $30\,\%$ of the sites on the surface are unoccupied throughout the simulation. The average coverages for one representative pressure are summarized in table 3.9.

Species	Coverage [%] at $p(O_2) = 1.0 \times 10^{-10}$ atm
NO	39
N	6
empty	30
OH	9
O	9
NH	6
others	1

Table 3.9: Average coverages for the main surface species at one representative pressure of oxygen as evaluated within kMC simulations comprising the basis reactions as well as lateral interactions.

The TOF of NO steps up to $\approx 1 \times 10^{-4}\,\text{site}^{-1}\,\text{s}^{-1}$, reaching at least the region of the experimental TOF of NO at low oxygen pressure. Still the TOF of N_2 is with $\approx 2 \times 10^{-5}\,\text{site}^{-1}\,\text{s}^{-1}$ constantly one order of magnitude below the TOF of NO and far below the experiments' result. Both TOFs furthermore follow the same trend as before: Like in the simulations with 'just' the basis reactions they do not show a real oxygen pressure dependence – the TOFs just slightly drop with higher pressures as the oxygen species O and OH again require more sites on the surface. The TOF of the third product, water, is with $\approx 2 \times 10^{-4}\,\text{site}^{-1}\,\text{s}^{-1}$ twice as high as the TOF of NO. The resulting TOFs for one representative oxygen pressure are listed in table 3.10.

Zero point energy (ZPE) correction

The ZPE of the vibrational modes, which is needed to correct the zero-Kelvin state that is computed within the DFT calculations, sums up to 0.2 eV for the NO molecule

$p(O_2)$ [atm]	TOF(NO) [site^{-1} s^{-1}]	TOF(N_2) [site^{-1} s^{-1}]	TOF(H_2O) [site^{-1} s^{-1}]
1.0×10^{-10}	1.0×10^{-4}	2.0×10^{-5}	2.5×10^{-4}

Table 3.10: TOFs of the desorbing species NO, N_2 and H_2O from kMC simulations comprising lateral interactions between NO and NH_2 and N respectively at an oxygen pressure of 1.0×10^{-10} atm.

on the $RuO_2(110)$ surface and should therefore have an effect similar to the inclusion of the lateral interactions as it was done in the preceding section. As this correction is furthermore independent of the environment of the adsorbate the effect is expected to be even more pronounced. Corresponding kMC simulations including a ZPE-corrected NO binding energy revealed that this is indeed the case – the TOFs are not only higher than within the simulations with only the basis reactions, but even exceed the TOFs achieved in the kMC simulations that include the lateral interactions: The TOF for NO is with $\approx 5 \times 10^{-4}$ site^{-1} s^{-1} five times higher compared to the simulations comprising lateral interactions of NO. The TOF of N_2 is with $\approx 1.5 \times 10^{-4}$ site^{-1} s^{-1} even increased by one order of magnitude. The TOF of H_2O remains with 1.0×10^{-3} site^{-1} s^{-1} the main product.

The average coverage for one representative pressure (as summarized in table 3.11) reveals that the picture of the overall coverage changed: While the coverage with N atoms ($\approx 20\,\%$) was quite high within the very first simulations and dropped to only 6 % including lateral interactions, it reaches a preliminary maximum of 25 % when considering the ZPE correction for NO.

An oxygen dependence of the NO desorption could – like before – not be observed, but the TOF of NO is now clearly within the regime of the TOF achieved in the experiments.The TOFs for one representative oxygen pressure are listed in table 3.12.

It has to be admitted that in principle the ZPE has to be evaluated and the corresponding binding energy has to be corrected not only for one but all adsorbates on the surface. However, for single-atom adsorbates like N or O it is expected that the ZPE is lower than the ZPE of NO as the vibration of only one atom can account for a decrease of the binding energy. Furthermore oxygen atoms desorb frequently – even without the ZPE correction. For atomic nitrogen it is the other way around: It has such a high desorption barrier that the ZPE correction would not bring the corresponding process rate constant into the vicinity of a reasonable height so that desorption could be expected (A binding energy of 3.5 eV as it was calculated for the N atom causes a process rate constant of the order of $10^{-18} s^{-1}$. Lowering the binding energy by 0.2 eV would only change it by two orders of magnitude.).

In contrast hydrogen containing species like NH_x and H_xO are expected to have remarkably higher ZPEs than the NO molecule due to the higher number of degrees of freedom especially in the case of the NH_3 or H_2O species. Yet these species desorb (and re-adsorb) anyway quite frequently within the kMC simulations and therefore the correction of their binding energies concerning the ZPE is not expected to change the overall interplay of reactions on the catalyst surface significantly. The same holds for N_2: Within the kMC simulations it was observed that once it is formed, it desorbs always immediately. Lowering the energy barrier of desorption would have virtually no further influence.

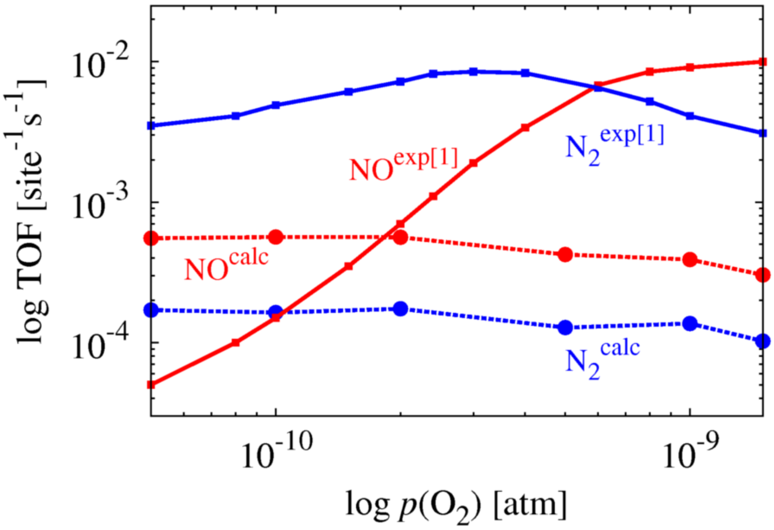

Figure 3.8: TOFs vs. oxygen pressure including the ZPE correction for NO at $T = 500\,K$, $p(NH_3) = const = 10^{-10}$ atm (Straight lines represent the experimental [1], dashed lines the calculated results. Red lines are for NO, blue lines are for N_2).

Intermediate summary

Refining just the binding energy of NO does not improve the overall picture of this reaction network, but just elevates the TOFs of the major products. It has to be furthermore admitted that the absolute value of the TOFs is not the major but rather a minor goal within this work: As the standard error in DFT energetics is likely around 0.2 eV, it can not be seen as a significant success to lower the binding energy

Species	Coverage [%] at $p(O_2) = 1.0 \times 10^{-10}$ atm
NO	33
N	25
empty	21
OH	15
O	15
others	1

Table 3.11: Average coverages for the main surface species at one representative pressure of oxygen as evaluated within kMC simulations comprising the basis reactions as well as ZPE correction for NO.

$p(O_2)$ [atm]	TOF(NO) [site^{-1} s^{-1}]	TOF(N_2) [site^{-1} s^{-1}]	TOF(H_2O) [site^{-1} s^{-1}]
1.0×10^{-10}	5.6×10^{-4}	1.7×10^{-4}	1.0×10^{-3}

Table 3.12: TOFs of the desorbing species NO, N_2 and H_2O comprising ZPE correction of NO at an oxygen pressure of 1.0×10^{-10} atm.

of a species by this amount.
The major goal within this work is rather to reproduce the *trend* of the TOFs and therefore to gain insights into the reaction network. Lowering the oxygen pressure will not introduce such an oxygen dependency to the TOF of NO, it would only take *longer* until the accumulation of NO molecules from which the desorption process would start, was reached. From this point on, the surface is poisoned with NO and the system is restricted in terms of the opportunities to proceed and therefore the desorption process, though the barrier is high, becomes more likely than before. As a consequence it is documented that the TOF of NO is indeed desorption- and not formation-limited.
To find a solution for this problem the binding energy of NO has to be either *significantly* lower than the values discussed above (possibly via a new process how the NO is formed and/ or desorbs off the surface) or an improved theoretical treatment acting on all processes within the reaction network has to be performed. The next improvement step will account for the latter.

Refinement of the overall picture: Spanning the whole range of semi-local XC-functionals

To capture the whole range of opportunities that GGA XC-functionals provide, the RPBE functional, suspected to deliver more accurate and typically lower binding energies than the PBE functional – at least for metals (see chapter 2 for details), is applied to the reaction network. With this approach not only a selected modification on one species is performed (like correcting just the NO molecule with the ZPE energy) but the whole reaction network will be treated.

Adsorbate	E_{Bind} [eV]
NH_3	1.21
NH_3 (O-rich conditions)	1.47
O (molecular/ atomic ref.)	0.84/ 3.59
NH_2	2.27
NH	2.20
N (molecular/ atomic ref.)	-1.02/ 3.54
OH	2.54
H_2O	0.83
NO	1.90

Table 3.13: Binding energies of the main species calculated with the RPBE XC-functional.

The RPBE XC-functional yields a binding energy of the NO molecule which is with 1.9 eV significantly lower than the one achieved with the PBE XC- functional. Similarly, the calculated binding energies of all species also decrease as compiled in table 3.13.

With the new binding energies the stability ranges of the different phases change and therefore a new *ab initio* phase diagram has to be constructed (displayed in diagram 3.9). The lower binding energies for all surface species evaluated with the RPBE functional lead to a shift of the phase regions: The phase, in which both ammonia and oxygen are adsorbed on the surface now correspond to higher pressures of ammonia and oxygen, compared to its PBE counterpart, leaving more space for the less occupied phases within the UHV pressure range of interest. First kMC simulations with this setup – accounting solely for the adsorption, desorption and diffusion processes of ammonia and oxygen – could show that the surface is indeed empty by around three-fourths under UHV conditions. When varying the pressure of ammonia and oxygen respectively (moving horizontally and vertically respectively within the

phase diagram), the tendencies are analogue to the kMC simulation with binding energies from PBE. A comparison of the two *ab initio* phase diagrams, 3.3 and 3.9 and the corresponding kMC results reveal that the two different XC-functionals yield two different regimes of occupancy: While the RPBE functional produces an almost empty surface under UHV conditions, the PBE functional produces a semi-occupied surface within the same pressure range. Both functionals have in common, that under ambient pressure the fully occupied surface is the most stable phase. As a consequence this setup allows to test the reaction network within these three very different regimes as the occupancy could become important if it comes to competing reactions that require empty sites.
The energy barriers for the various reactions change as well when treating the reaction

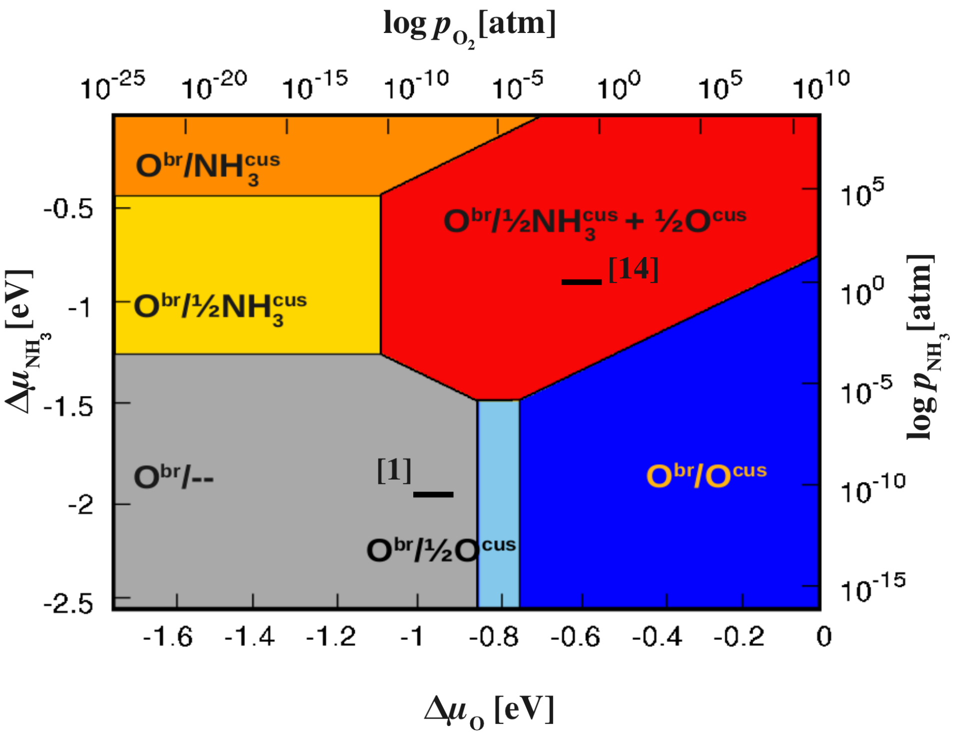

Figure 3.9: RPBE phase diagram of the $RuO_2(110)$ surface accounting for coverages of ammonia and oxygen at $T = 500\,K$: The black lines indicate the pressure range in which the experiments of Wang *et al.* [1] and Perez-Ramirez *et al.* [14] were performed.

pathways with the RPBE XC-functional. The energy barriers for the basis reactions 3.1, 3.2, 3.4 and 3.5, are listed in table 3.14. The results of the kMC simulations for this setup of 39 processes[22] with values from RPBE-DFT calculations are shown in the TOF diagram 3.10. The kMC simulations reveal that the TOF of NO shows an oxygen pressure dependence comparable to what was observed in [1]: At low oxygen pressure the TOF achieves only $4.5 \times 10^{-7}\,\text{site}^{-1}\,\text{s}^{-1}$, but at high oxygen pressure it increases by more than one order of magnitude to $4.2 \times 10^{-6}\,\text{site}^{-1}\,\text{s}^{-1}$. This is attended by a pronounced increase of hydroxyl molecules on the surface: While in the low-pressure regime only 14 % of the sites are occupied with OH, leaving the main part of 84 % empty, the surface exhibits a coverage of OH of 76 % within the high-pressure regime. Oxygen atoms cover the remaining 2 % of the sites and NH_x species are not stable at all on the surface. The evolution of the coverage with increasing oxygen pressure is displayed in diagram 3.11. Increasing the oxygen pressure up to a value of 1.5×10^{-5} atm leads to an even higher coverage of OH groups (no corresponding experimental results exist for this pressure) and the TOF of NO drops again, after passing the maximum of $3.7 \times 10^{-4}\,\text{site}^{-1}\,\text{s}^{-1}$ at 1.5×10^{-6} atm. Due to its low binding energy no accumulation of NO was observed.

							E_{forward} [eV]	E_{back} [eV]
NH_3	+	O	$\rightleftarrows$	NH_2	+	OH	0.84	0.00
NH_3	+	OH	$\rightleftarrows$	NH_2	+	H_2O	FS not stable	0.00
NH_2	+	O	$\rightleftarrows$	NH	+	OH	0.68	0.27
NH_2	+	OH	$\rightleftarrows$	NH	+	H_2O	0.31	0.00
NH	+	O	$\rightleftarrows$	NH	+	OH	0.00	0.77
NH	+	OH	$\rightleftarrows$	N	+	H_2O	0.00	0.70
N	+	O	$\rightleftarrows$	NO			0.79	2.24
N	+	N	$\rightleftarrows$	N_2			0.85	3.47

Table 3.14: Reaction barriers for the basis reactions calculated with RPBE.

What is gained for the TOF of NO is lost for the TOF of N_2: The formation and with that the desorption of this product stopped completely, due to the unavailability of NH_x species on the surface. The TOF of the H_2O molecule follows the trend of NO, but is always a little higher. The TOFs for two chosen oxygen pressures are summarized in table 3.15.

---

[22] The barrier for the decomposition process of NH to N an H was not considered as this process did not play any role in the afore performed kMC simulations.

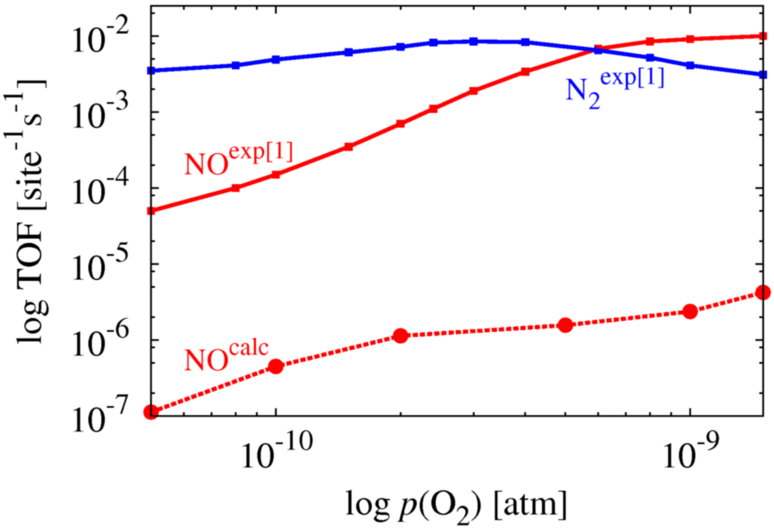

Figure 3.10: TOFs vs. oxygen pressure from kMC simulations with the 39 basis reactions treated with the RPBE XC-functional at $T = 500\,K$, $p(NH_3) = const = 10^{-10}$ atm (Straight lines represent again the experimental [1], dashed lines the calculated results. Red lines represent NO, blue lines N_2). Note that the calculated N_2 TOF is essentially zero, that is why no corresponding line is shown in the graph.

$p(O_2)$ [atm]	TOF(NO) [site^{-1} s^{-1}]	TOF(N_2) [site^{-1} s^{-1}]	TOF(H_2O) [site^{-1} s^{-1}]
1.0×10^{-10}	4.5×10^{-7}	0	1.6×10^{-7}
1.5×10^{-9}	4.2×10^{-6}	0	2.5×10^{-6}

Table 3.15: TOFs of the desorbing species NO, N_2 and H_2O at two different oxygen pressures representing two different coverages on the surface.

Summary

The variation of the binding energy of the NO molecule within the scope of the opportunities of DFT leads so far to an improvement of the TOF of this species: Within the PBE-framework, a TOF within the same order of magnitude as discovered in experiment is achieved, while the RPBE-framework provides the oxygen-dependency of

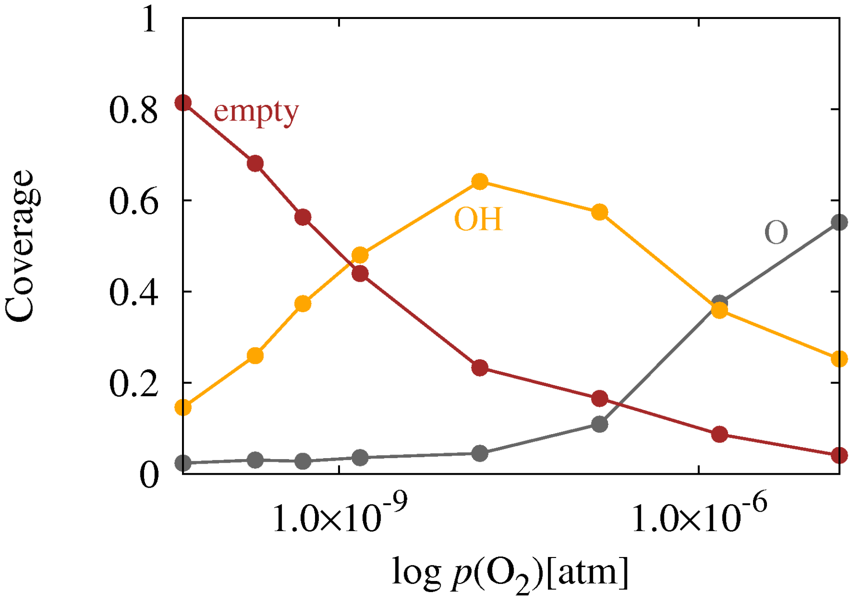

Figure 3.11: Coverage of the main surface species as obtained within kMC simulations with the basis reactions treated with the RPBE XC-functional at $T = 500\,\mathrm{K}$, $p(NH_3) = \mathrm{const} = 1.0 \times 10^{-10}$ atm.

the TOF of NO. The TOF of N_2 remains a major obstacle as its TOF is constantly below the experimental result and never higher than the TOF of NO. These two important characteristics of the experimental measurements are to be reproduced in the following.

3.4.2 The immobile nitrogen atom

The very high diffusion barriers of several species as well as the arrangement of the sites, namely in *cus* rows inhibit a proper mixing of the adsorbates. Focusing on the nitrogen atom, this species is not very mobile, and therefore the N atoms simply do not meet very often and therefore can not overcome the comparably low reaction barriers of N_2-formation and -desorption. The formation of O_2 this is not a problem, since O atoms, though they have a similar diffusion barrier, can desorb and re-adsorb, but do not necessarily have to flow along the *cus* rows to meet each other. And indeed the O_2 desorption was in all simulations very frequent. To promote the desorption of N_2 molecules, the N atom has to be more mobile. Alternatively, an additional process to form N_2 could also be a step forward to enhance the TOF of this product molecule.

Diffusion of NH_x species

Not yet included in the simulations is the ability of the hydrogen atoms to diffuse along NH_x and OH_x species. These diffusion processes[23] are expected to have barriers that are remarkably smaller than the diffusion barriers of the bare O or N atoms because hydrogen atoms are comparably small and the distance they have to cover from one NH_x- or OH_x species is smaller than the distance between two *cus* sites. Furthermore, the start and end geometries are at least in the case of NH_x as IS and NH_{x-1} as FS and OH_x as IS and OH_{x-1} as FS respectively, (with $x \neq 1$) very similar in energy. With this hydrogen diffusion along NH_x or OH_x it might not be necessary that bare N or O atoms have to diffuse along the *cus* rows on the $RuO_2(110)$ surface to find each other to combine to the products, but the job is done via the hydrogen atoms diffusing around and away, leaving bare O or N atoms next to each other. The initial kMC simulations showed that the amount of NH_x species on the surface is very low. But what if these species only reacted that fast with adjacent oxygen atoms because they simply do not have another choice? An NH_2 molecule, for example, could be more stable on the surface if the hydrogen atom is exchanged between the NH_2 and another N-containing species, rather than being abstracted by an O or OH, which leads most likely to H_2O and with that to the evacuation of the hydrogen atoms from the surface. To test this, the movements of hydrogen atoms along NH_x were included as well as their movement along OH_x species, though the latter could neutralize the effect of the former. In this respect, adding these additional processes to the kMC list is not too promising – at least in terms of the mobility of the N atom and with that in terms of the final TOF of N_2 – but these processes are definitely a part of the reaction network and although they might not solve the above mentioned problem they may provide their share to the overall activity on the catalyst surface. Furthermore these reactions are relatively simple – only one or two atoms move. To keep the effort marginal, the barriers for these processes are just estimated by the drag method. For such elementary reactions this simple approach should deliver reliable estimates for the barriers. All possible diffusion processes of H along NH_x or OH_x with their corresponding barriers are listed in table 3.16.

The barriers for the hydrogen diffusion processes are as expected in general very small. Only if it comes to the situation that a nitrogen atom should be converted

---

[23] Strictly speaking, reactions 3.1 and 3.2 are in that sense also diffusion processes.

							$\Delta E_{\text{TS-IS}}$ [eV]	$\Delta E_{\text{TS-FS}}$ [eV]
NH_3	+	NH_2	$\rightleftarrows$	NH_2	+	NH_3	0.07	=
NH_3	+	NH	$\rightleftarrows$	NH_2	+	NH_2	0.00	0.23
NH_3	+	N	$\rightleftarrows$	NH_2	+	NH	FS not stable	0.00
NH_2	+	NH	$\rightleftarrows$	NH	+	NH_2	0.13	=
NH_2	+	N	$\rightleftarrows$	NH	+	NH	1.18	0.00
NH	+	N	$\rightleftarrows$	N	+	NH	0.18	=
OH	+	O	$\rightleftarrows$	O	+	OH	0.09	=
OH	+	OH	$\rightleftarrows$	O	+	H_2O	0.19	0.00
H_2O	+	OH	$\rightleftarrows$	OH	+	H_2O	0.10	=

Table 3.16: Diffusion barriers for the hydrogen atoms along NH_x and OH_x species.

into a hydrogen species the barrier is significantly higher due to the loss of the strong binding energy of N bond to the surface. Therefore it can be assumed that the diffusion of the hydrogen atoms along N_x as well as O_x is very fast. The conditions for an easier conjunction of two N atoms are thus given.

Having a closer look on the hydrogen atoms, the hydrogen *orientation* also has to be discussed when evaluating the most stable geometries of the affected adsorbates: These are NH_3, NH_2, NH, OH and H_2O. The hydroxyl group and NH both have the same most stable orientation on the surface: The hydrogen atom points along the line of the *cus* row. The NH molecule encloses an angle of 122.8° with the surface, while the OH exhibits a slightly smaller angle of 113.5° [24] (see also picture 3.12). An orientation of the hydrogen atom towards the O_{br} is in both cases less stable, even though only by ≈ 0.1 eV: The oxygen sitting on the bridge row seems to be too far away to stabilize the orientation via hydrogen bonds with the adsorbates. Having this finding in mind, one could come up with the same concept for H_2O and NH_2: Both molecules could be oriented along or orthogonal to the *cus* rows of the surface of the $RuO_2(110)$ facet. For NH_2 this is indeed the case: Its hydrogen atoms point in perpendicular directions along the *cus* row with the N atom located above the underlying Ru-atom with a H-N-H angle of 113.8° (see picture 3.13). This orientation is by 0.21 eV more stable than the to-O_{br} position.

---

[24] This reflect the behavior of these species in the context of organic molecules: OH groups in alcohols exhibit with an R-O-H angle of 109° also a smaller angle than R-N-H in an imine (120°) [115]. The different angles come about the higher electron density around the oxygen atom: It has two free electron pairs while nitrogen coordinates only one electron pair around itself.

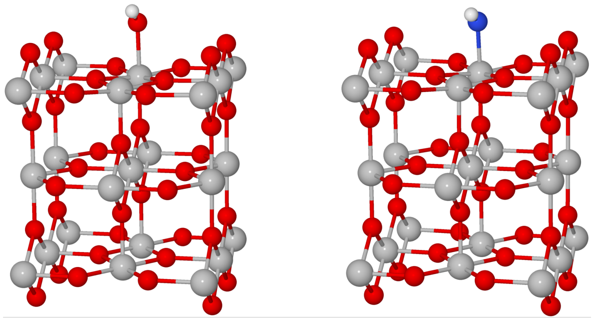

Figure 3.12: NH (left) and OH (right) adsorbed on the $RuO_2(110)$ surface (both in side view). The hydrogen atoms point in both cases along the *cus* rows. The angle between Ru-O-H is with 113.5° slightly smaller that the angle that is enclosed between Ru-N-H (122.8°) (Oxygen: red, ruthenium: grey, nitrogen: blue, hydrogen: white).

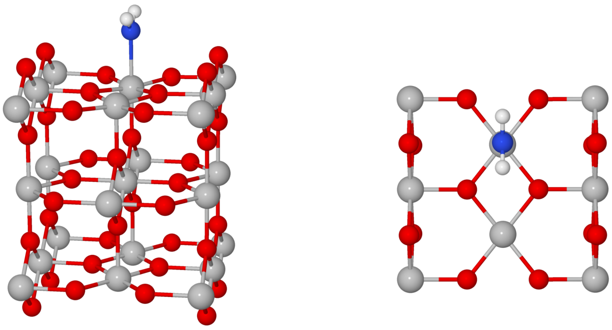

Figure 3.13: NH_2 adsorbed on the $RuO_2(110)$ surface (side and top view). The hydrogen atoms point along the *cus* rows at the surface (Oxygen: red, ruthenium: grey, nitrogen: blue, hydrogen: white).

For the water molecule the situation is different: It adsorbs asymmetrically on the surface, with one hydrogen atom pointing along the *cus* row and one towards the

O_{br} with a H-O-H angle of 100°[25] (see picture 3.14). The two symmetric orientations along the *cus* row and towards the bridging oxygen atoms are less stable by 0.15 eV and 0.21 eV respectively.

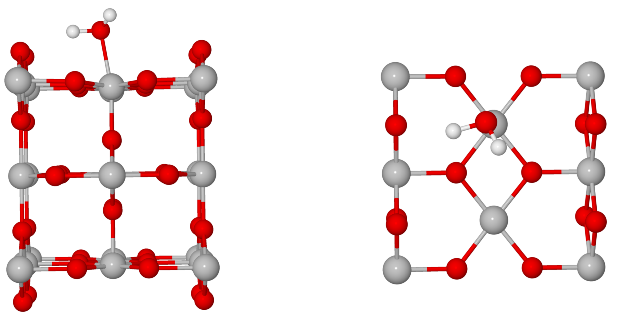

Figure 3.14: H_2O adsorbed at the $RuO_2(110)$ surface (side and top view): The molecule does adsorb asymmetrically (Oxygen: red, ruthenium: grey, hydrogen: white).

The most stable structure has not necessarily the lowest diffusion barrier – it would actually make more sense, if a less stable structure that is not bound too strongly to the surface would diffuse easier than the most stable configuration. This is indeed the case for several of the above mentioned species: The diffusion barriers for the different orientations of the hydrogen(s) for the nitrogen- and oxygen-containing species are listed in table 3.17.

The difference between the diffusion barrier of NH_2 pointing its hydrogen atoms along the *cus* rows and the NH_2 pointing its hydrogen atoms to the O_{br} is remarkably high. As speculated above, the lower diffusion barrier does not correspond to the more stable structure, but to the less stable one. It was found that the rotation around the Ru-N axis only has a small barrier of 0.1 eV. The same holds for the rotation of the H atoms of OH or NH from one to another in-*row* position or towards a to-O_{br} position. Therefore it is expected that the NH_x- or OH_x-species are able to rotate into the geometry which is most suitable for the diffusion, accomplish this process and rotate back to the geometry that results in the highest binding energy. Advancing the lower

---

[25] Interestingly the H_2O molecules is even tilt towards one to-O_{br} row by 10.2°. The two H-O-Ru angles are 96.3° and 114.45°.

	$E_{\text{Diff, }cus\text{ row}}$ [eV]	$E_{\text{Diff, to-O}_{br}}$ [eV]	$E_{\text{Diff, asymmetric}}$ [eV]
NH	1.29	0.84	—
NH_2	2.52	0.57	—
OH	1.02	0.92	—
H_2O	0.60	0.54	0.75

Table 3.17: Diffusion barriers for the different orientations of the hydrogen containing species.

diffusion barriers by about the value of the corresponding rotation barriers should then yield the reasonable diffusion barriers for the hydrogen-containing species. This naturally only makes sense if the energy gain for the diffusion barrier is higher than the energy loss caused by the rotation. Therewith the diffusion barrier for NH_2 can be lowered significantly as the rotational barrier from the in-*cus*-row orientation to the to-O_{br} orientation is only 0.18 eV but the difference between the two diffusion barriers is almost as high as 2 eV.
The water molecule with the hydrogen atoms oriented towards the O_{br} atoms diffuses with the lowest barrier. The diffusion for H_2O oriented along the *cus* rows is only slightly higher. The highest diffusion barrier is connected with the most stable configuration, the asymmetrically adsorbed water molecule. A rotation from the most stable orientation of the hydrogen atoms to a less stable could therefore help to reduce the diffusion barrier. However, the differences between the diffusion barriers for the unfavorable configurations and the diffusion barrier of the favored configuration are both so small that they can easily be reached or even exceeded by the barriers for the rotations that have to be accomplished to flip between the various orientations. Furthermore, the TS of the diffusion of H_2O has for both unfavored geometries a higher energy than the TS of the diffusion process via the favored orientation of the water molecule (see energy diagram in appendix D). Therefore a decrease of the diffusion barrier would not result in a lower energy barrier for this process and therewith it is not corrected.
The diffusion barrier of the hydroxyl species does also not have to be adjusted as the TS for both orientations of OH was evaluated to be the same: The hydrogen atom points between two O_{br} atoms (see also appendix D for details). The difference between the diffusion barriers of the two possible NH orientations is with 0.45 eV high enough to be possibly changed: As the rotation from in-*cus*-row orientation to the to-O_{br}-orientations consumes only 0.1 eV the barrier is adjusted appropriately in the kMC simulations (see also diagram in appendix D for details). The barriers for the evaluated rotation processes are listed in table 3.18. The most stable orientation of a

Rotation from	to	ΔE_{Rot} [eV]
$NH_{2,\text{in-row}}$	$NH_{2,\text{to-O}_{br}}$	0.18
$NH_{\text{in-row}}$	$NH_{\text{to-O}_{br}}$	0.10

Table 3.18: Rotation barriers for the movement of hydrogen atoms around NH_x- or OH_x-species.

molecule can change with various neighbors, executing lateral interactions with the molecule of interest. And for some reactions it might be helpful, if a molecule was in another than the most stable orientation. The water molecule for example is formed via a TS, in which the hydrogen atoms of H_2O are oriented along the *cus* row from which the diffusion would be easier than from the end geometry. On the other hand bulky neighbors like ammonia could enforce other most stable geometries via lateral interaction. Accounting for all different cases and positions of all species within the above mentioned reactions would go beyond the scope of this work and the impact on the TOFs is somewhat questionable since the difference in the energy barriers would be rather small and the reactions that would be affected already do *occur* efficiently in the reaction network simulation of kMC. Therefore only the diffusion barriers for NH_2 and NH are adjusted, while the diffusion barriers for water and OH remain unchanged as well as the barriers for reactions in which water is formed.

Including these hydrogen diffusion processes and adjusting the process rate constants respectively yield no significant differences of the TOFs of the products compared to the very first kMC simulation approach comprising just the basis reactions (see diagram 3.15): The TOF of NO is still of the order of $10^{-5}\,\mathrm{site}^{-1}\,\mathrm{s}^{-1}$, and the TOF of N_2 stays with $10^{-6}\,\mathrm{site}^{-1}\,\mathrm{s}^{-1}$ still below the former (even though a bit less than in the very first approach). The TOF of water exceeds again both of these TOFs, ranging with $5 \times 10^{-5}\,\mathrm{site}^{-1}\,\mathrm{s}^{-1}$ slightly above the TOF of NO. Moreover the TOFs do not show a sensitivity towards the oxygen pressure, but rather show the same accumulation of NO molecules on the surface, which leads to the already described passivation of the surface.

Notwithstanding a big difference can be seen in the surface occupancy. Besides NO as the main species and O and OH, as well as empty sites, a new stable adsorbate can be observed on the surface: NH_2 represents now with $\approx 20\,\%$ one of the major species within the simulations with this setup of reactions, while NH as a stable adsorbate disappears. The surface population accordingly corresponds to the surface occupancy as detected in the HREELS and TDS experiments as discussed in the beginning of this chapter. The coverages of the main species for one representative pressure are listed in table 3.19.

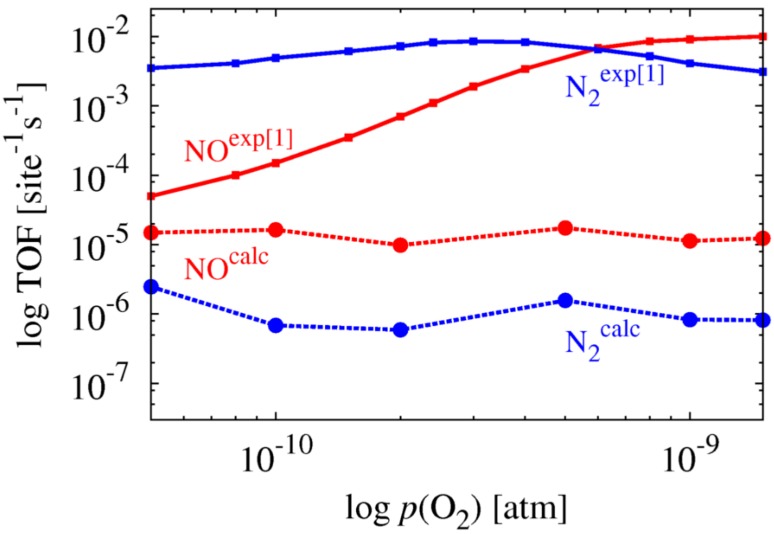

Figure 3.15: TOFs vs. oxygen pressure for the initially defined 41 basis reactions (evaluated with PBE) and hydrogen diffusion at $T = 500\,\mathrm{K}$, $p(\mathrm{NH_3}) = \mathrm{const} = 10^{-10}$ atm (Straight lines represent again the experimental [1], dashed lines the calculated results. Red lines represent NO, blue lines N_2).

Species	Coverage [%] at $p(\mathrm{O_2}) = 1.0 \times 10^{-10}$ atm
NO	60
NH_2	20
empty	16
O	3
others	1

Table 3.19: Average coverages for the main surface species at one representative pressure of oxygen as evaluated within kMC simulations comprising the basis reactions as well as hydrogen diffusion reactions.

An alternative pathway to produce N_2

From the first kMC simulations it could be seen that a nitrogen atom sits very often next to an NO molecule. This configuration gives rise to a new reaction pathway, NO + N, that leads to a new surface species, namely N_2O, which itself can then decompose into N_2 and O (see reactions 3.8 and 3.9).

$$\mathrm{NO} + \mathrm{N} \rightleftarrows \mathrm{N_2O} \tag{3.8}$$

$$\mathrm{N_2O} \rightleftarrows \mathrm{N_2} + \mathrm{O} \tag{3.9}$$

In this reaction only one nitrogen atom is involved and the formation process of N_2 depends no longer on a diffusion process. Furthermore this reaction can help to control the amount of NO molecules by abolishing NO so that the passivation of the surface can be avoided. Including these reactions requires to add as well the diffusion and desorption of the new surface species N_2O to the process list. In total this list then contains 45 reactions. The calculated energetic parameters for these additional reactions are listed in tables 3.20 and 3.21 respectively[26].

			E_{forward} [eV]	E_{back} [eV]
NO + N	$\rightleftarrows$	N_2O	1.24	1.43
N_2O	$\rightleftarrows$	N_2 + O	0.33	1.39

Table 3.20: Energy barriers for the formation and decomposition of N_2O.

$E_{\text{Bind}}(N_2O)$	0.63 eV
$E_{\text{Diff}}(N_2O)$	0.50 eV

Table 3.21: Binding energy and diffusion barrier of N_2O.

The amount of desorbing N_2 increases slightly up to $1.5 \times 10^{-5}\,\text{sites}^{-1}\,\text{s}^{-1}$, attaining the vicinity of the TOF of NO that is with $2.5 \times 10^{-5}\,\text{sites}^{-1}\,\text{s}^{-1}$ almost as high as yielded in the very first attempt. Water remains with a TOF of $4.5 \times 10^{-4}\,\text{sites}^{-1}\,\text{s}^{-1}$ within the same range as in the first kMC simulations.

The most important innovation is the frequent desorption of N_2O. This species has such a low binding energy that its desorption follows immediately after the formation via reaction 3.8. The N_2O molecules therewith do not have the chance to decompose

---

[26] Diffusion barrier evaluated with the drag method.

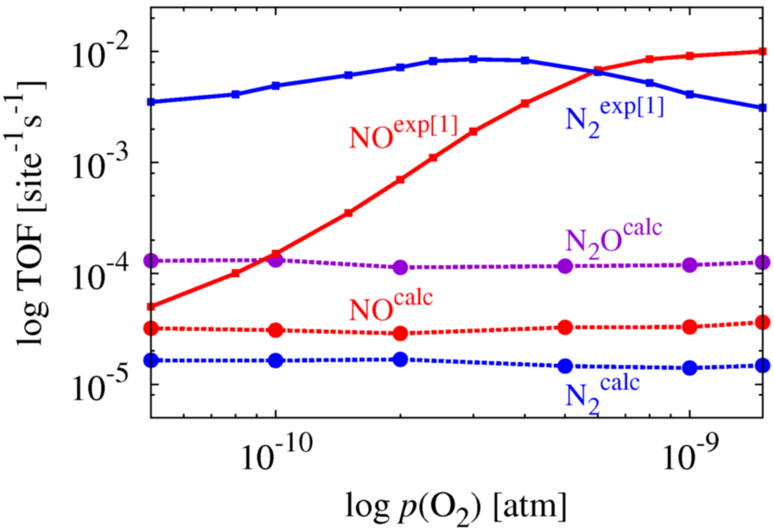

Figure 3.16: TOF vs. oxygen pressure including the basis reactions as well as reactions 3.8 and 3.9 that proceed via N_2O at $T = 500\,K$, $p(NH_3) = const = 10^{-10}$ atm. The new reactions introduce a new species that desorbs from the surface: N_2O is the main product (Straight lines represent again the experimental [1], dashed lines the calculated results. The red lines represent NO, blue lines N_2, the violet line N_2O).

into N_2 and O, though this reaction has a very low reaction barrier. This promotes N_2O to be the main desorption product with a TOF of $6.0 \times 10^{-5}\,sites^{-1}\,s^{-1}$. The afore mentioned increase of the TOF of N_2 is therefore not directly owed to the new reaction pathway. Yet the overall higher desorption rate generates more empty sites on the surface and therewith diffusion processes are in general performed more often, promoting also the N diffusion and with that the N_2 production.

An oxygen pressure dependence could still not be identified for any desorbing species. The coverage of the various species on the surface within this reaction network is distributed as follows: NO still constitutes with 35 % the main surface species, but empty sites are present almost in the same amount (30 %). OH and N occupy with 15 % and 13 % respectively less sites. NH and finally O are least present on the surface. The coverages for one representative pressure are summarized in table 3.22. Wang *et al.* [1] did not detect any N_2O desorption in their UHV experiments, while the ambient-pressure experiments of Perez-Ramirez *et al.* [14] clearly identified this

Species	Coverage [%] at $p(O_2) = 1.0 \times 10^{-10}$ atm
NO	35
N	3
empty	30
OH	15
O	5
NH	10
others	1

Table 3.22: Average coverages for the main surface species at one representative pressure of oxygen as evaluated within kMC simulations comprising the basis reactions as well as the formation and decomposition reaction of N_2O.

molecule as desorbing from the surface. Furthermore, the two experiments differ in another main result: Under ambient pressure N_2 is the main product for the whole pressure range and for all measured temperatures ($T = 573$, 673 and 773 K): It has a by far higher selectivity than NO. Under UHV conditions molecular nitrogen desorbs in contrast more often *only* at a very low oxygen pressure. At an oxygen pressure of $p(O_2) = 6 \times 10^{-10}$ atm the TOF of NO already starts to overthrow the TOF of N_2, reaching a selectivity of $\approx 80\,\%$ at 500 K and $\approx 100\,\%$ at 530 K. Perez-Ramirez *et al.* speculate that this difference between their ambient pressure experiment and the UHV experiment of Wang *et al.* could arise from the overall surface occupancy: At higher pressures the diffusion processes, which they also identified as having high process rate constants, do not necessarily have to be performed for a meeting of two N atoms or an N atom and an NO molecule. Therefore these formation processes (3.5 as well as 3.9) do occur more often. Under UHV conditions the overall surface occupancy might instead be too low for that. As discussed above the number of empty sites indeed differ severely for the two different pressure regimes (though the *ratios* of the two pressures of ammonia and oxygen are the same) (see phase diagrams 3.3 and 3.9). Furthermore the composition of the adsorbates on the surface could be different for the two different pressure regimes promoting either the production of NO or N_2. The same could hold for the formation and desorption process of N_2O.

To clarify not only the discrepancies between experiment and theory with respect to N_2O desorption under UHV, but also between the two experiments that investigate two different phases of the system, kMC simulations are also performed at ambient pressure. To mimic the setup of the experiments of Perez-Ramirez *et al.* the reaction network is treated with an oxygen pressure of $1 - 2 \times 10^{-2}$ atm and an ammonia pressure of $p(\mathrm{NH_3}) = 2 - 5 \times 10^{-3}$ atm as listed in table 3.23.

Ratio $p(\mathrm{O_2})/\,p(\mathrm{NH_3})$	TOF(NO) [site^{-1} s^{-1}]	TOF(N_2) [site^{-1} s^{-1}]	TOF(N_2O) [site^{-1} s^{-1}]
2:1	1.4×10^{-5}	1.9×10^{-5}	2.3×10^{-5}
5:1	9.9×10^{-6}	1.7×10^{-5}	2.0×10^{-5}
10:1	6.1×10^{-6}	2.3×10^{-6}	5.6×10^{-7}

Table 3.23: TOFs for the reaction network comprising the basis reactions as well as the formation, diffusion and desorption as well as decomposition of N_2O molecule at ambient pressures: $p(\mathrm{O_2}) = \mathrm{const} = 10^{-1}$ atm, $p(\mathrm{NH_3}) = 5 \times 10^{-2}$, 2×10^{-2}, 1×10^{-2} atm.

At these almost ambient pressures the TOF of molecular nitrogen at lower oxygen-ammonia-pressure ratios (2 : 1 and 5 : 1) is slightly higher than the TOF of NO. When the oxygen pressure is clearly dominating (ratio 10 : 1) the TOF of NO is superior. The TOF of N_2O constitutes the main product for the pressure ratios of 5 : 1 and 2 : 1. Its TOF drops severely for a ratio of 10 : 1 and this adsorbate is then the minor product due to a higher oxygen occupancy. In contrast Perez-Ramirez *et al.* [14] found N_2 to have a far higher TOF than the two other products. Furthermore, the TOF of N_2O was measured to be higher than the TOF of NO which should be by far the least desorbing molecule[27]. However, the experimental results were performed at a slightly higher temperature ($T = 575$ K). Still, the calculations do not reproduce any feature of the experimental findings. The coverage at these ambient pressures differs severely from the configuration under UHV conditions: The main species on the surface is no longer the NO molecule but rather NH, as well as NH_3 pushing the coverage of NO to half of the amount compared to the initial simulations. Furthermore far less empty sites are available. The coverage of the surface for one representative pressure is itemized in table 3.24.

Flat or upright N_2O molecule?

Analysis of the calculated reaction pathway of the conversion of NO + O to N_2O and further to N_2 + O reveals that both transitions go via a flat lying N_2O species that occupies two *cus* sites (see appendix D). The most stable N_2O orientation is in

---

[27] Selectivities for $T = 573$ K, $p(\mathrm{O_2})/p(\mathrm{NH_3}) = 5 : 1$: $N_2 = 80\,\%$, $\mathrm{NO} = 2\,\%$, $N_2O = 18\,\%$.

Species	Coverage [%] at $p(O_2) = 1.0 \times 10^{-1}$ atm $p(NH_3) = 2.0 \times 10^{-2}$ atm
NO	20
NH	22
NH_3	22
OH	5
O	10
others	5

Table 3.24: Average coverages for the main surface species at one representative pressure of oxygen as evaluated within kMC simulations comprising the basis reactions as well as the formation and decomposition of N_2O at ambient pressure.

contrast almost upright (see pictures 3.17 and 3.18 for details).

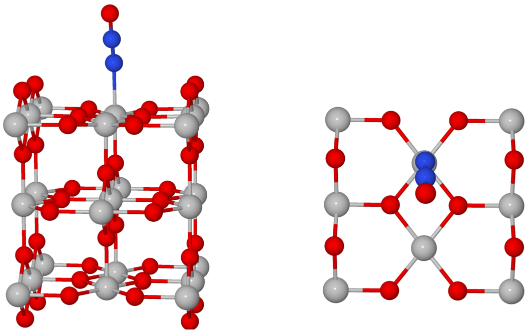

Figure 3.17: N_2O adsorbed on the $RuO_2(110)$ surface (side and top view) in its most stable orientation – almost perpendicular to the surface.

Therefore it can be possible that the end products N_2 and O in reaction 3.9 are not necessarily formed via the N_2O in its upright orientation, but proceed from an earlier stage of the reaction pathway of reaction 3.8, namely the flat lying N_2O:

$$NO + N \rightleftarrows N_2O_{\text{flat}} \rightleftarrows N_2 + O \tag{3.10}$$

DFT calculations show that the flat lying orientation of N_2O in which the molecule bridges two *cus* sites indeed represents a local minimum on the PES. However, this state is only stable if there are free empty sites adjacent. From this state N_2O can

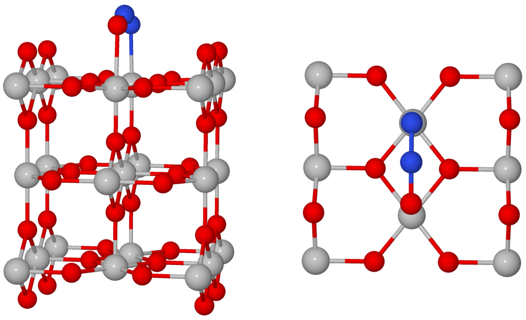

Figure 3.18: Flat N_2O adsorbed on the $RuO_2(110)$ surface (side and top view): This orientation occurs as a transient state on the reaction pathway from NO + N to the upright N_2O.

then decompose to N_2 and O, as described in 3.10 or it can swing to the upright position. Wang *et al.* [2] who also performed UHV experiment with NO on the $RuO_2(110)$ surface observed this flat lying orientation of N_2O as an intermediate during the formation of N_2 in their HREELS experiments. The barriers for the modified processes are listed in table 3.25.

			E_{forward} [eV]	E_{back} [eV]
NO + N	$\rightleftarrows$	N_2O_{flat}	1.11	1.11
N_2O_{flat}	$\rightleftarrows$	N_2 + O	0.00	1.21
N_2O_{flat}	$\rightleftarrows$	N_2O_{up}	0.22	0.32

Table 3.25: Energy barriers for the formation and decomposition of N_2O via its flat lying orientation.

The barrier for the transition of NO + N to the flat lying N_2O is slightly lower than the transition to the upright standing N_2O (reaction 3.8). The decomposition of the flat lying N_2O into N_2 and O proceeds then without any barrier, while the straightening of the molecule is connected with a small but existent barrier of 0.22 eV. This new reaction pathway has the potential to change the whole picture drawn by the kMC simulations that include the N_2O formation process: With this refined reaction pathway of N_2O formation and decomposition, the desorption of N_2O could no longer be favored over the decomposition to N_2 and atomic oxygen. Furthermore a coverage dependency is introduced with this new reaction channel: The flat lying N_2O is only stable at low coverages – at high coverages it will not be formed. This could explain the different findings of the two experiments ([1] = lower coverage, no N_2O desorption; [14] = high coverage, N_2O desorption). The resulting TOF diagram with the improved reaction network comprising the basis reactions as well as the reaction pathway via the flat lying N_2O is shown in diagram 3.19.

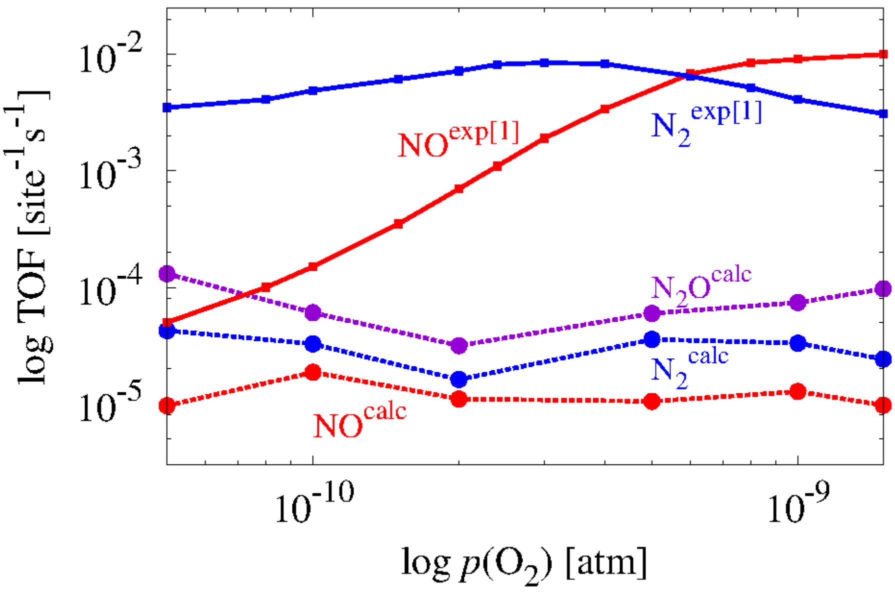

Figure 3.19: TOF vs. oxygen pressure for kMC simulations comprising the improved reaction pathway for N_2 formation via a flat lying N_2O at $T = 500\,K$, $p(NH_3) = const = 10^{-10}$ atm (Straight lines represent the experimental [1], dashed lines the calculated results. Red lines represent NO, blue lines N_2, violet line N_2O).

Within this extended reaction network the desorption of N_2 overcomes the one of NO: The TOF of N_2 increases slightly to $\approx 3 \times 10^{-5}$ sites^{-1} s^{-1}, while the TOF of NO drops to $\approx 1 \times 10^{-5}$ sites^{-1} s^{-1} compared to the simulations comprising solely the reaction pathway via the upright N_2O. The desorption of H_2O remains unchanged: It is still the main product. The TOF of N_2O does not change as well. Although the barrier is smaller, reaction 3.10 is performed less often than 3.8 – it seems as there are not enough empty sites for the former process. Most of the N_2O molecules are therewith still in their upright standing position and still desorb immediately after the formation process. Only a small fraction of the N_2O molecules on the surface are generated in their flat lying orientation. These N_2O molecules decay in any case into N_2 and atomic oxygen and higher therewith the desorption rate of N_2. The process of the flat lying N_2O moving into the upright standing position was never observed. As NO still requests the position as the main adsorbate on the surface, the TOFs remain constant within the whole pressure range, showing no sensitivity towards the change of the oxygen pressure. The coverage for the main species for one representative pressure is summarized in table 3.26.

Species	Coverage [%] at $p(O_2) = 1.0 \times 10^{-10}$ atm
NO	40
N	2
empty	30
OH	4
O	6
NH	16
others	2

Table 3.26: Average coverages for the main surface species at one representative pressure of oxygen as evaluated within kMC simulations comprising the basis reactions as well as the N_2O adsorbate in its flat lying configuration.

At *ambient* pressure the hierarchy of desorption of the three adsorbates of interest, N_2O, NO and N_2, change completely compared to the UHV simulations: NO is, after water, the main product, followed by N_2. The least desorbing product is N_2O. The TOFs for the main desorbing species at an oxygen pressure of 1×10^{-2} atm and an ammonia pressure of $p(NH_3) = 1 - 5 \times 10^{-3}$ atm are listed in table 3.27. The surface

Ratio $p(O_2)/\,p(NH_3)$	TOF(NO) [$\text{site}^{-1}\,\text{s}^{-1}$]	TOF(N_2) [$\text{site}^{-1}\,\text{s}^{-1}$]	TOF(N_2O) [$\text{site}^{-1}\,\text{s}^{-1}$]
2:1	9.3×10^{-6}	5.2×10^{-6}	7.0×10^{-6}
5:1	9.8×10^{-6}	4.6×10^{-6}	6.1×10^{-6}
10:1	1.3×10^{-5}	5.2×10^{-6}	6.9×10^{-6}

Table 3.27: TOFs for the reaction network comprising the basis reactions as well as the formation, diffusion, desorption and decomposition of the for both orientations of the N_2O molecule at ambient pressures: $p(O_2) = \text{const} = 10^{-1}$ atm, $p(NH_3) = 5{\times}10^{-2}$, 2×10^{-2}, 1×10^{-2} atm.

exhibits – as achieved within the preceding simulation (comprising only the N_2O formation pathway via the upright standing molecule, reaction 3.8) – no empty sites and the main adsorbates are still NH_3 and NH. However, the amount of O and OH is increased.

Furthermore, NO is, now for all pressure ratios, the main product, followed by N_2. N_2O is for all pressure ratios the least desorbing one. Unfortunately, the kMC simulations predict thus less N_2O desorption under ambient-pressure condition than under UHV conditions. This is contrary to the findings of the experiment: Under UHV no desorption of N_2O was detected at all while at ambient pressure N_2O desorption *was* observed. Furthermore the trend of the desorption rates of NO and N_2 could not be reproduced: In contrast to the kMC simulations the ambient-pressure experiment always measure distinctly more N_2 than NO.

3.4.3 Summary

The mobilization of the nitrogen atom via the inclusion of the diffusion processes of NH_x species, as well as the adjustment of the diffusion barriers of NH_2 and NH, do not improve the desorption rate of N_2 so far – the TOF even decreases slightly within this approach. The surface occupancy changes considerably though: While for the basis reaction network NO and N were the only nitrogen species that were present on the surface, NH_2 is introduced as one of the main adsorbates on the surface by considering the afore mentioned processes.

In contrast inclusion of the new surface adsorbate, the flat lying N_2O together with the associated processes of formation, decomposition, diffusion and desorption leads indeed to a higher TOF of N_2. The N_2O molecule shapes up as problematic: Its desorption is overall too high under UHV conditions, and even lower under ambient pressure – although the experiments reported the opposite behavior. However, the kMC simulations allow for the detailed insight into the surface configuration under these very different pressure regimes, revealing that not only the amount of empty sites is diverging but also the composition of the adsorbates changes.

The major goal – an oxygen dependency as well as a cross-over between the TOFs of NO and N_2 could still not be introduced with any of the variations. Hence, the combination of the promising ideas is the next step.

3.5 Combining the successful approaches

The individual approaches to adjust the TOFs of NO and N_2 within the reaction network of the ammonia oxidation on $RuO_2(110)$, as they were described in the preceding chapters, were by themselves not able to change the overall picture or introduce the main features of the TOF diagram measured in the experiments [1]. The combination of the promising approaches and by that the influence of them *on each other*, however, could lead to a new overall picture.

3.5.1 Combined RPBE approach

Among the so far tested attempts the RPBE XC-functional treatment of the basis reactions was the only one that introduced an oxygen dependency. Within this approach, the major deficiency was the absence of molecular nitrogen. Therefore introducing the additional pathway to produce N_2 via N_2O could improve this TOF. For that the energy parameters for the reactions 3.10 have to be calculated with the RPBE XC-functional. Since the difference between the energy barriers of the basis reactions evaluated with PBE and RPBE respectively were not severely high, it is assumed that this is also the case for the reactions concerning N_2O. Therefore as a preliminary estimate, the PBE values are used.
Since the surface is rather empty under the conditions caused by the RPBE XC-functional it might be further helpful to include the reactions that allow the hydrogen atoms to diffuse along the NH_x and OH_x species[28]. Furthermore the TOF of NO was below the experimentally measured TOF. Therefore the ZPE correction for the NO binding energy as well as lateral interactions between NO and N and NO and NH_2, respectively, are introduced as an additional treatment to the reaction network to lower the binding energy of NO in this special configuration about 0.2 eV (as it was the case within the PBE framework).
Combining these four approaches does neither increase the TOF of NO nor the TOF of N_2 in corresponding kMC simulations. The surface is, as stated before, in the single RPBE approach still only occupied by few oxygen and OH groups. The case of an N atom next to NO never occurs, as the NO desorbs before this can happen. In the same manner the NH_x diffusion is never performed as none of this species is present on the surface. Therefore the resulting TOF diagram is similar to what was achieved by applying the RPBE approach within the first simulations comprising just the basis reactions (see diagram 3.20): The oxygen pressure dependency is existing

---

[28] For the same reasons as mentioned above the values calculated with the PBE functional were taken as a very first attempt.

for NO, but no N_2 is formed at all.

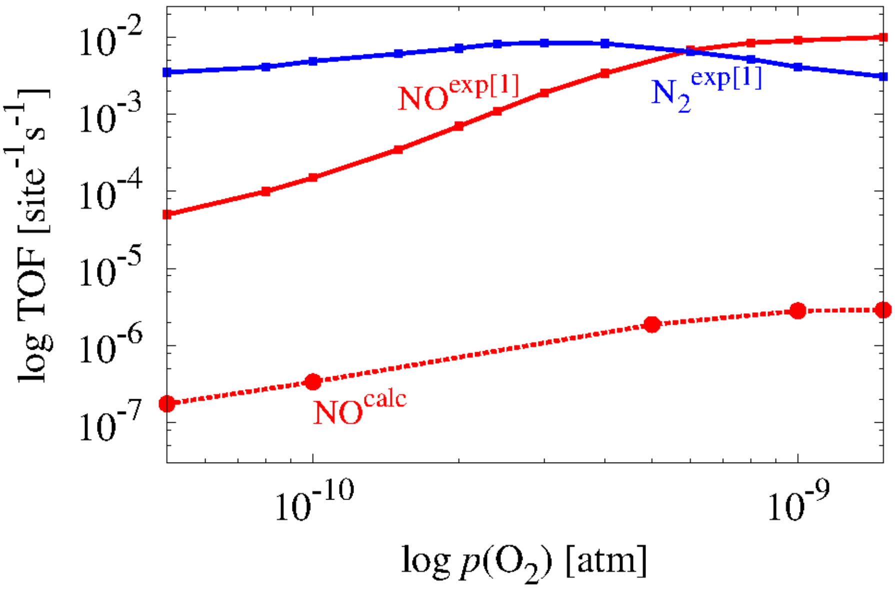

Figure 3.20: TOF vs. oxygen pressure at $T = 500\,\mathrm{K}$, resulting from a combination of the RPBE-treated basis reaction with N_2 formation via N_2O (flat lying *and* upright) as well as consideration of hydrogen diffusion along NH_x species and lateral interactions. (Straight lines represent again the experimental [1], dashed lines the calculated results. Red lines represent NO, blue lines N_2).

On the other hand, severely increasing the ammonia pressure to $p(NH_3) = 10^{-4}$ atm changes the TOFs significantly (see diagram 3.21). The TOF of NO is reproduced very well for the low pressure range. Furthermore, the nitrogen desorption could be introduced to this reaction network. The nitrogen desorption rate is almost identical with the desorption rate of NO and no cross-over of the two curves could be observed. Both TOFs reach their maximum at a far higher oxygen pressure than measured in the experiment. Only at a pressure above 10^{-8} atm the TOFs start to drop – the TOF of N_2 at least faster than the TOF of NO. This severe change in the TOF is due to the higher ammonia pressure and the accordingly higher surface occupancy of NH_x species. The observed pressure ranges are far off the experimental UHV conditions and therefore even a better agreement than achieved here would not be a proof for the accuracy of this combined approach.

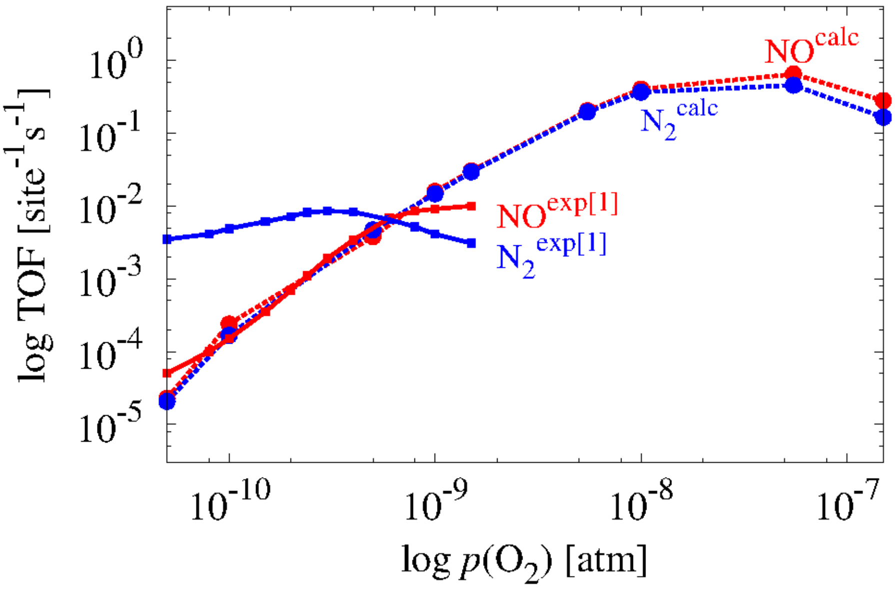

Figure 3.21: TOF vs. oxygen pressure with a – compared to the experimental values [1] – severely higher $p(NH_3) = \text{const} = 10^{-4}$ atm at $T = 500$ K, resulting from a combination of the RPBE-treated basis reaction with N_2 formation via N_2O (flat lying *and* upright) as well as consideration of hydrogen diffusion along NH_x species and lateral interactions (Straight lines represent again the experimental [1], dashed lines the calculated results. Red lines represent NO, blue lines N_2). Note that the experimental results [1] shown here are measured under a far lower ammonia pressure and are displayed only for comparison.

3.5.2 Combined PBE approach

Though there was no sensitivity towards the oxygen pressure, the basis reactions treated with the PBE XC-functional should also be tested with the promising additional approaches. The inclusion of the ZPE correction for the NO molecule as well as the lateral interactions between NO and the two other adsorbates, N and NH_2, looked particularly promising as this brought the TOF of NO closer to the regime observed in experiment. Furthermore, the diffusion of hydrogen atoms along NH_x led to a surface occupancy confirmed by the HREELS experiments. The thus introduced NH_2 could even have a further influence on the afore mentioned lateral interactions and with that on the desorption rate of NO. Additionally the new reaction pathways to form molecular nitrogen via the N_2O molecule lifted the desorption rate of N_2. These four concepts are therefore also chosen for the PBE approach to be combined within one kMC simulation. The resulting TOFs are shown in diagram 3.22.

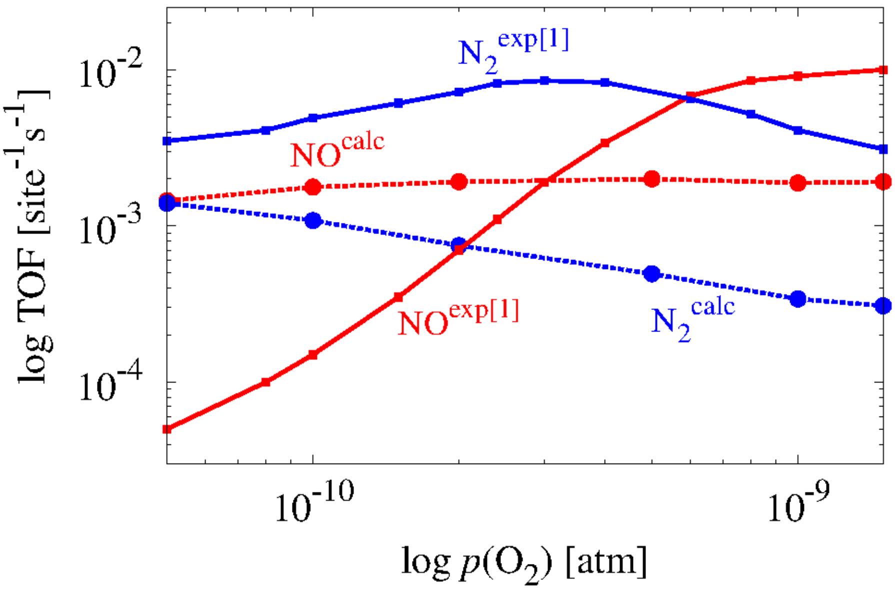

Figure 3.22: TOF vs. oxygen pressure resulting from a combination of the basis reaction with lateral interactions as well as consideration of hydrogen diffusion along NH_x species and N_2 formation via a flat lying N_2O at $T = 500\,\text{K}$, $p(NH_3) = \text{const} = 10^{-10}$ atm (Straight lines represent again the experimental [1], dashed lines the calculated results. Red lines represent NO, blue lines N_2).

The TOF diagram implies that the combination of the several features added to the basis reaction network can indeed introduce a sensitivity concerning the oxygen pressure: For a very low oxygen pressure the TOF of N_2 is equal to the TOF of NO and decreases with increasing oxygen pressure. For even lower oxygen pressures the TOF of N_2 could therewith even exceed the TOF of NO. To confirm this, kMC simulations were performed with lower (and higher) oxygen pressure. The extended TOF diagram is shown in diagram 3.23.

The TOF diagram now clearly reveals that there is an oxygen-pressure dependency of the TOF of NO and N_2: With lower oxygen pressure the N_2 desorption rate is

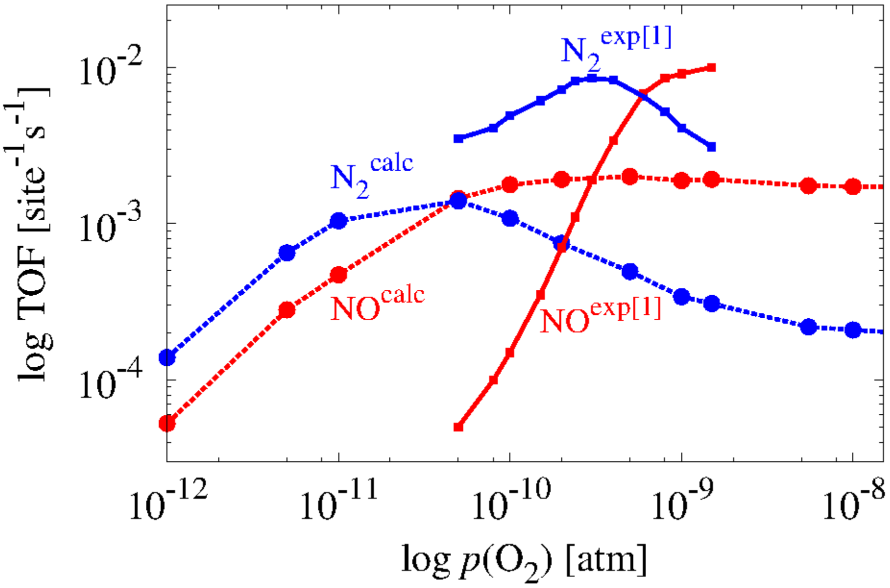

Figure 3.23: Larger range of the TOF vs. oxygen diagram pressure resulting from a combination of the basis reaction with ZPE correction of NO lateral interactions as well as consideration of hydrogen diffusion along NH_x species and N_2 formation via a flat lying N_2O at $T = 500\,K$, $p(NH_3) = const = 10^{-10}$ atm (Straight lines represent again the experimental [1], dashed lines the calculated results. Red lines represent NO, blue lines N_2).

higher than the NO desorption rate. Therewith this reaction network can reproduce the cross-over of the two TOF curves as found in experiment [1]. This cross-over appear at a remarkably lower pressure than in the experiment (approx. one order of magnitude difference). Furthermore the TOFs of NO as well as N_2 are smaller than the ones found in experiment.

The coverage of the surface changes with increasing oxygen pressure as follows: Starting from a completely empty surface at extremely low oxygen pressure, NO starts to be constantly present. Similarly but less distinct O atoms appears on the surface. The maximum of the TOF of N_2 coincides with the maximum number of N atoms on the surface: $\approx 5\%$ of the sites are occupied with this species. With higher oxygen pressure the amount of N drops again to $1-2\,\%$. At this point $\approx 55\,\%$ of the *cus* sites on the surface are still empty, while $\approx 20\,\%$ are occupied with NO. Atomic oxygen occupies ≈ 10 of the surface sites.

Increasing the oxygen pressure further the number of empty sites drops further while the amount of oxygen and NO increase simultaneously. When these three species occupy approximately the same number of sites (≈ 28%), the maximum desorption rate of NO is reached. After this point the amount of empty sites drop to its lower limit of ≈ 20 %, while the amount of NO drops only slightly to 25%. The amount of oxygen increases up to its upper limit of ≈ 40%. The evolution of the coverage of the main species with increasing oxygen pressure is depicted in diagram 3.24.

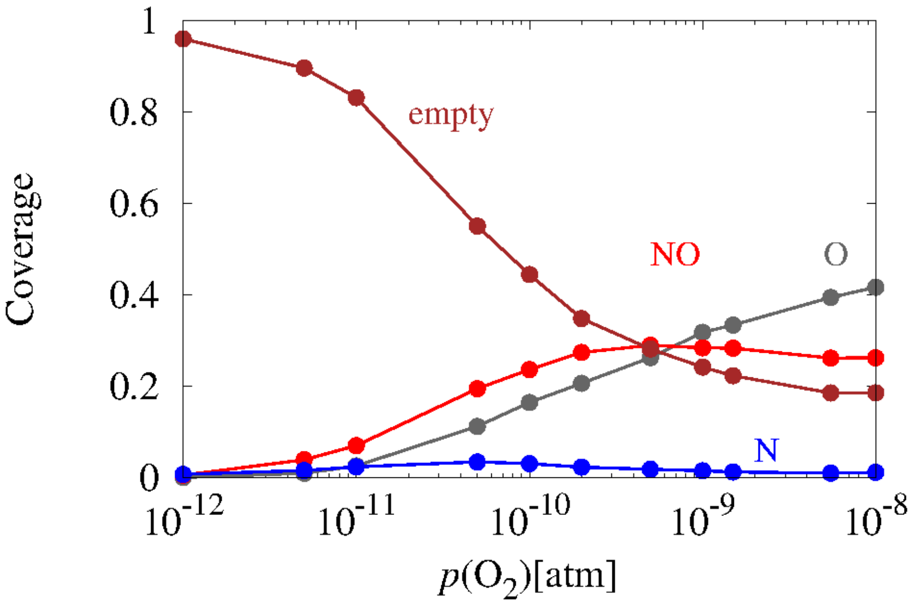

Figure 3.24: Coverage of the main species for the initially defined 41 basis reactions and ZPE correction of NO, lateral interactions as well as hydrogen diffusion and the reactions concerning N_2O at $T = 500\,\mathrm{K}$, $p(\mathrm{NH_3}) = \mathrm{const} = 10^{-10}$ atm.

For very low pressures of oxygen approximately only one third of the desorbing nitrogen is formed via a flat lying N_2O molecule. The main part is formed via the combination of two N atoms due to the low amount of NO on the surface. The fraction of N_2 generated from N_2O however increases with increasing oxygen pressure and reaches its maximum (approximately three-fours) when the TOF of N_2 is highest. After passing this maximum, the share of molecular nitrogen from NO and N via reaction 3.10 drops again to its former value since the number of empty sites declines.

At a certain pressure the critical mass of NO and O on the surface is reached and molecular nitrogen is no longer the main product. At this point the amount of NO that is constantly present on the surface starts to drop slowly but consequently, while the amount of oxygen increases simultaneously.
The desorption of N_2O follows in principle the trend of the desorption of N_2 though the TOF of N_2O is constantly smaller: It starts with $1 \times 10^{-5}\,\mathrm{site}^{-1}\,\mathrm{s}^{-1}$ for the small oxygen pressure regime, reaches its maximum of $4.3 \times 10^{-4}\,\mathrm{site}^{-1}\,\mathrm{s}^{-1}$ at a pressure of $p(\mathrm{O}) = 10^{-10}$ atm and drops again to a value of $1 \times 10^{-5}\,\mathrm{site}^{-1}\,\mathrm{s}^{-1}$. It stays therewith also consequently below the TOF of NO. To further illustrate the relation between the two main products, NO and N_2, their selectivities are analyzed in the following: The selectivity s_x is the portion of the desorption rate (the TOF) that a product molecule has on the overall desorption. For NO and N_2 respectively this means:

$$s_\mathrm{NO} = \frac{\mathrm{TOF}_\mathrm{NO}}{\mathrm{TOF}_\mathrm{NO} + \mathrm{TOF}_{\mathrm{N}_2}} \tag{3.11}$$

and

$$s_{\mathrm{N}_2} = \frac{\mathrm{TOF}_{\mathrm{N}_2}}{\mathrm{TOF}_\mathrm{NO} + \mathrm{TOF}_{\mathrm{N}_2}} \tag{3.12}$$

The selectivities for NO and N_2 change congruently with their TOFs: At a low oxygen pressure N_2 starts with a rather low selectivity of only $\approx 72\,\%$. It drops analogue to the rise of the selectivity of NO until the selectivity for the latter converges towards a limit of $\approx 90\,\%$, leaving a selectivity of $10\,\%$ for N_2. The evolution of the selectivities is shown in diagram 3.25. For comparison, the selectivities as measured in the experiment [1] are displayed as well. These selectivities appear in accordance with their TOFs in a rather narrow pressure range compared to the kMC simulations presented here. Furthermore, the experimental selectivity for NO is slightly lower ($80\,\%$) than the one achieved in the simulations. However, at only slightly higher temperatures ($T = 530\,\mathrm{K}$) the selectivity measured in experiment was almost 100%
To compare with the ambient-pressure experiments of Perez-Ramirez *et al.* [14] the combined reaction scheme was also applied to these higher pressures. It appears that N_2 is the favored product at a low oxygen-ammonia pressure ratio. This changes when the oxygen amount is higher (oxygen-ammonia pressure ratios of 5:1 and 10:1). N_2O is always the minor product: Its amount decreases with increasing oxygen pressure quota. The TOFs at ambient-pressure are summarized in table 3.28. The surface comprises – in contrast to the UHV experiments in which NO as well as O and OH dominate the surface – also ammonia molecules. For a visual comparison with the experiment, the selectivities are displayed in diagram 3.26. Unfortunately the simulated results could not reproduce the experimental findings at all: The selectivity of NO is too high and the selectivity of N_2 is too low compared to the experimental measurements in [14]. Furthermore these lines cross, which implies that there is an

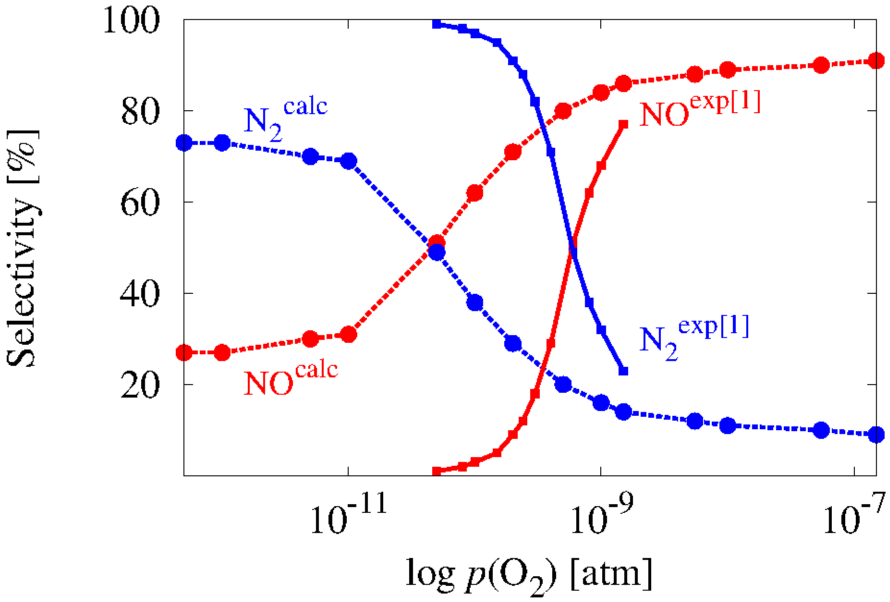

Figure 3.25: Selectivity for the reaction network comprising the initially defined 41 basis reactions as well as ZPE correction for NO, lateral interactions, hydrogen diffusion and N_2O reactions at 500 K, $p(NH_3) = \text{const} = 10^{-10}$ atm (Straight lines represent again the experimental [1], dashed lines the calculated results. Red lines: NO, blue lines: N_2)

Ratio $p(O_2)/\,p(NH_3)$	TOF(NO) [site^{-1} s^{-1}]	TOF(N_2) [site^{-1} s^{-1}]	TOF(N_2O) [site^{-1} s^{-1}]
2:1	5.7×10^{-3}	8.2×10^{-3}	2.4×10^{-3}
5:1	5.2×10^{-3}	6.0×10^{-3}	1.9×10^{-3}
10:1	4.6×10^{-3}	4.4×10^{-3}	1.4×10^{-3}

Table 3.28: TOFs for the reaction network comprising the basis reactions as well as lateral interactions, hydrogen diffusion and the formation, diffusion and desorption as well as decomposition of the N_2O molecule at ambient pressures: $p(O_2) = \text{const} = 1 \times 10^{-1}$ atm, $p(NH_3) = 5 \times 10^{-2}$, 2×10^{-2}, 1×10^{-2} atm.

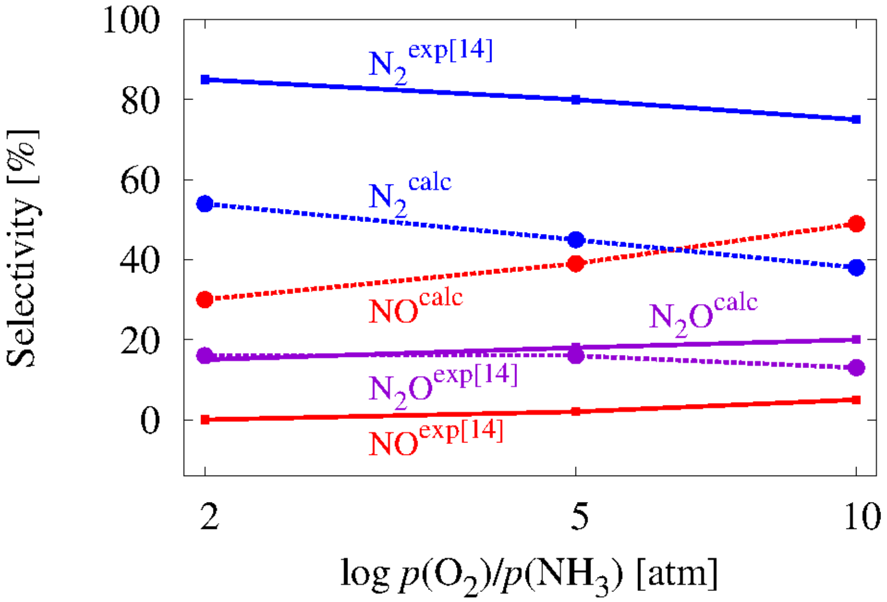

Figure 3.26: Selectivity for the reaction network comprising the initially defined 41 basis reactions as well as lateral interactions, hydrogen diffusion and N_2O in both orientations at ambient pressure and $T = 500\,K$ (Straight lines represent again the experimental [14], dashed lines the calculated results. Red lines: NO, blue lines: N_2, violet lines: N_2O).

oxygen dependent change of the preferred product. The results for the N_2O molecule shows indeed the selectivity as measured in experiment. Yet, the trend that the desorption of this species occurs more often than NO but less often than N_2 could not be reproduced.

3.5.3 Summary

The extension of the PBE-treated basis reaction network with the hydrogen diffusion along the NH_x and OH_x as well as the lateral interactions between NO and its neighbors N and NH_2 and the new intermediate N_2O improve the overall TOF evolution of NO as well as N_2. Though spanning a far wider oxygen pressure range, an oxygen sensitivity is introduced and the TOFs are advanced by several orders of magnitude reaching the TOF values achieved in the UHV experiments of Wang *et al.* Describ-

ing the reaction network with energy barriers evaluated with the PBE XC-functional leads to promising results when comparing with the experiment [1]: With this approach not only an oxygen pressure dependence but also a cross-over between the two TOFs of NO and N_2 is reproduced: At low oxygen pressures the production of N_2 is favored, at higher oxygen pressures the desorption of NO is superior. With the RPBE XC-functional approach this cross-over can not be introduced to the reaction network. Furthermore a far higher ammonia pressure is necessary to reach the TOFs reported in the experiment.
As the results from kMC simulations using the barriers from PBE XC-functional are superior to the ones achieved within the RPBE approach, the ambient-pressure calculations are only performed within the former approach. The tendency – more N_2 than NO – agree only for a low oxygen-ammonia ratios of 2:1 and 5:1 with the experiment [14]. Furthermore more NO than N_2O is produced for all pressure ratios. Furthermore the trend of the N_2O desorption concerning the different pressure regimes is not reproduced consistently: Under UHV conditions the desorption of this molecule could be observed during the calculations though the corresponding experiments in [1] claimed that they found none of it. Furthermore, N_2O was found to desorb even less at ambient pressure than at UHV. Therefore it is obvious that the so far compiled reaction network still has its deficiencies: Especially the processes connected with the N_2O molecule seem to be fragmentary.

3.6 Further ideas and dead ends

3.6.1 N_2O desorption for different pressure regimes

The pressure dependence is directly connected with the surface coverage – this comprises the number of empty sites as well as the configuration on the surface. A pressure dependence concerning the N_2O could therewith already be introduced via reaction 3.10 which requires an empty site[29]. Another ansatz could be the different surface occupancies at different pressure regimes. As mentioned before the amount of ammonia molecules is at ambient pressure by far higher than under UHV condi-

---

[29] The already included diffusion processes belong to this type of reaction. Following the afore described theory, the N diffusion should increase the N_2 formation at a rather empty surface (UHV conditions) and this effect should then disappear at a highly occupied surface. Yet, the higher N_2 desorption at low coverages is not owed to this process as it has a too high barrier and the effect results rather from the decomposition of N_2O. This example should emphasize that a promising process for the formation or decomposition of N_2O should have a reasonable energy barrier that can be overcome.

tions. Lateral interactions between N_2O and the corresponding surface species could therefore be crucial for a desorption of the former – for example when the neighboring species affect the swing from the flat lying N_2O to the easier desorbing upright standing N_2O. Different neighbors surely introduce also different and new reaction pathways, which could be essential to grasp the main features of this complex reaction network.

3.6.2 More N_2

The amount of desorbing N_2 molecules was too low throughout all kMC simulations. It could already be increased by adding the additional pathway of the combination of NO + N to flat lying N_2O which finally led to the decomposition of N_2O to molecular nitrogen (reaction 3.10). To *further* increase the N_2 formation and accordingly its desorption another reaction to increase the amount of the intermediate N_2O in its flat orientation could therefore be helpful. With regard to the surface configuration under UHV conditions which exhibits a high occupancy with NO an alternative channel to produce the N_2O molecule could be the following reaction[30]:

$$2\,\mathrm{NO} \rightleftarrows (\mathrm{NO})_2 \rightleftarrows \mathrm{N_2O_{flat}} + \mathrm{O} \tag{3.13}$$

Unfortunately the energy difference between the IS and FS of this reaction is already 2.5 eV. The barrier for the formation of the N_2O molecule would therefore be at least as high as this difference and this rules out this pathway. This indirectly confirms again the high binding energy of the NO molecules on the surface.

3.6.3 A new surface species: hydroxylamine

A so far not discussed intermediate species within this reaction network could be hydroxylamine. This species could be formed via the following reaction:

$$\mathrm{NH_2} + \mathrm{OH} \rightleftarrows \mathrm{H_2NOH} \tag{3.14}$$

The energy difference between IS and FS adds up to only 0.81 eV, implying that the reaction barrier could be of a reasonable height for the reaction to occur. The advantage of this mechanism is that no NH is involved which corresponds to the experimental findings in [1]. In the gas phase hydroxylamine is known to decompose according to the following reaction [116]:

$$3\,\mathrm{H_2NOH} \rightleftarrows \mathrm{NH_3} + \mathrm{N_2} + \mathrm{H_2O} \tag{3.15}$$

---

[30] as proposed in [2] and investigated in [29] on Pt.

The hydroxylamine could thus constitute a source for molecular nitrogen as an end product. Furthermore, the computed binding energy of H_2NOH is with 1.46 eV low enough to allow an efficient desorption of this molecule at the temperature of interest. Unfortunately, the complicated disproportionation process of reaction 3.15 would represent a formidable challenge for a NEB calculation. In gas phase this reaction is reported to appear at temperatures as low as 100 K, which is far lower than the temperatures applied in the experiments of interest [1, 14] and the kMC simulations presented here. A first attempt could therefore be to include only the formation and the desorption process of the hydroxylamin to the reaction network and assume that the decomposition follows immediately above the surface.
Unfortunately there is no data for the hydroxylamin molecule in the thermodynamic tables [106]: An evaluation of the chemical potential $\Delta\mu$ and further the desorption process rate constant of this molecule as described in 2.4.5 is therewith not applicable. Hence, the chemical potential has to be derived as described in 2.4.4, which is far from being a trivial task for molecules like hydroxylamin that contain more than two atoms.

3.6.4 An oddly adsorbed NO

When searching for a way to the low TOF of NO as resulting from the initial kMC simulations comprising just the basis reactions, not only the configuration, namely the neighbors on the surface around the NO molecule could be of interest, but also the *orientation* of the molecule. NO was so far considered to bind to the surface via the N atom. The opposite orientation, with the oxygen closer to the surface, is far less stable (2.27 eV vs. 0.54 eV). Naturally the NO molecule tends to be oriented in the more stable way, but what if there is a reaction that produces the 'oddly' oriented ON molecule? Such a reaction could be a flip reaction either performed on one *cus* site or from one to another *cus* site (see reactions 3.16 and 3.17).

$$\mathrm{NO} \rightleftarrows \mathrm{ON} \tag{3.16}$$

$$\mathrm{NO} + * \rightleftarrows * + \mathrm{ON} \tag{3.17}$$

The computed energy barriers for the flip from NO to ON are rather high (1.98 eV for the flip on one site and 1.67 eV for a flip from one to another site[31]), though not too high to not possibly occur at the pressure and temperature range of interest. The back reaction has in both cases a much lower barrier though (0.2 eV in both cases)

---

[31] evaluated with the drag method.

and therefor a flip reaction will always be followed by immediate back reaction like it was the case for the decomposition of NH into N and H (see eqn. 3.3).
A further way to desorb an NO molecule would be via an associative desorption of N and O (like the desorption of O_2): Though this reaction exhibits a barrier of only 1.95 eV, it is in direct competition with the formation of NO adsorbed on a *cus* site which has a by ≈ 1.2 eV lower barrier.

3.6.5 A look on the *br* site

In the beginning it was stated that the reaction with the oxygen atoms occupying the *br* sites is rather unlikely due to their high binding energy. Nevertheless, an interaction with these oxygen atoms can not completely be excluded. As a possible process the diffusion of a NO molecule to these oxygen atoms was investigated with the drag method: This could form a new surface intermediate NO_2 which is also stable in the gas phase and could therefore desorb:

$$\mathrm{NO} + \mathrm{O}_{br} \rightleftarrows \mathrm{NO}_{2,br} + * \rightleftarrows \mathrm{NO}_2(g) \tag{3.18}$$

Furthermore the NO molecule could desorb from the O_{br} as this process exhibits a barrier of only 0.87 eV:

$$\mathrm{NO} + \mathrm{O}_{br} \rightleftarrows \mathrm{NO}_{2,br} + * \rightleftarrows \mathrm{NO}(g) + \mathrm{O}_{br} \tag{3.19}$$

The diffusion of the NO molecule to the O_{br} atom has actually a reasonable barrier of 1.52 eV. Unfortunately its back diffusion is activated by only 0.2 eV. Therefore no desorption, but only this back reaction is expected. The experiments of Wang *et al.* [2] and Perez-Ramirez *et al.* [14] indeed agree in the fact that no NO_2 desorption takes place, though the formation of NO_2 and the split (at $T = 250\,\mathrm{K}$) was detected in [2, 33].

Chapter 4

Conclusion and outlook

Chemical reactions on surfaces, as they occur in heterogeneous catalysis, usually consist of several intermediate steps: The more reactants are involved in the chemical reaction and the bigger these reactants are, the more complex and numerous are these involved intermediate steps. The number of these elementary steps can further literally explode if concepts like selectivity or diverse sites on a catalyst surface are included. The comprehensive investigation of intrinsically large reaction networks is therewith from both the experimental as well as the theoretical side a demanding, not to say a yet impossible task.

To address such large reaction networks from a theoretical point of view, in the present work a *sensitivity-guided* multiscale modeling approach was developed: The basis of this hierarchical method is the evaluation of the energetic parameters of elementary steps of a reaction network from first principles. Moving to bigger time and length scales kinetic Monte Carlo (kMC) follows as the computational tool to show the statistical interplay of these elementary steps. This approach was already successfully applied to the catalytic oxidation of CO to CO_2. However, the number of processes within this reaction network is on the lower level.

To approach chemical reactions with considerably more elementary steps a *sensitivity-guided* refinement of the investigated reaction network was attached to the multiscale modeling scheme. This refinement shall identify the rate limiting steps in a reaction network so that the focus of detailed analysis of the computationally demanding first principles evaluation can be restricted to a minimum. To identify these crucial processes as many methods as possible are accessed: Among these is with a high priority chemical intuition, as the handling of huge reaction networks requires a detailed understanding of the participating molecules and their interactions. Furthermore we reverted to *ab initio* thermodynamics as a representative of the computationally low-demanding methods. In this context also briefing from literature was used. The refinement is an iterative process in order to investigate only as many reactions as necessary and to thoroughly understand their impact.

The refined multiscale modeling approach was exemplified for the example of the oxidation of ammonia at the $RuO_2(110)$ surface. This first step of the well-known Ostwald process has two competing end products: Molecular nitrogen as well as nitrogen monoxide are both thermodynamically stable. The reactants of this reaction are ammonia and oxygen. Even though there are solely two educts and two products, the list of possible elementary steps is extensive: The reason for this is the ability of nitrogen to host a multiplicity of different oxidation states ranging from $+5$ in nitric acid to -3 in ammonia. This is the basis for a lot of possible intermediate reactants, like azanes, azenes and azadiens but also nitrogen-oxides and nitrogen-hydroxides. Though a lot of these reactants are not stable or only short-living in the gas phase, their formation has to be considered in the environment of a solid catalyst surface. Therewith more than 200 possible elementary steps were identified within the present work as being reasonable from a chemical point of view (see also appendix C).

To pick a significant initial setup of elementary steps to initialize the refinement loop of the *sensitivity-guided* multiscale modeling approach several attempts were accessed: First of all, chemical intuition led to a set of basis reactions that formed the core and starting point of the whole work. These reactions were evaluated on a first principles level. As binding energies are of high importance within this catalytic surface reaction, two different exchange correlation (XC) functionals, PBE and RPBE, were applied. These XC-functionals are known to mark a somewhat lower and upper boundary, respectively, for the strength of a bond of an adsorbate.

In addition an *ab initio* thermodynamics phase diagram of the underlying system was assembled. This phase diagram gave valuable first insights into the surface occupancy and the corresponding stability concerning different pressure and temperature regimes. These insights motivated the focus on only one kind of active site in the ensuring kinetic modeling (though the $RuO_2(110)$ surface exhibits in principle two dominant adsorption site types).

Initial kMC simulations with this limited basis set of reactions could not show any agreement with the UHV experiment [1] which served as the benchmark for the microkinetic modeling results: The main aim was to reproduce the overall trend of the TOFs of NO and N_2, as well as the oxygen pressure dependency. An extra would be the quantitative determination of these TOFs in agreement with the experiment. Unfortunately the simulated TOFs of NO and N_2 did not show any sensitivity to the oxygen pressure. Furthermore, the trend – more N_2 than NO for low oxygen pressure and vice versa for high oxygen pressure – could not be introduced within the simulations. Additionally, both TOFs were consequently lower than the TOFs measured in the experiment. However, the distribution and occurrence of the adsorbates on the surface could be studied within these initial simulations. To start the refinement cycle possible reasons for the deviation from experiment were therewith identified and processes that could find a remedy for these deviations were successively added to the reaction network. This identification was supported and could benefit from a variety of accessible information from literature – from theory as well as from experiment. The effect of every considered process (or class of processes) on the reaction network was evaluated separately by reinitializing several kMC simulations with only one single improvement attempt at the time to attain a systematic evaluation of each of the variations.

None of the first attempts could *significantly* improve the agreement with the experiment. An oxygen pressure dependency of the TOF for NO could only be introduced within the simulations using energy parameters evaluated with the RPBE XC-functional (and this simulation predicted then no N_2 desorption at all!) Yet again the analysis of the TOFs as well as the distribution and occurrence of adsorbates on the surface could show that the results and therewith the agreement with the experiment were improved: Simulations comprising the lateral interactions between NO and other adsorbates and the ZPE correction of the NO binding energy, respectively, could increase the TOF of NO significantly and brought it closer to the experimentally measured values. The hydrogen diffusion reactions along NH_x and OH_x improved the surface occupancy by introducing NH_2 – a species which was clearly identified in the HREELS experiment but did not occur in the initial simulation. Finally the introduction of the N_2O intermediate and the corresponding formation and decomposition processes allowed for a higher N_2 desorption rate, closer to the value measured in the experiment.

According to the therewith gained insights further kMC simulations comprising diverse *combinations* of the promising innovations were run to investigate the effect of them on each other. The interplay of the various innovations did indeed further improve the simulation results: The oxygen pressure dependency of the desorption of the two main products NO and N_2 could be reproduced qualitatively. Furthermore, N_2 appeared to be the main product within the low oxygen pressure regime, while NO desorbs more frequently in the high pressure regime – as it was anticipated in the experiment. Albeit it has to be admitted that the change of the TOFs of NO and N_2 sprawl over a broader pressure range than observed in the experiment. Additionally the absolute values of the TOFs are still certainly lower than in the experiment. This could clearly show that the individual processes within the observed reaction network act and *re*-act on each other and therewith have (concerted) effects concerning the overall reactivity (and selectivity) of the catalytic process. However, the behavior at ambient oxygen pressures (see [14]) could not be reproduced with the so far extended reaction network and especially the role of the intermediate/ product N_2O in the different pressure regimes could not yet be explained. Furthermore, a quantitative agreement of the simulated TOFs with the experimentally evaluated ones would be desirable.

The reaction network would further benefit from the investigation of additional processes (as many as possible), but also from a deeper analysis of the basics presented here: Processes formerly appearing as useless could for example later play a (decisive) role within the interplay of other new attempts. However, such a thorough analysis of all possibilities and all combinations of these possibilities goes beyond the scope of any theoretical investigation that is feasible nowadays.

It would therefore be highly desirable to extend the *sensitivity-guided* refinement by additional methods. Of great help would be to find a method to estimate the energetic parameters on a low-cost level in terms of computer power which delivers reasonable results rather than be guided only by chemical intuition. Such a method could be the unity bond index-quadratic exponential potential (UBI-QEP) method [117] that is by now only thoroughly tested for metals, but not for metal oxides. With such a crude but quick estimate of the energy barriers of potential processes the list of events that a kMC simulation accounts for could be extended and adjusted very fast to study the importance of any process that is therewith added. This would introduce an additional tool to further support the idea of a *sensitivity-guided* refinement of the multiscale modeling approach and thereby extending it to complex chemical kinetics.

Abstract

Reaching a high selectivity in surface catalytic processes with more than one thermodynamically feasible product is nowadays one of the major ambitions in catalysis. Compared to the overall activity our present atomic-scale understanding of the mechanisms driving such selectivity is very shallow. On the modeling side, this concerns notably quantitative simulations aiming at a first-principles based microkinetic description. While corresponding modeling has already led to significant advances in the understanding of simple model reactions with one product (like the CO oxidation reaction), the approach is severely challenged by the excessive number of elementary processes in more complex reaction networks offering different possible end products. An exhaustive determination of all kinetic parameters of all elementary processes from first-principles represents at present in most cases still a prohibitive computational cost.

Using the catalytic oxidation of ammonia to nitrogen monoxide and molecular nitrogen as a showcase an extended approach based on an iterative *sensitivity-guided* refinement will be explored in this work. Starting with a core set of elementary processes and their first-principles kinetic parameters, additional processes will initially be considered at a low-level description in the kinetic Monte Carlo based microkinetic simulations. Sensitivity analyses will then be systematically employed to identify those rate-limiting steps in the network which require a more accurate first-principles treatment. Using correspondingly refined kinetic parameters for the latter steps the simulations will be re-initiated, new processes considered and potentially refined until a self-consistent description has been reached. It is expected that this procedure, which concentrates the first-principles calculations on a subset of all feasible elementary processes, will reduce the computational burden to an extend to make also more complex reaction networks and their sensitivity features amenable to the detailed investigation by first-principles mikrokinetic modeling. Here, reduced means essentially just tractable.

Zusammenfassung

Die Selektivität katalytischer Prozesse ist eines der drängenden Themen in der Katalyse-Forschung. Verglichen mit Untersuchungen zur *Aktivität* eines Katalysators ist diesem Gebiet der Oberflächen-Chemie bislang jedoch eher geringe Aufmerksamkeit geschenkt worden: Nur wenig ist bekannt zu den Mechanismen, die Selektivität in Prozessen mit mehr als einem thermodynamisch stabilen Endprodukt bedingen – besonders theoretische Untersuchungen hierzu fehlen. Die Modellierung einfacher chemischer Prozesse (mit nur einem thermodynamisch stabilen Endprodukt) hat in der Vergangenheit bereits deutlich zu deren Verständnis beitragen können. Dies zeigen quantitative Simulationen zur Oxidationsreaktion von CO zu CO_2 mit Hilfe eines mikrokinetischen Modells auf der Basis von *ab initio* Dichtefunktional-Rechnungen beispielhaft. Eines der größten Hindernisse bei diesem Ansatz ist allerdings die Anzahl der beteiligten Elementarreaktionen, die bei komplexeren Reaktionsnetzwerken schnell zum geschwindigkeitsbestimmenden Schritt innerhalb der Modellierung werden kann: In den meisten Fällen – und besonders bei Reaktionen, die Selektivität aufweisen – gibt es schlicht zu viele mögliche Elementarprozesse, als dass eine Bestimmung der entsprechendnen kinetischen Parameter durchführbar wäre.
Am Beispiel der katalytischen Oxidation von Ammoniak soll in dieser Arbeit deshalb ein erweiterter Ansatz zur *ab initio* basierten mikrokinetischen Modellierung entwickelt werden. Das Reaktionsnetzwerk soll dabei schrittweise, basierend auf einer Sensitivitätsanalyse, erweitert werden: Die Basis dazu bilden wenige Elementarreaktionen, deren kinetische Parameter mit *ab initio* Methoden bestimmt werden. Die Beschreibung zusätzlicher Prozesse, die dem Reaktionsnetzwerk hinzugefügt werden sollen, erfolgt dann zunächst mit Hilfe ungenauerer, computertechnisch aber weit weniger kostspieliger Methoden. Eine Sensitivitätsanalyse der Ergebnisse aus den mikrokinetischen (kinetischen Monte Carlo-) Simulationen soll die für das Reaktionsnetzwerk entscheidenden Prozesses identifizieren. Die kinetischen Parameter dieser Prozesse werden dann durch *ab initio* Berechnung verfeinert und die Simulation reinitialisiert. Neue Reaktionen werden so lange untersucht und dem Netzwerk hinzugefügt bis eine ausreichend genaue Beschreibung desselben erreicht ist. Es wird erwartet, dass diese Methode die erforderlichen computertechnisch teuren *ab initio* Berechnungen auf ein Minimum beschränkt, um somit in Zukunft auch komplexe Reaktionsnetzwerke für die mikrokinetische Modellierung auf der Basis von *ab initio* Dichtefunktional-Rechnungen zugänglich zu machen.

Appendix

A Structural details and convergence tests

Ruthenium dioxide crystalises in the rutile structure, having a tetragonal unit cell with the lattice parameters a = b≠c and an internal parameter u defining the distance between the oxygen and ruthenium atoms. The ruthenium atoms are therewith octahedrally coordinated by six oxygen atoms while the oxygen atoms are surrounded by three ruthenium atoms, resulting in a trigonal planar coordination. RuO_2 is metallic and therewith one of the few electronic conducting oxides. Table 4.1 shows an overview over the experimentally as well as theoretically determined lattice constants: For consistent DFT calculations the lattice parameters for the equilibrium geometry of bulk $RuO_2(110)$ have to be evaluated within this work. This was done using the Murnaghan equation of state (EOS) [123]:

Method	a	c	u
Exp. (XRD) [118]	4.49	3.11	0.306
Exp. (LEED) [119]	4.51	3.18	–
Exp. (LEED) [120]	4.51	3.23	–
Theory (PP-GGA) [120]	4.65	3.23	0.305
Theory (FP-GGA) [121]	4.52	3.13	0.306
Theory (PAW-4p) [122]	4.53	3.12	–

Table 4.1: RuO_2 lattice constants from literature.

$$E(V) = E_0 + \frac{B_0 V}{B_0'}\left(\frac{(V_0/V)^{B_0'}}{B_0' - 1} + 1\right) - \frac{B_0 V_0}{B_0' - 1} \qquad (4.1)$$

with $E(V)$ being the energy with respect to the volume of the unit cell and B_0 being the bulk modulus of the system in equilibrium. A typical Murnaghan EOS plot is shown in figure A.1.

The EOS was determined for a range of different cutoff energies and **k**points. If the key quantity, in this case the lattice constants, does not change anymore within a certain energy range, the key quantity is assumed to be converged. Diagram A.2

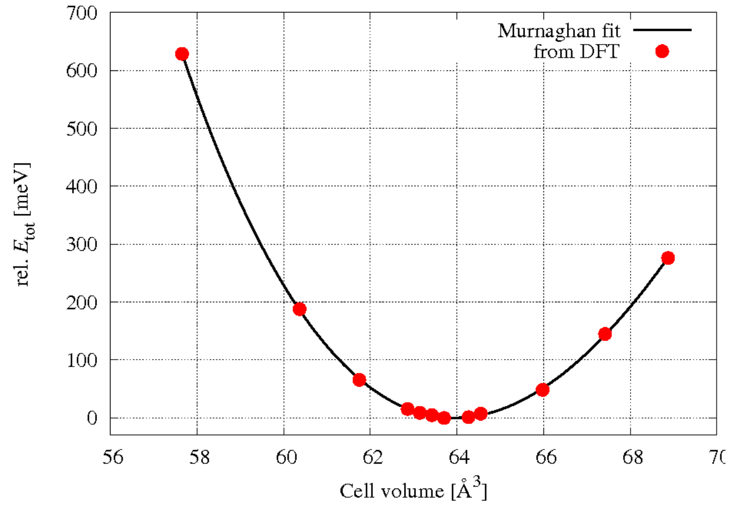

Figure A.1: Murnaghan equation of state for the setup of 6 × 6 × 6 **k**points and a cutoff energy of 400 eV.

shows the change of the lattice constant a with the cutoff energy for various **k**point sets. It is apparent that only at a cutoff energy of 400 eV the values do not deviate too much from each other. However the change between the (4 × 4 × 4) **k**point mesh and the (6 × 6 × 6) **k**point mesh is still remarkable, while between (6 × 6 × 6) and (8×8×8) **k**points the difference is negligible. Yet only at a cutoff energy of 500 eV the lattice constant a does not change any more within a range of ±0.001 Å. Therefore the parameters for the final geometry optimization are a cutoff energy of 500 eV and a **k**point mesh of (6 × 6 × 6). The resulting converged lattice constants a and c as well as the internal parameter u for the bulk RuO_2(110) are listed below:

- a = 4.52 Å
- c = 3.12 Å
- u = 0.306

This setup yields a bulk modulus of 269 GPa which is in good agreement with the literature values of 283 GPa (theory) and 270 GPa (exp.) [124].
To built the (110) facet of RuO_2 one has to cut through the bulk material diagonally. The lattice constants of the new unit cell exhibiting the surface are $a = \sqrt{2}a_{\text{bulk}} = 6.39$ Å and $b = c_{\text{bulk}} = 3.12$ Å.

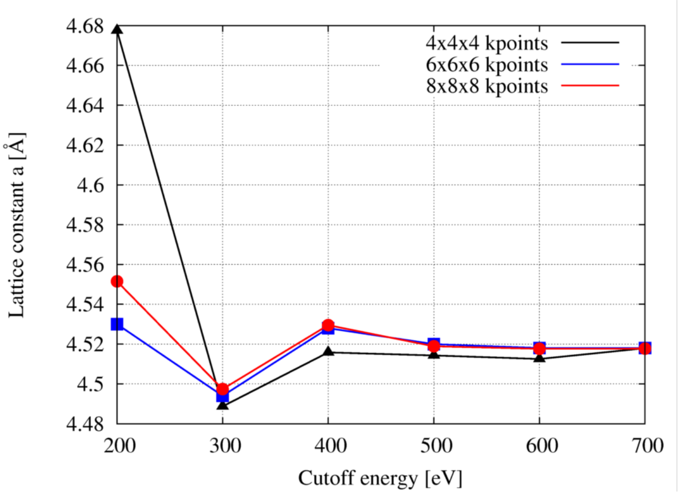

Figure A.2: Convergence test: Lattice constant vs. cutoff energy for various **k**point sets.

For the evaluation of a proper setup, namely **k**point and cutoff energy for the following DFT calculations concerning the surface, the key quantity will be the surface free energy, γ (see eqn. 2.41). Diagram A.3 shows that convergence is only reached when at least $6 \times 6 \times 6$ **k**points and a cutoff energy of 400 eV are used: With this setup the surface free energy does not change within a range of ±0.0001eV.

The surface free energy of the $RuO_2(110)$ facet was calculated as 81 meV which is in good agreement with the reported value in [125] but differs from the 71 meV/ Å reported in [126].

The third lattice constant, so to say the height of the supercell, is made up of the number of [O-Ru_2O_2-O] trilayers and the amount of vacuum between two surfaces, which are both subject to convergence tests. For the vacuum size 12 Å were determined to be sufficient so that the surfaces and atoms adsorbed on the surface do not interact with each other. However, when the convergence tests were performed it was not yet clear which adsorbates have to be treated. For big molecules, 12 Å might not be sufficient. Therefore the vacuum region was chosen to be 22 Å which allowed an upright standing N_2O molecule (which was by the time the biggest molecule considered) to not be affected by interactions with the above surface. For bigger molecules the vacuum region should be evaluated again. Since the molecules can not only feel

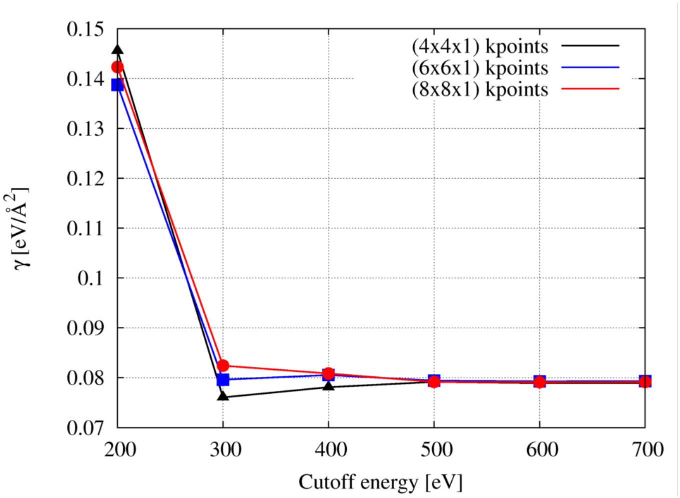

Figure A.3: Convergence test: Surface free energy γ vs. cutoff energy for various **k**point sets.

each other through the vacuum region, but also through the slab, the thickness of the slab is also a crucial parameter. It was shown before [4] that a stack of three trilayers of [O-Ru_2O_2-O] is sufficient to simulate interaction-free adsorbates on one surface.

B Final computational setup

All geometry optimization and single point energy calculations in this work were performed using the ultrasoft pseudopotential based plane wave code Cambridge Serial Total Energy Package (CASTEP) [81] in its 4.3 and 5.0 version. The geometries were modeled within the supercell approach using either a (2×1) or (3×1) supercells (depending on the complexity of the system of interest) with a vacuum size of 22 Å between two slabs. The slabs consist of three trilayers of [O-Ru_2O_2-O], of which the lower two were fixed within the calculations to simulate the surfaces' underlying bulk structure, while the upper trilayer is supposed to simulate the surface and is therefore allowed to relax in all three dimensions (for a picture of the structure see chapter results 3). All calculations were performed until convergence was reached. The convergence criteria/ parameters are listed below:
Parameters for geometry optimization and single point energy calculations:

- Cutoff energy: 400 eV
- **K**point sampling: $(6 \times 6 \times 1)$ for (2×1) cells; $(6 \times 3 \times 1)$ for (3×1) supercells
- XC-functionals: PBE and RPBE
- Grid scale: 1.75
- Energy convergence criterion: $\Delta E \leq 1 \times 10^{-5}$ eV/ atom
- Force convergence criterion: $\Delta F \leq 0.05$ eV/Å
- (Density-) Mixing scheme: Pulay
- Smearing scheme: Gaussian
- Smearing width: 0.2 eV

Nudged elastic band (NEB) calculations were performed as implemented in the atomic simulations environment (ASE) [93]. The parameters for the NEB calculations are listed below:

- Spring constant k^{S}: 0.1
- Geometry-optimizer: BFGS
- Number of images: $5 - 9$

C List of possible events on the surface

The following list of possible processes contains processes performed by one or between two adsorbates. Events of three or more interacting adsorbates are not considered. The list does not claim completeness, but should rather show the plurality of possible chemical reactions within the reaction network of the oxidation of ammonia.

Adsorption:

$$\text{Adsorbate}\,(g) + (*) \rightleftarrows \text{Adsorbate}$$

Adsorbate = O_2, NH_3

Diffusion:

$$\text{Adsorbate} + (*) \rightleftarrows (*) + \text{Adsorbate}$$

Adsorbate = O, NH_3, NH_2, NH, N, H_2O, OH, NO, N_2, N_2O, ON, H, H_2, NO_2, HNO, H_2NO, H_2NO_2, H_3NO, H_2NO_3, N_2O_2, N_2O_3, N_2O_4, N_2H, N_2H_2, N_2H_3, N_2H_4

Desorption:

$$\text{Adsorbate} \rightleftarrows (*) + \text{Adsorbate}\,(g)$$

Adsorbate = 2 O, NH_3, H_2O, NO, N_2, N_2O, ON, NO_2, HNO, H_2NO, H_2NO_2, H_3NO, H_2NO_3, N_2O_2, N_2O_3, N_2O_4, N_2H, N_2H_2, N_2H_3, N_2H_4

Reactions:

$$
\begin{array}{rcl}
\mathrm{NH_x + O} & \rightleftarrows & \mathrm{NH_{x-1} + OH} \\
\mathrm{NH_x + OH} & \rightleftarrows & \mathrm{NH_{x-1} + H_2O} \\
\mathrm{NH_x} + (*) & \rightleftarrows & \mathrm{NH_{x-1} + H} \\
\text{with x = 1, 2, 3} & & \\
\mathrm{N_{site_1} + O_{site_2}} & \rightleftarrows & \mathrm{NO_{site_1}} \\
\mathrm{N_{site_1} + O_{site_2}} & \rightleftarrows & \mathrm{NO_{site_2}} \\
\mathrm{N + N} & \rightleftarrows & \mathrm{N_2} \\
\mathrm{N_{site_1} + O_{site_2}} & \rightleftarrows & \mathrm{ON_{site_1}} \\
\mathrm{N_{site_1} + O_{site_2}} & \rightleftarrows & \mathrm{ON_{site_2}} \\
\mathrm{NO_{site_1} + N_{site_2}} & \rightleftarrows & \mathrm{N_2O_{site_1}} \\
\mathrm{NO_{site_1} + N_{site_2}} & \rightleftarrows & \mathrm{N_2O_{site_2}} \\
\mathrm{NO + N} & \rightleftarrows & \mathrm{N_2 + O} \\
\mathrm{NO_{site_1} + N_{site_2}} & \rightleftarrows & \mathrm{N_2O_{site_2}} \\
\mathrm{NO + O} & \rightleftarrows & \mathrm{NO_2} \\
\mathrm{2\,NO} & \rightleftarrows & \mathrm{N_2O + O} \\
\mathrm{2\,NO + O} & \rightleftarrows & \mathrm{NO_2} \\
\mathrm{x\,NO} & \rightleftarrows & \mathrm{NO_x(Polymer)} \\
\mathrm{N_2O} & \rightleftarrows & \mathrm{N_2 + O} \\
\mathrm{N_2O} & \rightleftarrows & \mathrm{N + NO}(g) \\
\mathrm{N_2O + O} & \rightleftarrows & \mathrm{NO + ON} \\
\mathrm{O + H} & \rightleftarrows & \mathrm{OH} \\
\mathrm{OH + O} & \rightleftarrows & \mathrm{O + OH} \\
\mathrm{2\,OH} & \rightleftarrows & \mathrm{H_2O + O} \\
\mathrm{OH + H_2O} & \rightleftarrows & \mathrm{H_2O + OH} \\
\mathrm{H + H} & \rightleftarrows & \mathrm{H_2} \\
\mathrm{OH + H} & \rightleftarrows & \mathrm{H_2O} \\
\mathrm{H + H_2O} & \rightleftarrows & \mathrm{H_2 + OH}
\end{array}
$$

$$
\begin{aligned}
\mathrm{NH_x + NH_y} &\rightleftarrows \mathrm{NH_{x-1} + NH_{y+1}} \\
\text{with x = 1, 2, 3} &\;\text{and}\; \text{y = 0, 1, 2} \\
\mathrm{N + NH} &\rightleftarrows \mathrm{N_2H} \\
\mathrm{NH + NH} &\rightleftarrows \mathrm{N_2H_2} \\
\mathrm{NH_2 + NH} &\rightleftarrows \mathrm{N_2H_3} \\
\mathrm{NH_2 + NH_2} &\rightleftarrows \mathrm{N_2H_4} \\
\mathrm{NH_2 + NH_3} &\rightleftarrows \mathrm{N_2H_5} \\
\mathrm{N_2H + O} &\rightleftarrows \mathrm{N_2 + OH} \\
\mathrm{N_2H + OH} &\rightleftarrows \mathrm{N_2 + H_2O} \\
\mathrm{N_2H_2 + O} &\rightleftarrows \mathrm{N_2H + OH} \\
\mathrm{N_2H_2 + OH} &\rightleftarrows \mathrm{N_2H + H_2O} \\
\mathrm{N_2H_3 + O} &\rightleftarrows \mathrm{N_2H_2 + OH} \\
\mathrm{N_2H_3 + OH} &\rightleftarrows \mathrm{N_2H_2 + H_2O} \\
\mathrm{N_2H_4 + O} &\rightleftarrows \mathrm{N_2H_3 + OH} \\
\mathrm{N_2H_4 + OH} &\rightleftarrows \mathrm{N_2H_3 + H_2O} \\
\mathrm{N_2H_5 + O} &\rightleftarrows \mathrm{N_2H_4 + OH} \\
\mathrm{N_2H_5 + OH} &\rightleftarrows \mathrm{N_2H_4 + H_2O} \\
\mathrm{N_2O + O} &\rightleftarrows \mathrm{N_2O_2} \\
\mathrm{NO + NO} &\rightleftarrows \mathrm{N_2O_2} \\
\mathrm{N_2O_2 + O} &\rightleftarrows \mathrm{N_2O_3} \\
\mathrm{N_2O_3 + O} &\rightleftarrows \mathrm{N_2O_4} \\
\mathrm{N_2O_4 + O} &\rightleftarrows \mathrm{N_2O_5} \\
\mathrm{NO + H} &\rightleftarrows \mathrm{NOH} \\
\mathrm{NO + H} &\rightleftarrows \mathrm{HNO} \\
\mathrm{NO + OH} &\rightleftarrows \mathrm{HNO_2} \\
\mathrm{HNO_2 + H} &\rightleftarrows \mathrm{H_2NO_2} \\
\mathrm{HNO_2 + OH} &\rightleftarrows \mathrm{H_2NO_2 + O} \\
\mathrm{HNO_2 + H_2O} &\rightleftarrows \mathrm{H_2NO_2 + OH}
\end{aligned}
$$

$$\begin{aligned}
\mathrm{HNO_2 + O} &\rightleftarrows \mathrm{HNO_3} \\
\mathrm{HNO_2 + OH} &\rightleftarrows \mathrm{H_2NO_3} \\
\mathrm{NH_2 + OH} &\rightleftarrows \mathrm{H_3NO} \\
\mathrm{NH + OH} &\rightleftarrows \mathrm{H_2NO} \\
\mathrm{N + OH} &\rightleftarrows \mathrm{NOH} \\
\mathrm{NOH + O} &\rightleftarrows \mathrm{HNO_2} \\
\mathrm{NOH + H} &\rightleftarrows \mathrm{H_2NO} \\
\mathrm{NOH + OH} &\rightleftarrows \mathrm{H_2NO + O} \\
\mathrm{NOH + H_2O} &\rightleftarrows \mathrm{H_2NO + OH} \\
\mathrm{NOH + OH} &\rightleftarrows \mathrm{N(OH)_2} \\
\mathrm{NOH + OH} &\rightleftarrows \mathrm{NO + H_2O} \\
\mathrm{H_2NO + O} &\rightleftarrows \mathrm{H_2NO_2} \\
\mathrm{H_2NO + H} &\rightleftarrows \mathrm{H_3NO} \\
\mathrm{H_3NO + O} &\rightleftarrows \mathrm{H_2NO + OH} \\
\mathrm{H_3NO + OH} &\rightleftarrows \mathrm{H_2NO + H_2O}
\end{aligned}$$

Lateral interactions:

$$\mathrm{Adsorbate_x} \rightleftarrows \mathrm{Adsorbate_x} \tag{4.2}$$

$$\mathrm{Adsorbate_x} \rightleftarrows \mathrm{Adsorbate_y} \tag{4.3}$$

D Minimum energy pathway calculations

The minimum energy pathways (MEPs) of the events as they were discussed in the main part of this work were evaluated/ approximated with the nudged elastic band (NEB) and the drag method, respectively[32]. The MEPs as well as the geometries of the initial states (IS), transition state (TS – in case a maximum on the potential energy surface was found) and final states (FS – if not identical with the IS) are shown below.

---

[32] The energy diagrams based on NEB calculations exhibit smooth curves, while the energy diagrams evaluated with the drag method exhibit rigid lines

$NH_3 + O \rightleftarrows NH_2 + OH$:

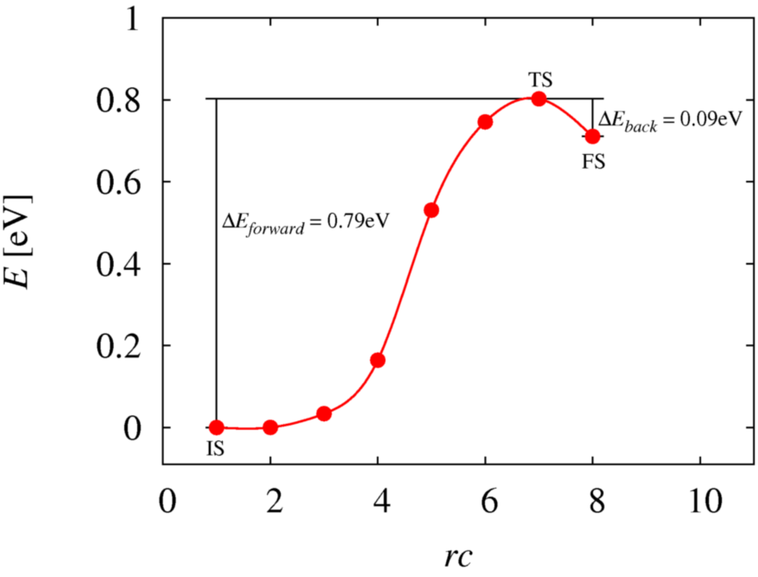

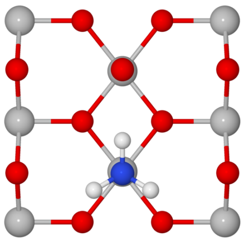

IS

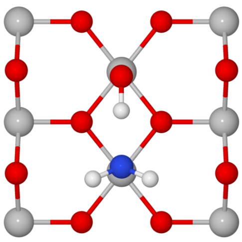

TS

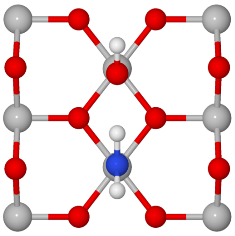

FS

$NH_2 + O \rightleftarrows NH + OH$:

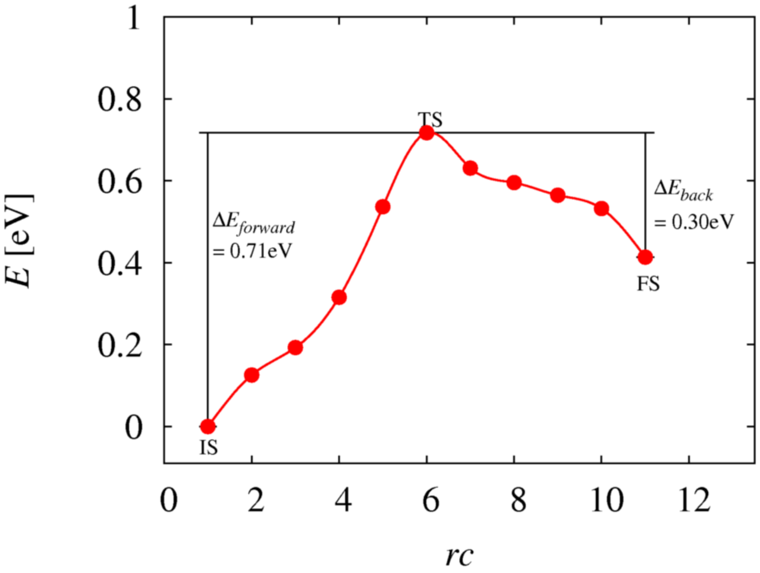

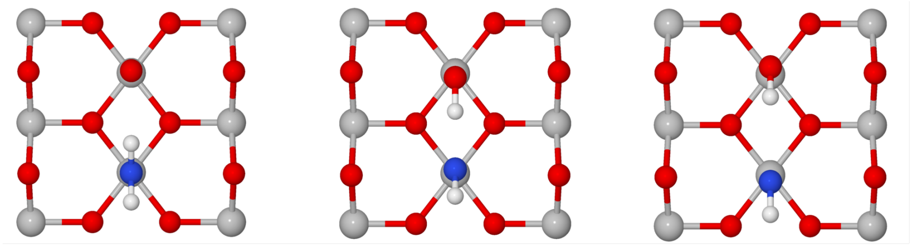

IS TS FS

$NH + O \rightleftarrows N + OH$:

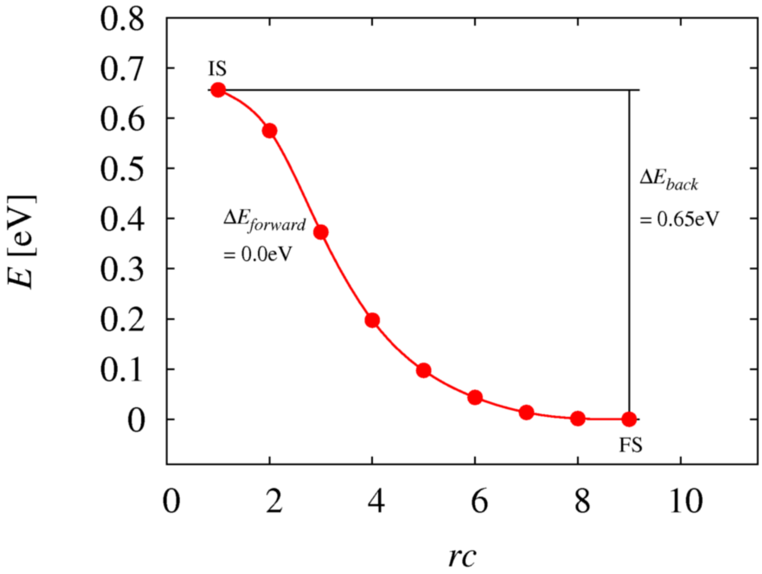

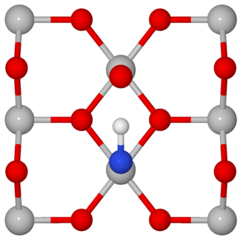

IS

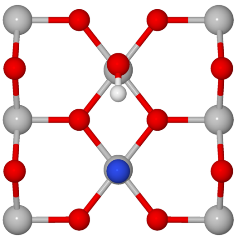

FS

$NH_2 + OH \rightleftarrows NH + H_2O$:

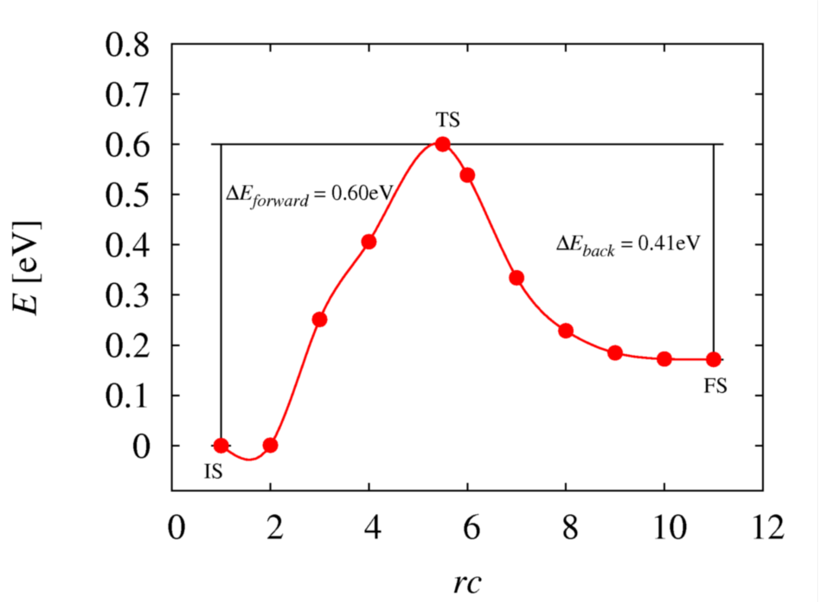

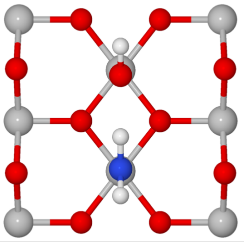

IS

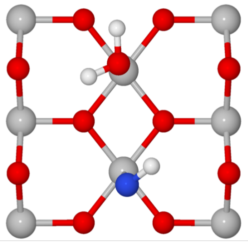

TS

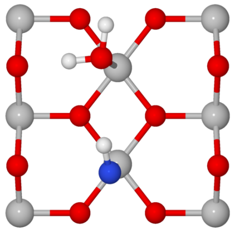

FS

$NH + OH \rightleftarrows N + H_2O$:

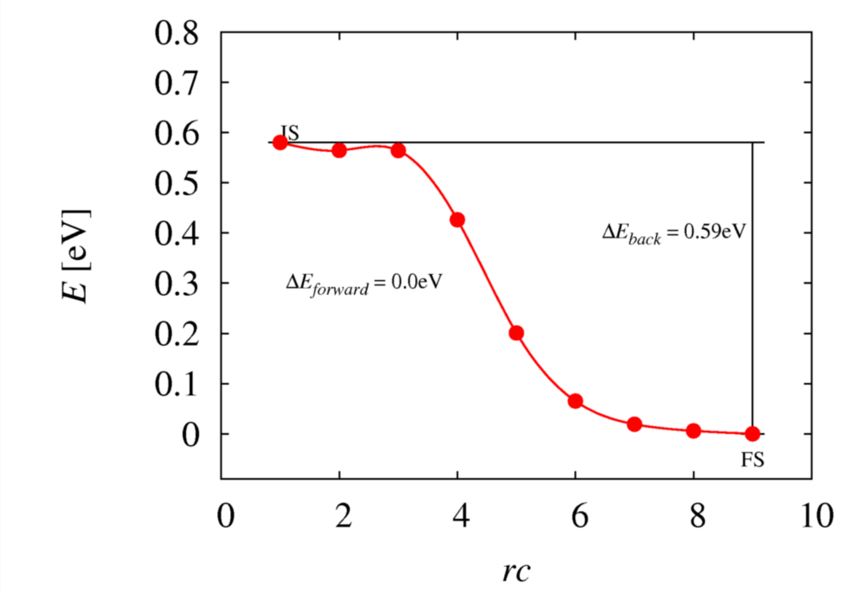

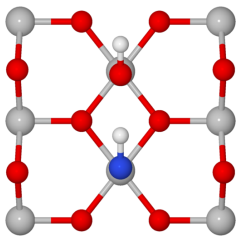

IS

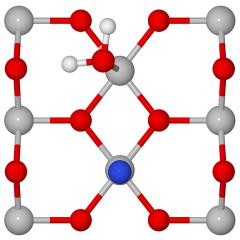

FS

N + O $\rightleftarrows$ NO:

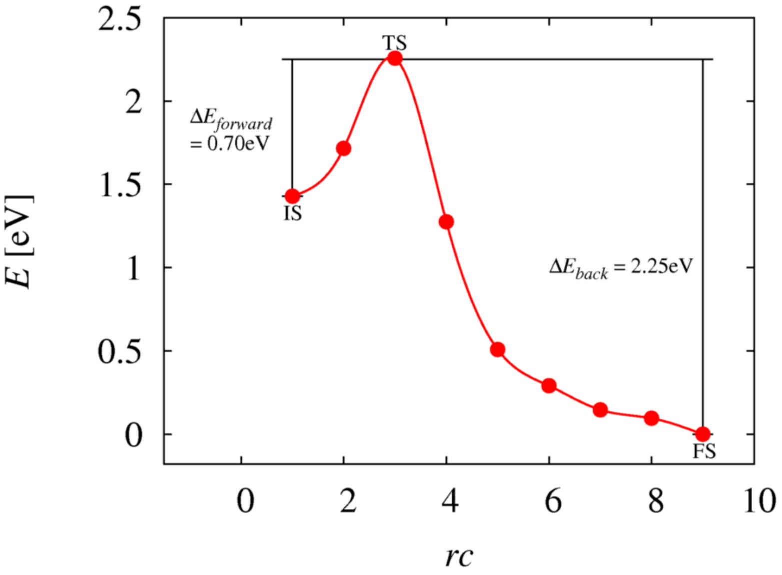

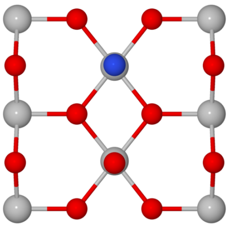

IS

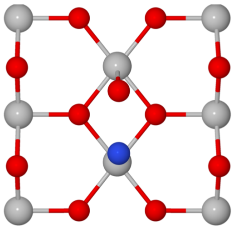

TS

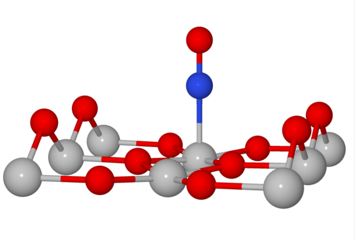

FS

$\mathbf{N} + \mathbf{N} \rightleftarrows \mathbf{N}_2$:

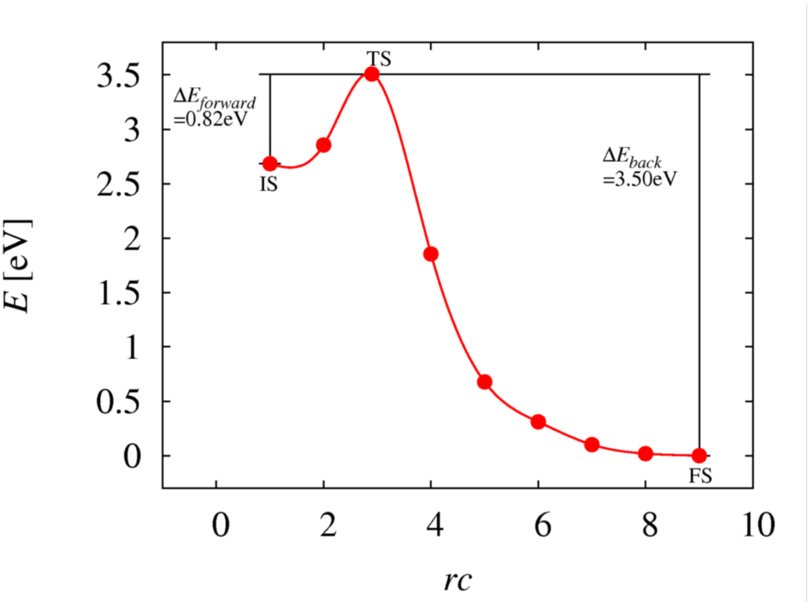

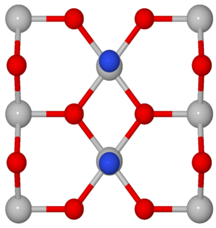

IS

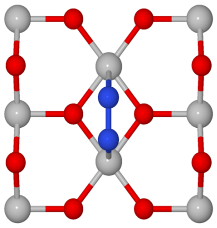

TS

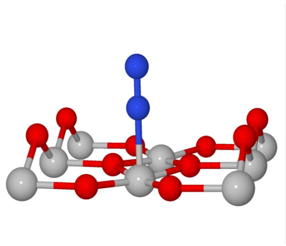

FS

$NH \rightleftarrows N + H$:

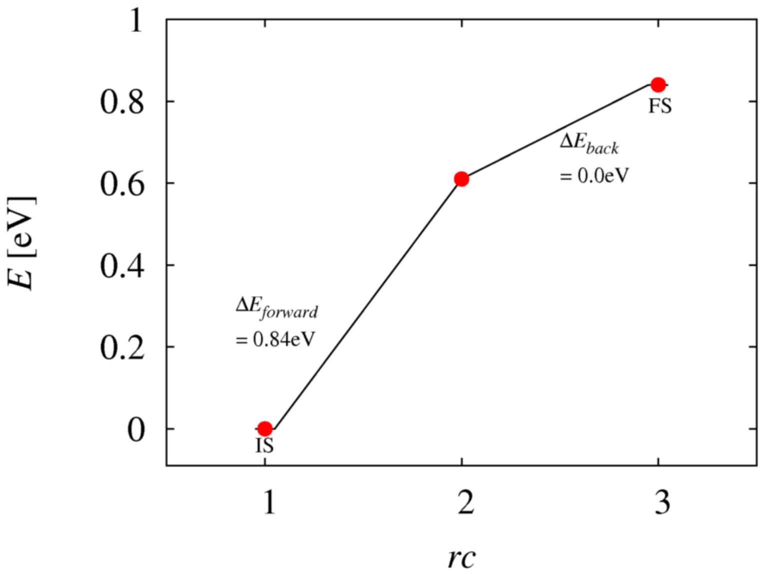

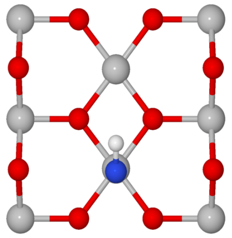

IS

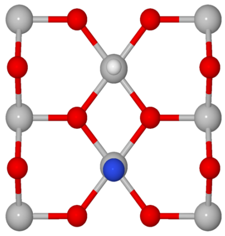

FS

$NO + N \rightleftarrows N_2O$:

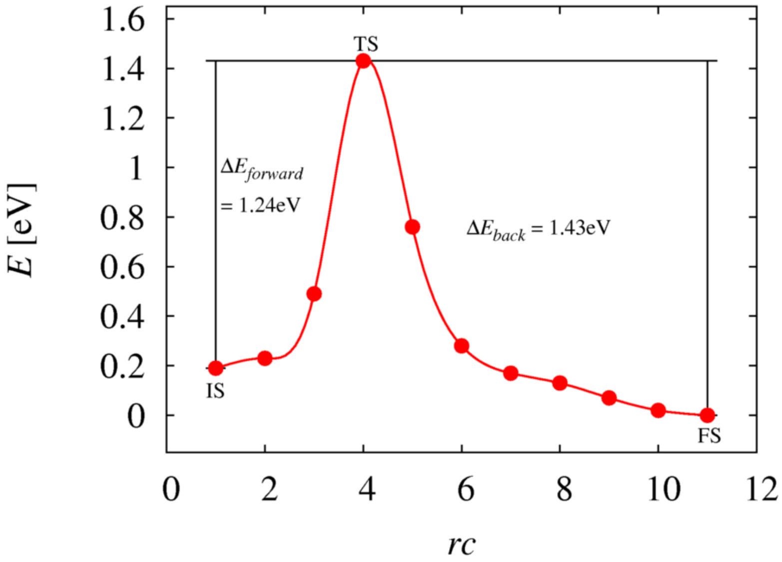

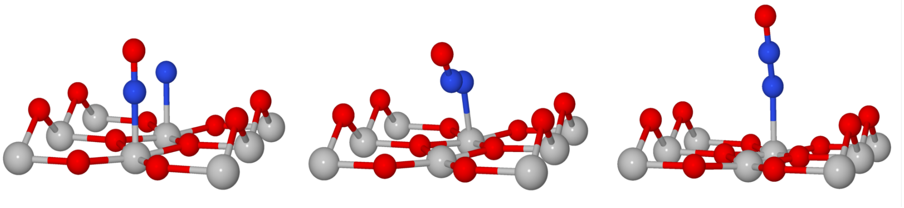

IS TS FS

$N_2O \rightleftarrows N_2 + O$:

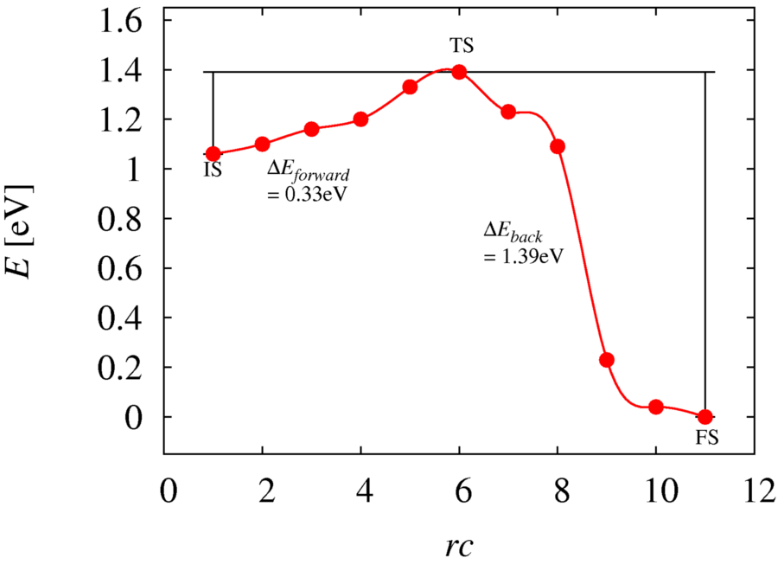

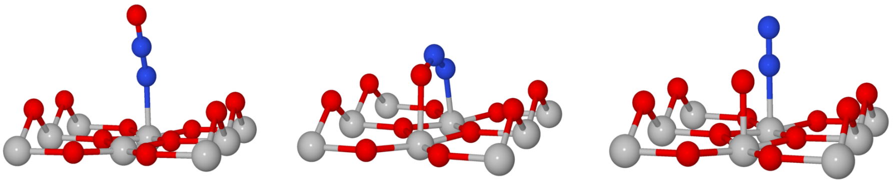

$\mathbf{NO + N \rightleftarrows N_2O_{flat}}$:

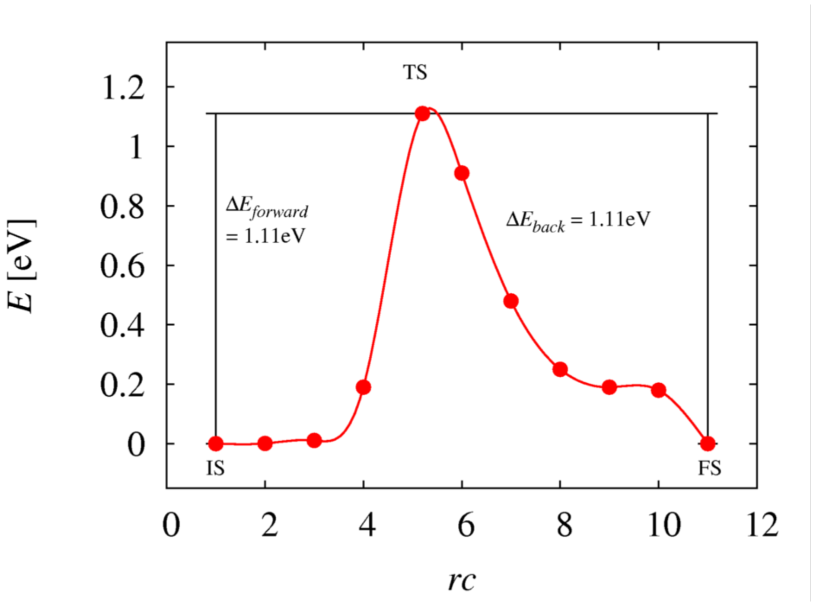

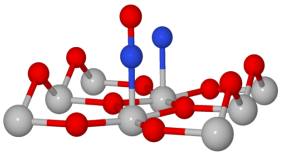

IS

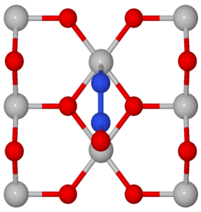

TS

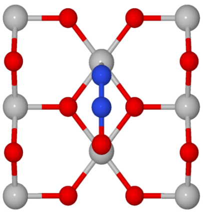

FS

$N_2O_{flat} \rightleftarrows N_2 + O$:

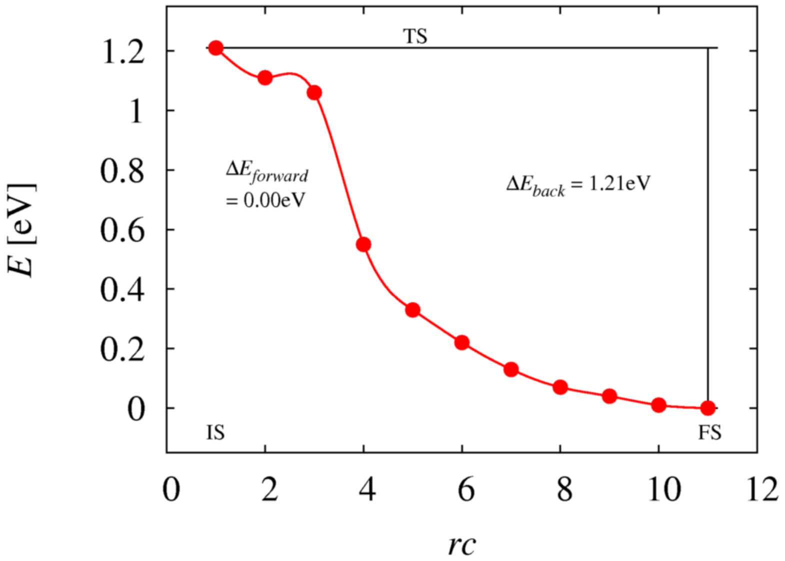

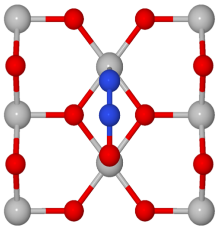

IS

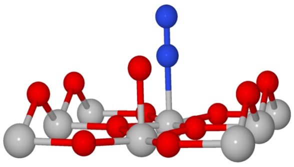

FS

$N_2O_{\mathbf{flat}} \rightleftarrows N_2O_{\mathbf{up}}$:

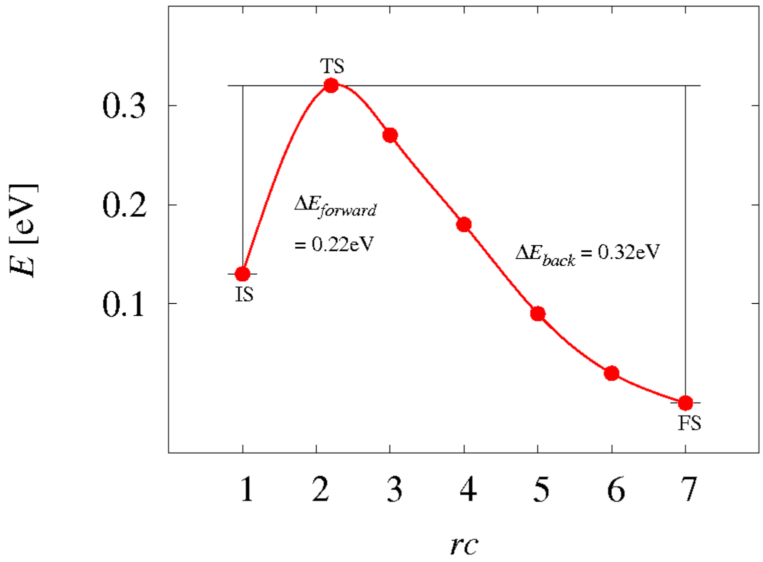

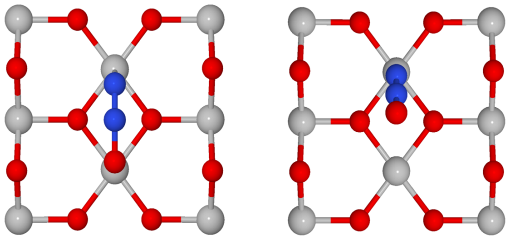

IS FS

$\mathbf{O + N \rightleftarrows ON}$:

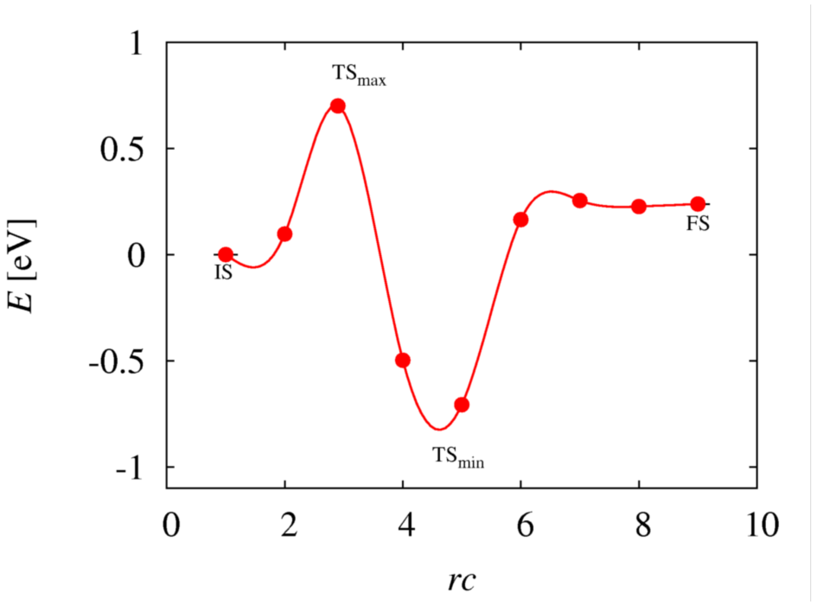

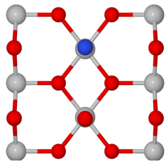

IS

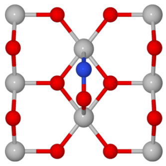

$\mathrm{TS}_{\mathrm{max}}$

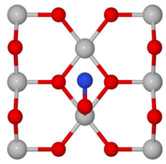

$\mathrm{TS}_{\mathrm{min}}$

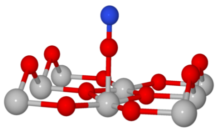

FS

N + O $\rightleftarrows$ NO(g):

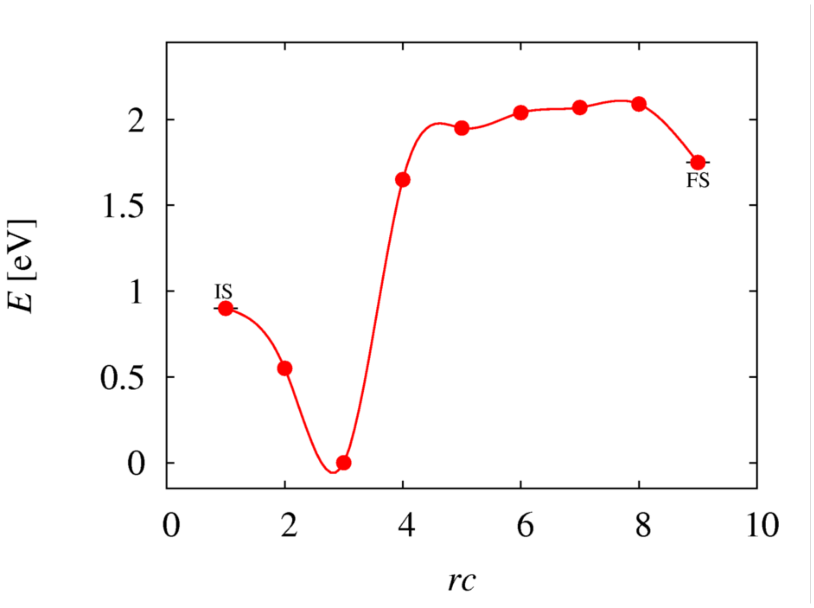

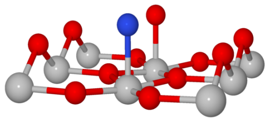

IS

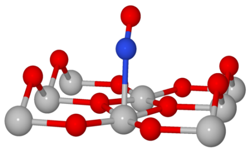

TS

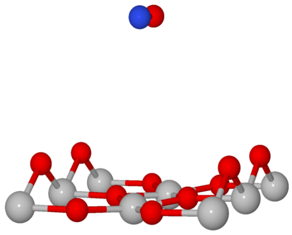

FS

$\mathbf{NO}_{cus_1} \rightleftarrows \mathbf{ON}_{cus_2}$:

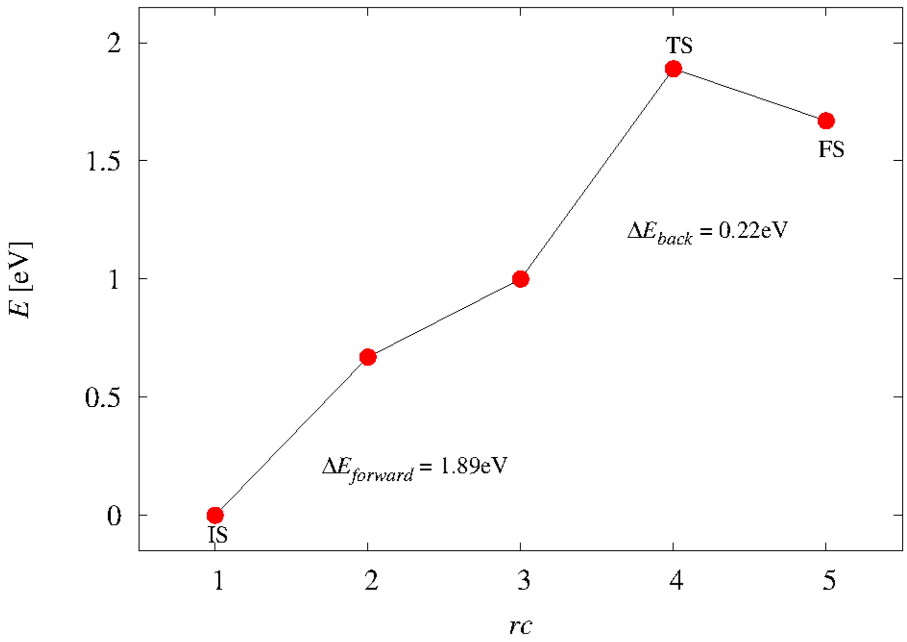

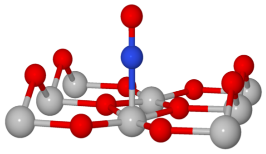

IS

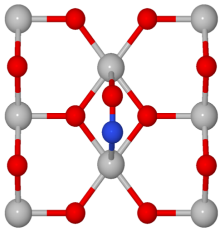

TS

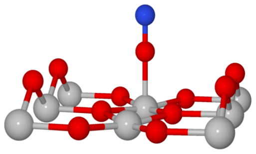

FS

$\mathbf{NO}_{cus_1} \rightleftarrows \mathbf{ON}_{cus_1}$:

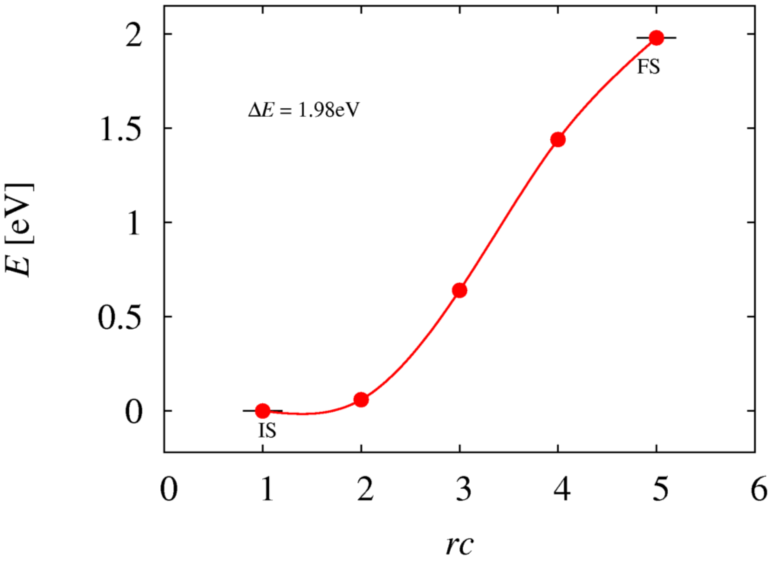

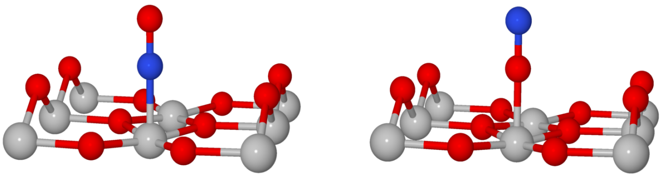

$\mathbf{NO}_{cus} \rightleftarrows \mathbf{NO}_{br}$:

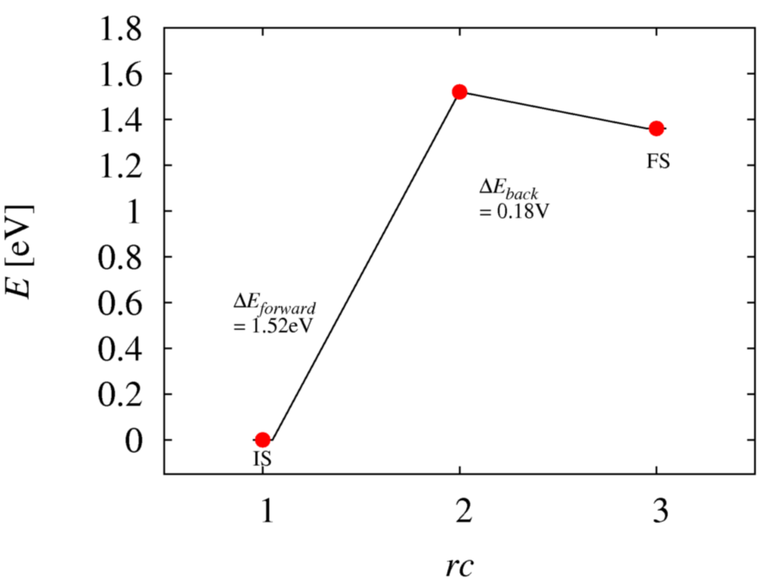

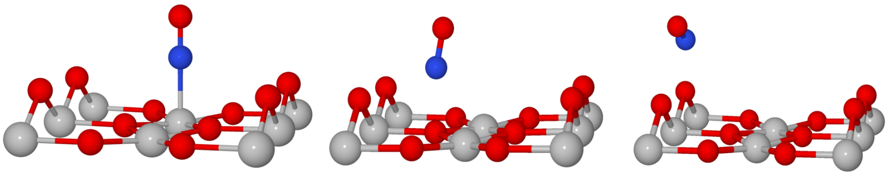

IS TS FS

Diffusion N

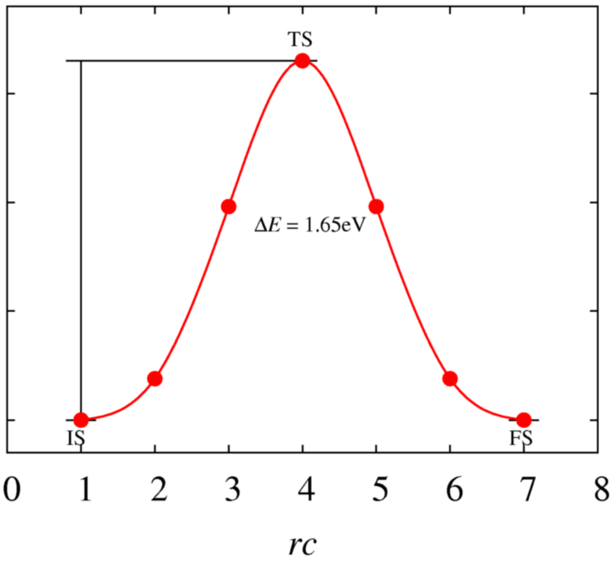

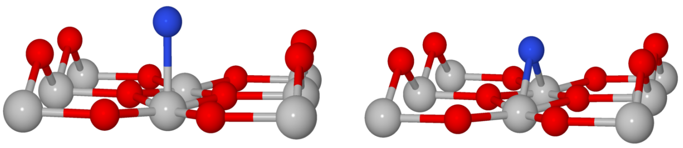

IS TS

Diffusion O

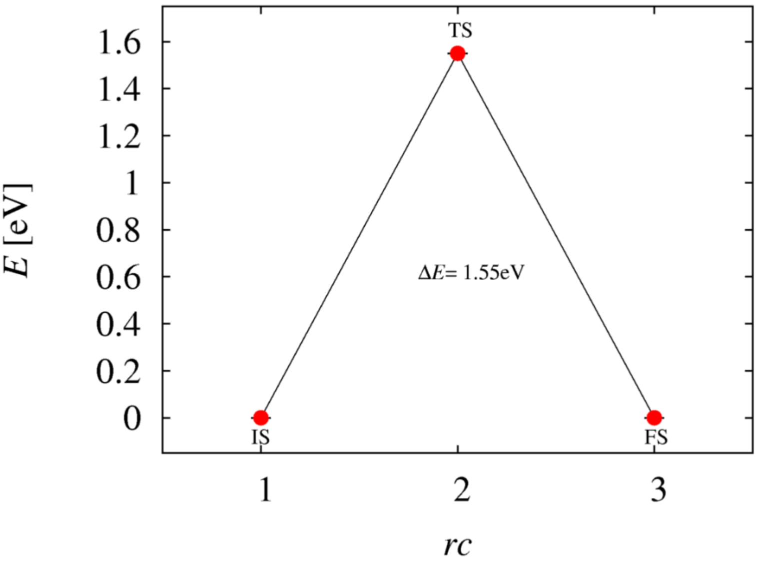

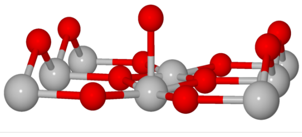

IS

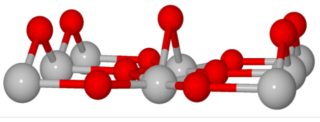

TS

Diffusion NO

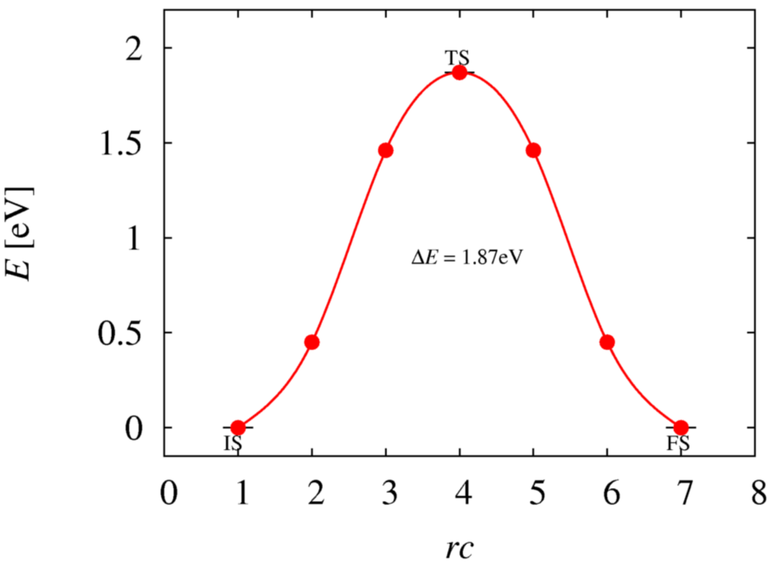

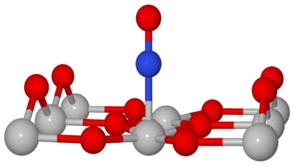

IS

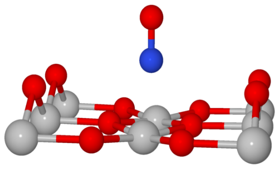

TS

Diffusion NH_3

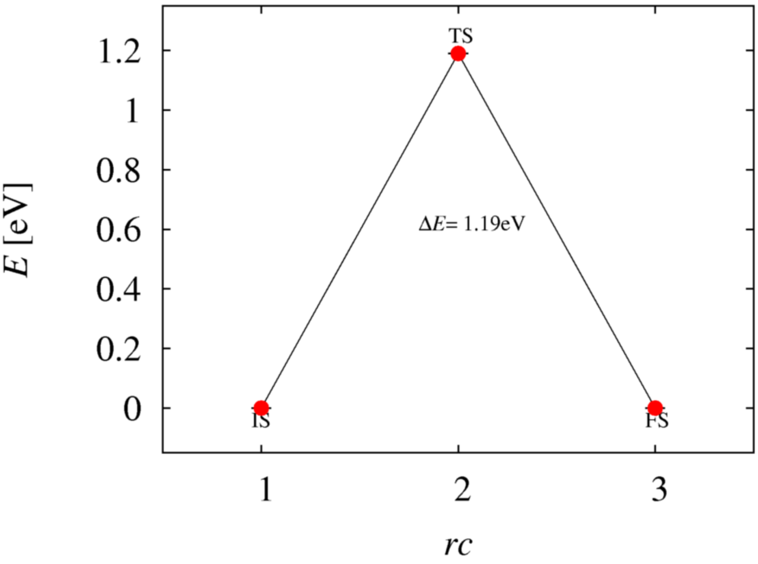

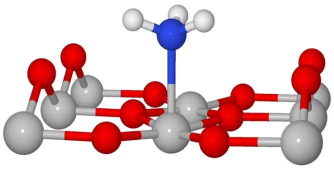

IS

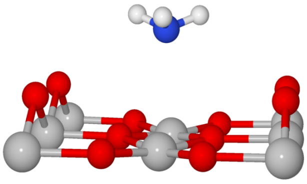

TS

Diffusion NH_2

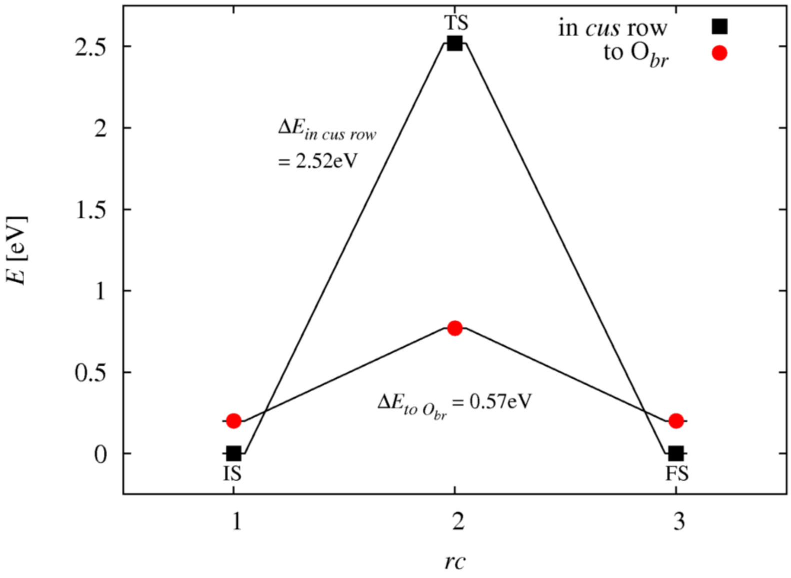

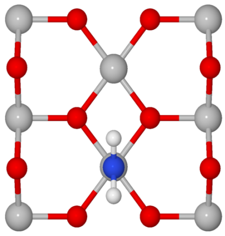

IS

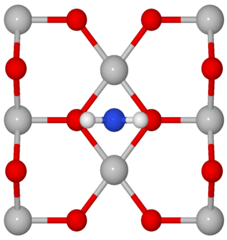

TS

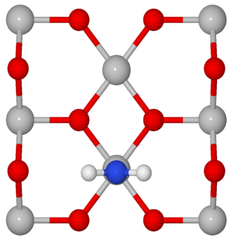

IS

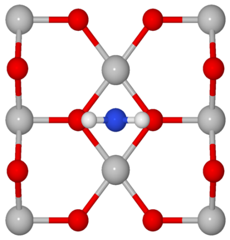

TS

Rotation $\mathbf{NH_{2,\text{in row}} \rightleftarrows NH_{2,\text{to } O_{br}}}$

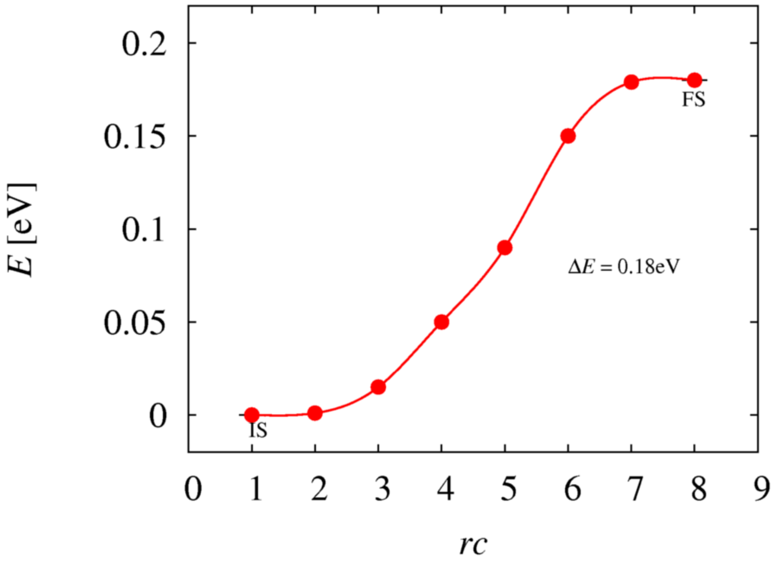

Diffusion NH

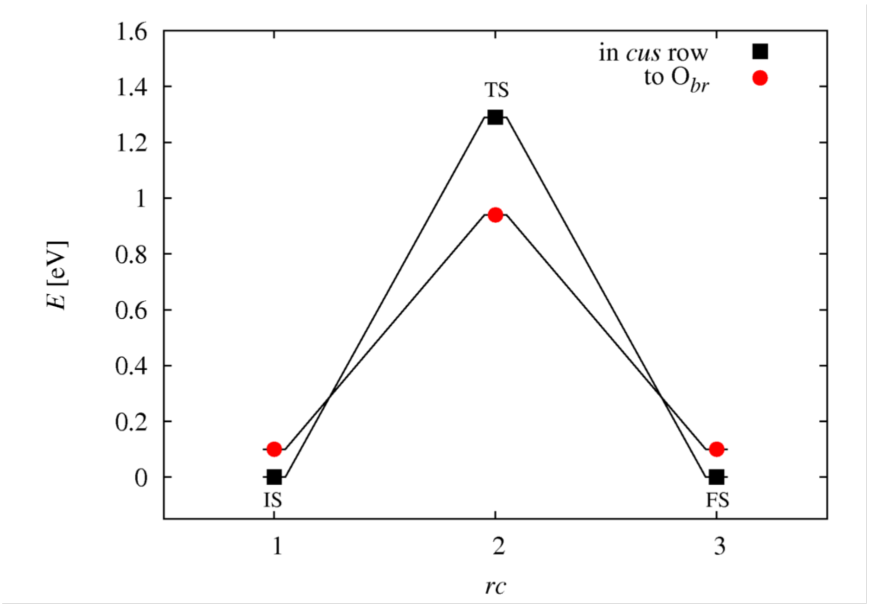

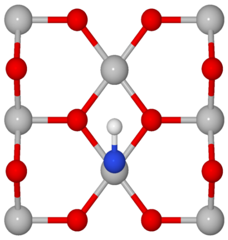

IS

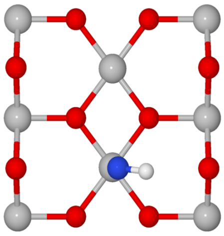

IS

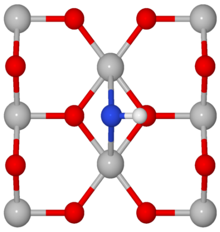

TS

Rotation $\mathbf{NH_{in\ row} \rightleftarrows NH_{to\ O_{br}}}$

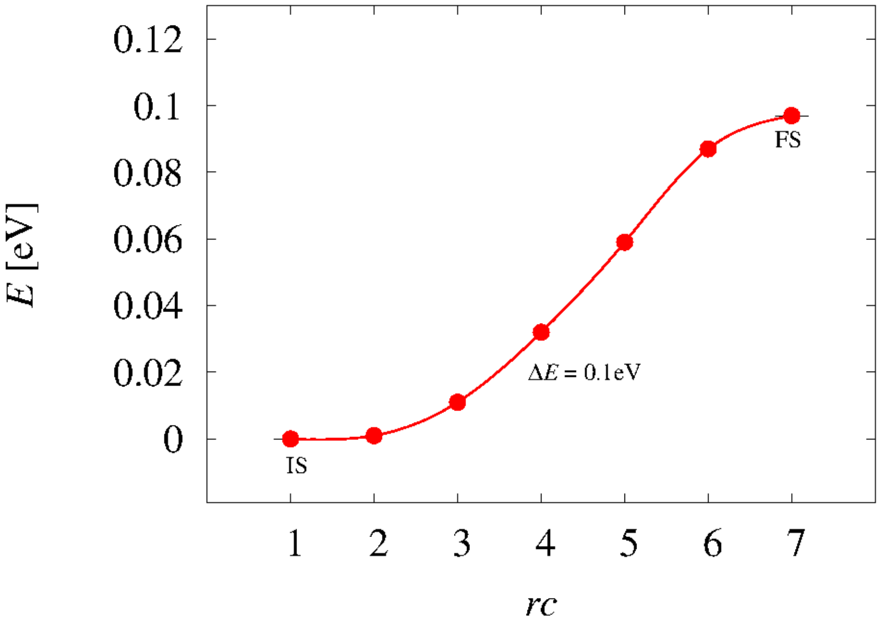

Diffusion OH

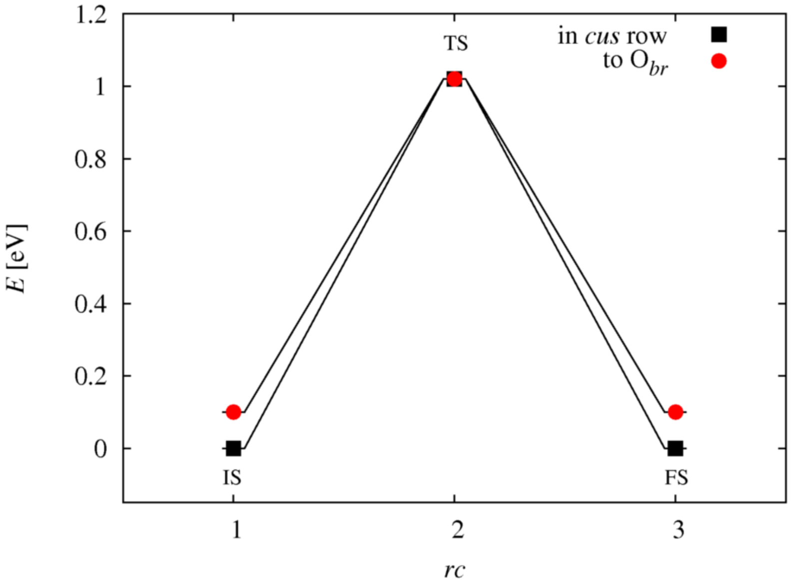

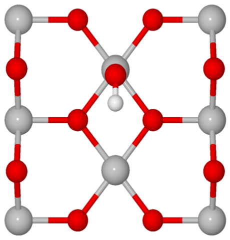

IS

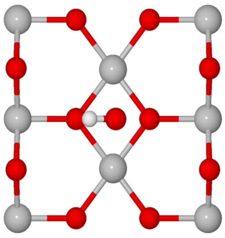

TS

Diffusion H_2O

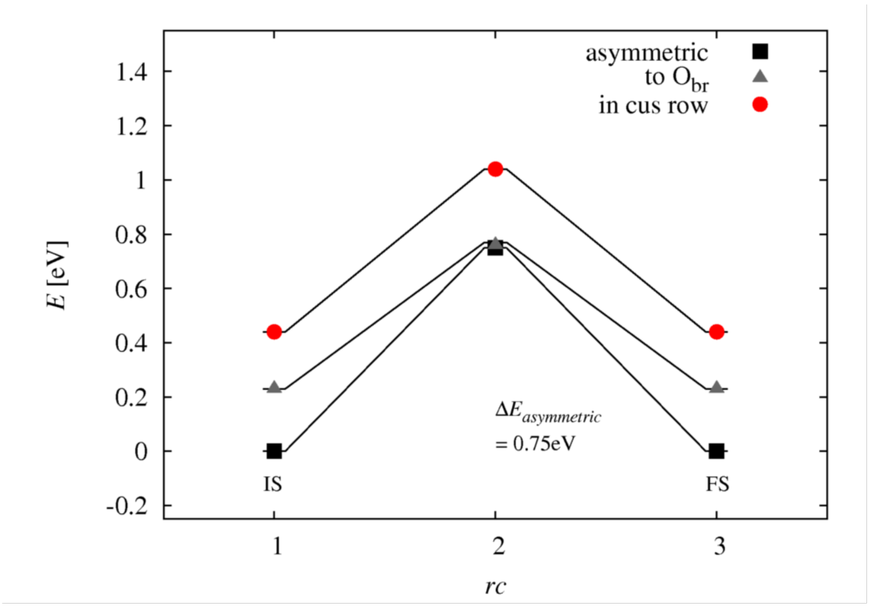

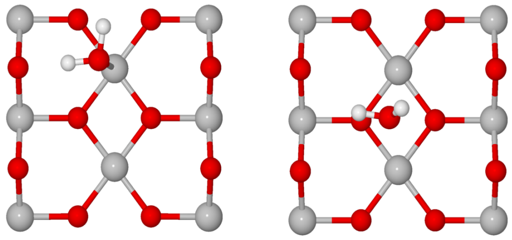
IS TS

Diffusion N_2O

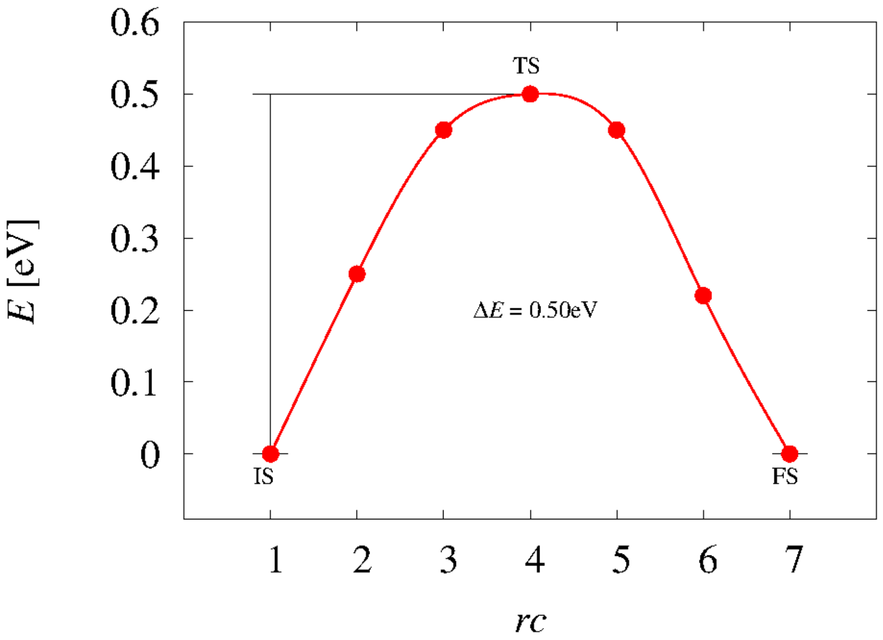

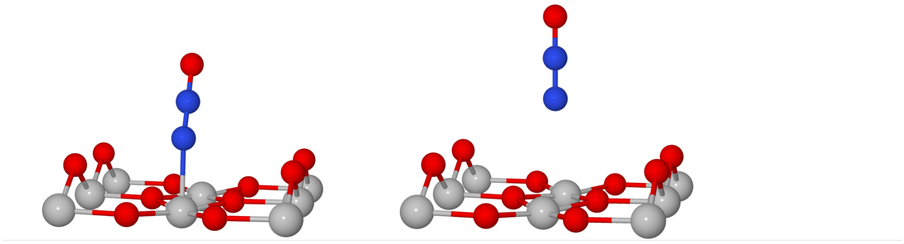

IS TS

$\mathbf{NH_2 + NH \rightleftarrows NH + NH_2}$

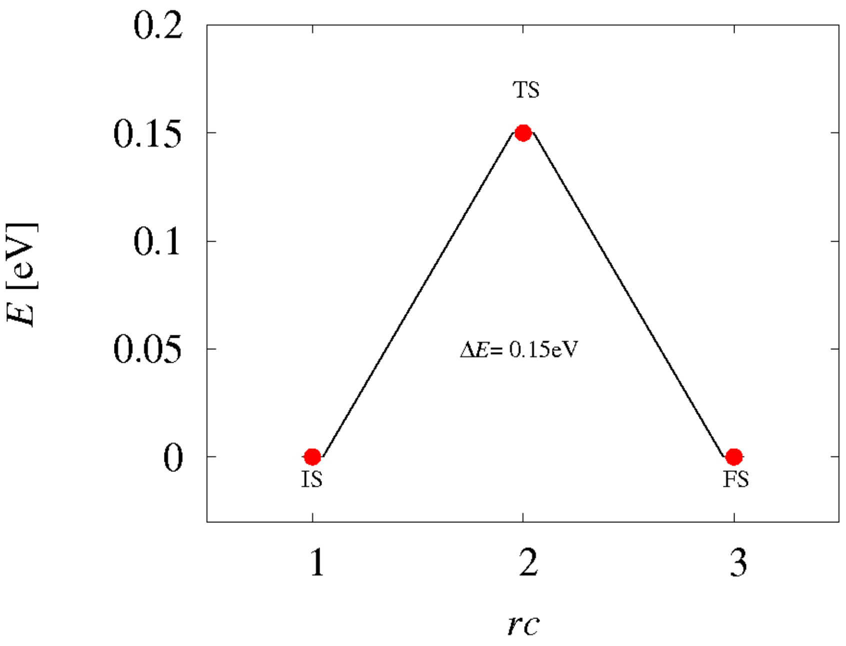

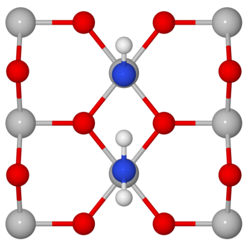

IS

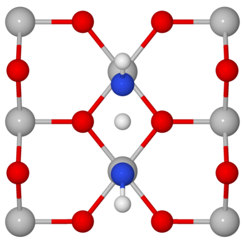

TS

$NH_2 + N \rightleftarrows NH + NH$

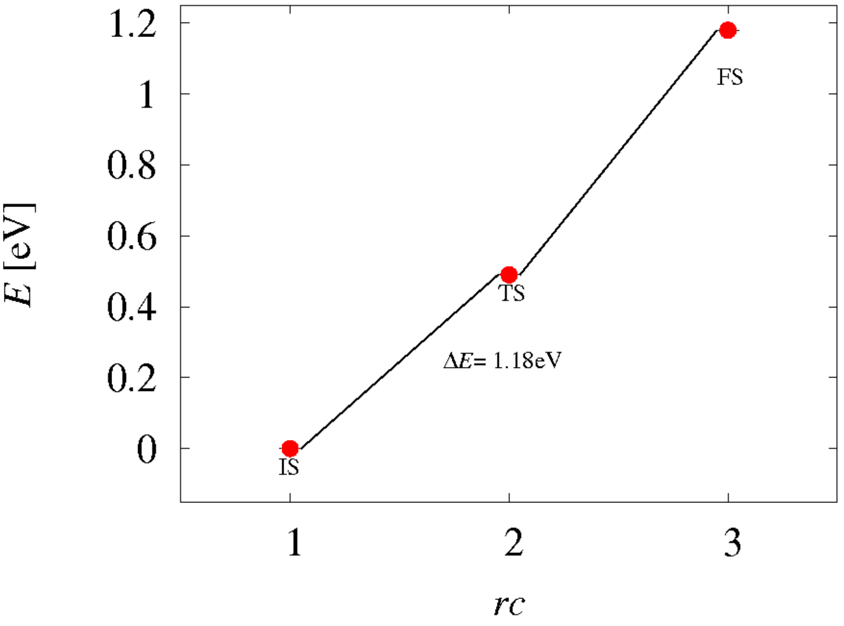

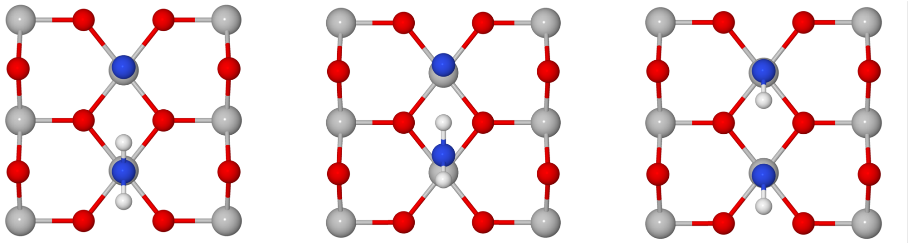

IS TS FS

$\mathbf{NH_3 + NH_2 \rightleftarrows NH_2 + NH_3}$

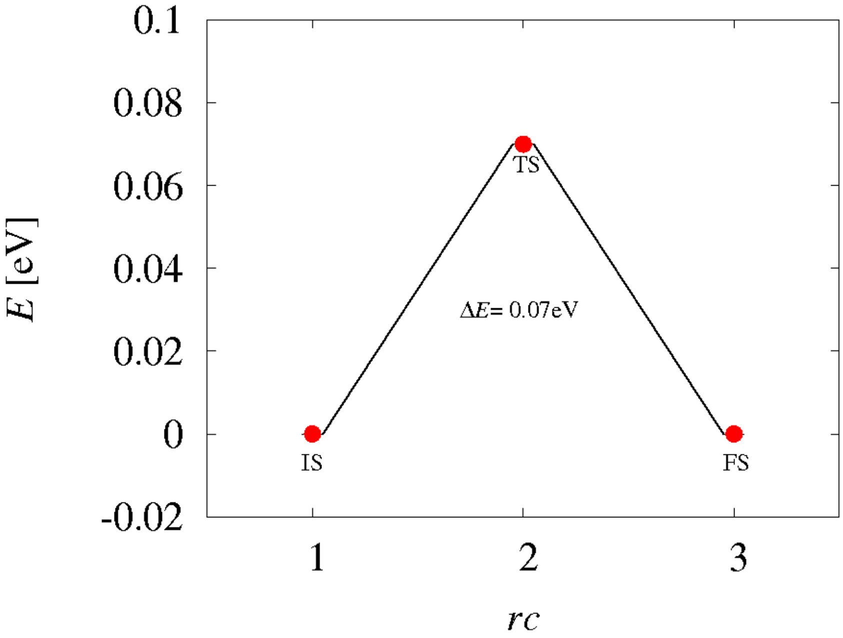

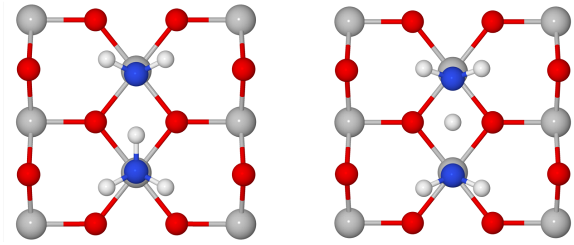

IS TS

$\mathbf{NH_3 + NH \rightleftarrows NH_2 + NH_2}$

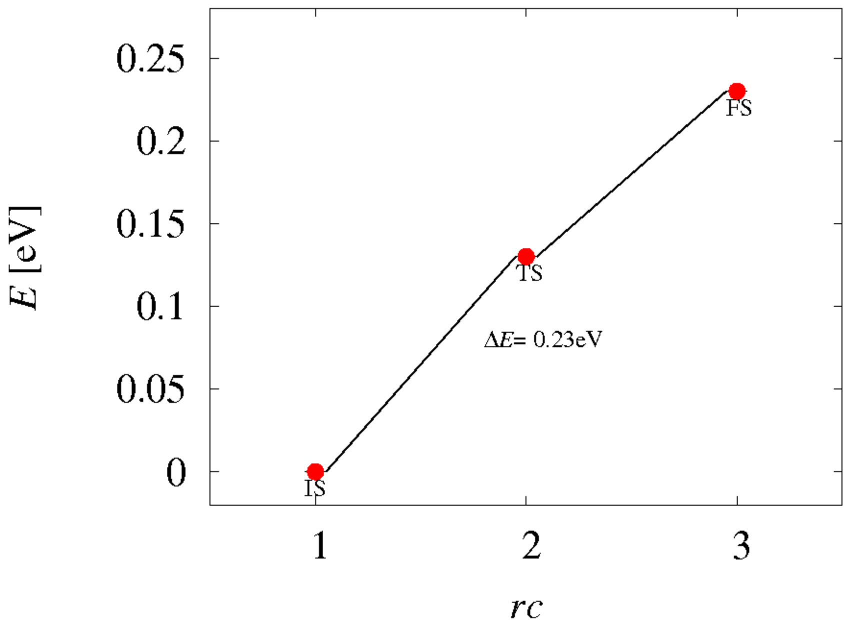

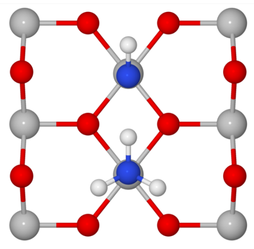

IS

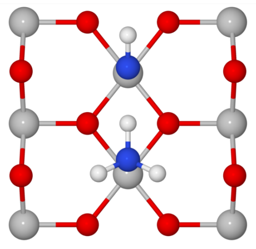

TS

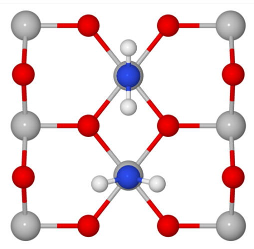

FS

NH + N $\rightleftarrows$ N + NH

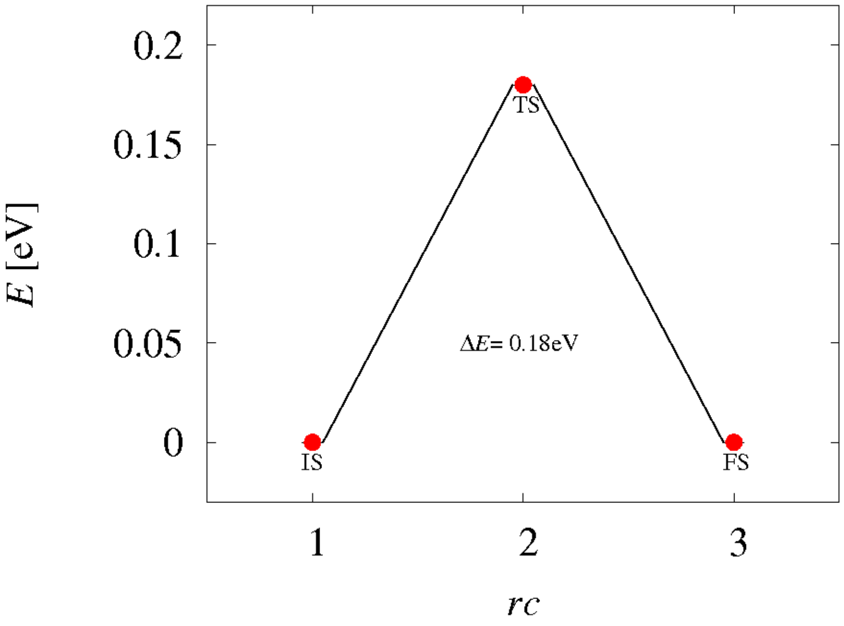

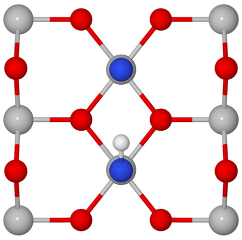

IS

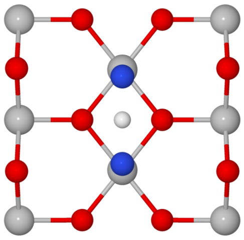

TS

E Acronyms

BFGS	Broyden, Flechter, Goldfarb, Shanno
BO	Born-Oppenheimer
BZ	Brillouin zone
br	bridge site
cus	coordinatively unsaturated site
DFT	Density functional theory
DOS	Density of states
EOS	Equation of states
ϵ_F	Fermi energy
FP	Full potential
FS	Final state
GGA	Generalized gradient approximation
HF	Hartree-Fock
HREELS	High resolution electron energy loss spectroscopy
hTST	Harmonic transition state theory
IS	Initial state
kMC	Kinetic Monte Carlo
KS	Kohn-Sham
LDA	Local density approximation
LEED	Low energy electron diffraction
MEP	Minimum energy pathway
ML	Mono layer
MP	Monkhorst Pack
ncl	non-classical
NEB	Nudged elastic band
PBE	Exchange correlation functional by Perdew, Burke and Enzerhof
PES	Potential energy surface
PP	Pseudopotential
QMC	Quantum Monte Carlo
rc	Reaction coordinate
RPBE	Revised PBE
TD-DFT	Time dependent density functional theory
TDS	Thermal desorption spectroscopy
TF	Thomas Fermi
TOF	Turnover frequency
TS	Transition state
UHV	Ultra high vacuum

XC	Exchange-correlation
XRD	X-Ray diffraction
ZPE	Zero point energy

F Curriculum vitae

For reasons of data protection,
the curriculum vitae is not included in the online version

G Acknowledgements

I appreciate the help I obtained from so many people during my time at the FHI:
First of all, I would like to thank my supervisor Prof. Dr. Karsten Reuter for giving me the opportunity to work on such a versatile and interesting topic. I am very grateful for his permanent support and especially for the many opportunities to get in contact with a lot of different people at conferences all over the world. Further I am very thankful for the opportunity to stay in Berlin until the end of my Ph.D.
Concerning this I would also like to thank Prof. Dr. Matthias Scheffler for giving me shelter in his department even though the Reuter group moved to TU Munich.
A special thanks goes to my office mate Norina Richter for brightening every single working day.
I also want to thank Jörg Meyer, who helped me especially in the beginning of my Ph.D., for being incredibly patient and helpful in any technical or professional issue.
Further people also contributed to my work: Many thanks to Nico Brademann for carefully proofreading my thesis, Karolina Kwapien for the motivation during these hard days and Thorben Winzer for solving this particularly nasty gnuplot-problem.
Besides this I would like to thank all my colleagues: the past colleagues of the Junior Research Group in Berlin as well as the members of the new group at TU Munich and all past and present members of the Theory Department of the FHI in Berlin.
Additionally, I would like to thank Professor Martin Weinelt for taking his time to be my second supervisor. For the permanent support I would also like to thank the secretaries and the system administrator.
Finally, my biggest thanks goes to my family and friends for their permanent support.

H Publications, poster, talks

Poster

- International Conference on Theoretical Aspects of Catalysis (ICTAC), Matsushima, Japan, June 2010
- Psi-*k* conference, Berlin, Germany, September 2010
- Catalysis from first principles (Cat1P), Copenhagen, Denmark, May 2011

Talks

- DPG Frühjahrstagung, Regensburg, Germany, March 2010
- European Conference on Surface Crystallography and Dynamics (ECSCD), Reading, UK, September 2010
- DPG Frühjahrstagung, Dresden, Germany, March 2011

Eidesstattliche Versicherung

Ich versichere hiermit, alle Hilfsmittel und Hilfen angegeben und die Arbeit auf dieser Grundlage selbstständig verfasst zu haben. Die Arbeit ist weder in einem früheren Promotionsverfahren angenommen noch als ungenügend beurteilt worden.

Bibliography

[1] Wang, Y., Jacobi, K., Schoene, W.-D., and Ertl, G., J. Phys. Chem. **109** (2005) 7883.

[2] Wang, Y., Jacobi, K., and Ertl, G., The Journal of Physical Chemistry B **107** (2003) 13918.

[3] Ertl, G., Angew. Chem., Int. Ed **47** (2008) 3524.

[4] Reuter, K. and Scheffler, M., Physical Review B **73** (2006) 045433.

[5] Rogal, J., *Stability, composition and function of palladium surfaces in oxidizing environments: A first-principles statistical mechanics approach*, PhD thesis, Freie Universität Berlin, 2006.

[6] Over, H. and Muhler, M., Progress in surface science **72** (2003) 3.

[7] Kim, M. et al., Science **292** (2001) 1357.

[8] Salo, P., Honkala, K., Alatalo, M., and Laasonen, K., Surface science **516** (2002) 247.

[9] Ge, Q. and Neurock, M., The Journal of Physical Chemistry B **110** (2006) 15368.

[10] Hammer, B., Morikawa, Y., and Nørskov, J., Physical review letters **76** (1996) 2141.

[11] Satterfield, C., *Heterogeneous catalysis in industrial practice*, New York, NY (United States); McGraw Hill Book Co., 1991.

[12] Second, C., Ertl, G., Knoezinger, H., Schueth, F., and Weitkamp, J., Environmental Engineering and Management Journal **7** (2008) 641.

[13] Kuhlmann, F., Annalen der Pharmacie **29** (1839) 272.

[14] Perez-Ramirez, J., Lopez, N., and Kondratenko, E., J. Phys. Chem. C **114** (2010) 16660.

[15] Seitsonen, A. et al., Surface Science **603** (2009) L113.

[16] Carabineiro, S. and Nieuwenhuys, B., Surface science **532** (2003) 87.

[17] Gootzen, J., Wonders, A., Visscher, W., Van Santen, R., and Van Veen, J., Electrochimica acta **43** (1998) 1851.

[18] Bradley, J., Hopkinson, A., and King, D., The Journal of Physical Chemistry **99** (1995) 17032.

[19] Asscher, M., Guthrie, W., Lin, T., and Somorjai, G., The Journal of Physical Chemistry **88** (1984) 3233.

[20] Mieher, W. and Ho, W., Surface science **322** (1995) 151.

[21] Curtin, T., O'Regan, F., Deconinck, C., Knüttle, N., and Hodnett, B., Catalysis today **55** (2000) 189.

[22] Hansgen, D., Vlachos, D., and Chen, J., Nature Chemistry **2** (2010) 484.

[23] Wang, C.-C., Yang, Y.-J., and Jiang, J.-C., J. Phys. Chem. C **113** (2009) 21976.

[24] Wang, C.-C., Yang, Y.-J., Jiang, J.-C., Tsai, D.-S., and Hsieh, H.-M., J. Phys. Chem. C **113** (2009) 17411.

[25] Hong, S., Karim, A., Rahman, T. S., Jacobi, K., and Ertl, G., Journal of catalysis (2010).

[26] Gerischer, H. and Mauerer, A., Journal of Electroanalytical Chemistry and Interfacial Electrochemistry **25** (1970) 421.

[27] Van den Broek, A., Van Grondelle, J., and Van Santen, R., Journal of Catalysis **185** (1999) 297.

[28] Perez-Ramirez, J., Kapteijn, F., Schöffel, K., and Moulijn, J., Appl. Catal. B: Environ **44** (2003) 117.

[29] Burch, R., Daniells, S., and Hu, P., The Journal of Chemical Physics **121** (2004) 2737.

[30] Wang, H. and Schneider, W., Catalysis Today (2010).

[31] Hong, S., Rahman, T., Jacobi, K., and Ertl, G., The Journal of Physical Chemistry C **111** (2007) 12361.

[32] Brown, W. and King, D., The Journal of Physical Chemistry B **104** (2000) 2578.

[33] Jacobi, K. and Wang, Y., Surface Science **603** (2009) 1600.

[34] Kim, M., Pratt, S., and King, D., Journal of the American Chemical Society **122** (2000) 2409.

[35] Over, H. et al., Science **287** (2000) 1474.

[36] Reuter, K., Stampfl, C., and Scheffler, M., *Ab initio atomistic thermodynamics and statistical mechanics of surface properties and functions, Part A Methods*, Springer Berlin, 2005.

[37] Nieminen, R., Journal of Physics: Condensed Matter **14** (2002) 2859.

[38] Vineyard, G., Journal of Physics and Chemistry of Solids **3** (1957) 121.

[39] Haenggi, P., Talkner, P., and Borkovec, M., Rev. Mod. Phys. **62** (1990) 251.

[40] Reuter, K., Frenkel, D., and Scheffler, M., Physical review letters **93** (2004) 116105.

[41] Kaxiras, E., Bar-Yam, Y., Joannopoulos, J., and Pandey, K., Physical Review B **35** (1987) 9625.

[42] Scheffler, M. and Dabrowski, J., Philosophical Magazine A **58** (1988) 107.

[43] Scheffler, M., *Physics of Solid Surfaces*, Elsevier, 1988.

[44] Qian, G., Martin, R., and Chadi, D., Physical Review B **38** (1988) 7649.

[45] Kohanoff, J., *Electronic structure calculations for solids and molecules: theory and computational methods*, Cambridge Univ Pr, 2006.

[46] Martin, R., *Electronic structure: basic theory and practical methods*, Cambridge Univ Pr, 2004.

[47] Parr, R. and Yang, W., The density-functional theory of atoms and molecules, volume 16 of the international series of monographs on chemistry, 1989.

[48] Jensen, F., *Computational chemistry*, Wiley, 1999.

[49] Hartree, D., The wave mechanics of an atom with a non-Coulomb central field. Part I. Theory and methods, in *Mathematical Proceedings of the Cambridge Philosophical Society*, volume 24, pages 89–110, Cambridge Univ Press, 1928.

[50] Thomas, L., The calculation of atomic fields, in *Mathematical Proceedings of the Cambridge Philosophical Society*, volume 23, pages 542–548, Cambridge Univ Press, 1927.

[51] Fermi, E., Zeitschrift für Physik A Hadrons and Nuclei **48** (1928) 73.

[52] Born, M. and Oppenheimer, J., Ann. Physik **84** (1927) 457.

[53] Dirac, P., Note on exchange phenomena in the Thomas atom, in *Mathematical Proceedings of the Cambridge Philosophical Society*, volume 26, pages 376–385, Cambridge Univ Press, 1930.

[54] Hohenberg, P. et al., Physical Review **136** (1964) B864.

[55] Kohn, W. et al., Physical Review **140** (1965) A1133.

[56] Ceperley, D. and Alder, B., Physical Review Letters **45** (1980) 566.

[57] Jones, R. and Gunnarsson, O., Reviews of Modern Physics **61** (1989) 689.

[58] Hammer, B., Hansen, L., and Nørskov, J., Physical Review B **59** (1999) 7413.

[59] Shang-Keng, M. and Brueckner, K., Physical Review **165** (1968) 18.

[60] Perdew, J., Ziesche, P., and Eschrig, H., Akademie-Verlag, Berlin (1991) 11.

[61] Perdew, J. and Wang, Y., Physical Review B **45** (1992) 13244.

[62] Zhang, Y. and Yang, W., Physical Review Letters **80** (1998) 890.

[63] Lieb, E. and Oxford, S., The Stability of Matter: From Atoms to Stars (2005) 65.

[64] Lieb, E., Physics Letters A **70** (1979) 444.

[65] Bloch, F., Zeitschrift für Physik **53** (1928) 555.

[66] Monkhorst, H. and Pack, J., Physical Review B **13** (1976) 5188.

[67] Chadi, D. and Cohen, M., Physical Review B **8** (1973) 5747.

[68] Gilat, G. and Bharatiya, N., Physical Review B **12** (1975) 3479.

[69] Blochl, P., Jepsen, O., and Andersen, O., Rev. B **49** (1994) 16223.

[70] Ho, K., Fu, C., Harmon, B., Weber, W., and Hamann, D., Physical Review Letters **49** (1982) 673.

[71] Fu, C. and Ho, K., Physical Review B **28** (1983) 5480.

[72] Marzari, N., *Ab-initio molecular dynamics for metallic systems*, PhD thesis, University of Cambridge, 1996.

[73] Phillips, J., Physical Review **112** (1958) 685.

[74] Heine, V., Solid state physics **24** (1970) 1.

[75] Cohen, M., Physica Scripta **1982** (1982) 5.

[76] Payne, M., Teter, M., Allan, D., Arias, T., and Joannopoulos, J., Reviews of Modern Physics **64** (1992) 1045.

[77] Meyer, B., *The pseudopotential plane wave approach*, volume 31, pages 71–83, NIC-Directors, Jülich, 2006.

[78] Hamann, D., Schlüter, M., and Chiang, C., Physical Review Letters **43** (1979) 1494.

[79] Starkloff, T. and Joannopoulos, J., Physical Review B **16** (1977) 5212.

[80] Vanderbilt, D., Physical Review B **41** (1990) 7892.

[81] Clark, S. et al., Zeitschrift für Kristallographie **220** (2005) 567.

[82] Hellmann, H., Acta Physicochimica URSS **2** (1936) 225.

[83] Feynman, R., Phys. Rev. **56** (1939) 340.

[84] Broyden, C., IMA Journal of Applied Mathematics **6** (1970) 222.

[85] Shanno, D. et al., Mathematics of computation **24** (1970) 647.

[86] Goldfarb, D., Mathematics of Computation **24** (1970) 23.

[87] Fletcher, R., The Computer Journal **13** (1970) 317.

[88] Fletcher, R. and Reeves, C., The computer journal **7** (1964) 149.

[89] Curry, H., Quart. Appl. Math **2** (1944) 250.

[90] Jónsson, H. et al., Classical and quantum dynamics in condensed phase simulations, 1998.

[91] Henkelman, G. and Jónsson, H., The Journal of Chemical Physics **113** (2000) 9978.

[92] Henkelman, G., Uberuaga, B., and Jónsson, H., The Journal of Chemical Physics **113** (2000) 9901.

[93] Bahn, S. and Jacobsen, K., Computing in Science & Engineering (2002) 56.

[94] Sheppard, D., Terrell, R., and Henkelman, G., The Journal of chemical physics **128** (2008) 134106.

[95] Henkelman, G., Jóhannesson, G., and Jónsson, H., Theoretical Methods in Condensed Phase Chemistry (2002) 269.

[96] Zangwill, A., *Physics at surfaces*, Cambridge Univ Pr, 1988.

[97] Reuter, K. and Scheffler, M., Physical Review B **68** (2003) 045407.

[98] Reuter, K. and Scheffler, M., Physical review letters **90** (2003) 046103.

[99] Wang, X. et al., Physical review letters **81** (1998) 1038.

[100] Wang, X., Chaka, A., and Scheffler, M., Phys. Rev. Lett **84** (2000) 3650.

[101] Reuter, K. and Scheffler, M., Phys. Rev. B **65** (2001) 035406.

[102] Wedler, G., *Lehrbuch der physikalischen Chemie*, volume 3, VcH, 1987.

[103] Rogal, J. and Reuter, K., *Ab initio atomistic thermodynamics for surfaces: A primer*, 2007.

[104] Eyring, H., J. Phys. Chem. **3** (1935).

[105] Frenkel, D. and Smit, B., *Understanding molecular simulation: from algorithms to applications*, Academic Pr, 2002.

[106] Chase, M., *NIST-JANAF thermochemical tables*, American Chemical Society (Washington, DC and Woodbury, NY), 1998.

[107] Reuter, K., *First-principles kinetic Monte Carlo simulations for heterogeneous catalysis: Application to the CO oxidation at RuO2(110)*, O. Deutschmann, 2009.

[108] Voter, A., *Introduction to the kinetic Monte Carlo method*, Springer, 2007.

[109] Jansen, A., Arxiv preprint cond-mat/0303028 (2003).

[110] Bortz, A., Kalos, M., and Lebowitz, J., Journal of Computational Physics **17** (1975) 10.

[111] Gillespie, D., Journal of computational physics **22** (1976) 403.

[112] Fichthorn, K. and Weinberg, W., The Journal of chemical physics **95** (1991) 1090.

[113] Chatterjee, A. and Vlachos, D., Journal of computer-aided materials design **14** (2007) 253.

[114] Redhead, P., Vacuum **12** (1962) 203.

[115] Vollhardt, K. and Shore, N., *Organische Chemie*, Wiley-VCH, 1994.

[116] Wiberg, E., Holleman, A., and Wiberg, N., *Lehrbuch der anorganischen Chemie*, de Gruyter, 2007.

[117] Shustorovich, E. and Sellers, H., Surface science reports **31** (1998) 1.

[118] Boman, C., Acta Chem. Scand **24** (1970) 116.

[119] Atanasoska, L., O'Grady, W., Atanasoski, R., and Pollak, F., Surface science **202** (1988) 142.

[120] Kim, Y., Seitsonen, A., and Over, H., Surface science **465** (2000) 1.

[121] Sun, Q., Reuter, K., and Scheffler, M., Physical Review B (2004) 235402.

[122] Kiejna, A. et al., Physical Review B **73** (2006) 035404.

[123] Murnaghan, F., Proc. Nat. Acad. Sci. **30** (1944) 244.

[124] Glassford, K. and Chelikowsky, J., Physical Review B **47** (1993) 1732.

[125] Sun, Q., Reuter, K., and Scheffler, M., Physical Review B (2003) 205424.

[126] Kim, Y., Schwegmann, S., Seitsonen, A., and Over, H., The Journal of Physical Chemistry B **105** (2001) 2205.